

Enhancing charge carrier transport in solution-processed organic field-effect transistors by control of fluid dynamics

**Dissertation zur Erlangung des Grades “Doktor der Naturwissenschaften”
am Physik, Mathematik und Informatik der Johannes Gutenberg-
Universität Mainz und in Kooperation mit dem Max Planck Institute für
Polymerforschung in Mainz**



Okan Yildiz

Geboren in Istanbul, Türkei

Mainz im Februar 2024

Dekan: Univ. -Prof. Dr. Patrick Windpassinger

1. Gutachter: Prof. Dr. Paul W. M. Blom

2. Gutacher: Univ. - Prof. Dr. Mathias Kläui

Tag der mündlichen Prüfung 16/04/2024

Affidavit

Ich bestätige hiermit, dass ich die Dissertation selbstständig und ohne fremde Hilfe angefertigt habe. Außer den in der Arbeit genannten und referenzierten Stellen wurden keine externen Quellen verwendet.

Ich versichere ferner, dass diese Arbeit weder in gleicher noch in ähnlicher Form im Rahmen eines anderen Prüfungsverfahrens vorgelegt wird.

I hereby confirm that I completed the dissertation independently and without any external support. Except for the places mentioned and referenced in the thesis, no external sources were used.

I further confirm that this thesis is neither presented in the identical nor similar form as a part of another examination process.

Place, Date (Ort, Datum):

Mainz, 26/02/2024

Signature (Unterschrift):

A handwritten signature in black ink, consisting of a series of loops and a long horizontal stroke at the end.

Contents

Chapter 1 Introduction.....	2
1.2 Device physics of organic field-effect transistors.....	7
1.2.1 Device architectures.....	14
1.2.2 Operation principles of OFETs.....	17
1.2.3 Electrical characterization.....	19
1.3 Factors that effect OFET performance	22
1.3.1 Contact resistance and channel resistance.....	23
1.3.2 Molecular organization and order.....	27
1.3.3 Film morphology.....	30
1.3.4 Physics of meniscus – guided coating.....	49
1.4 Motivation	56
1.4.1 Optimal processing window by meniscus – guided coating.....	57
1.4.2 Tuning crystallization of OSC via controlled meniscus shape.....	58
1.4.3 Precise patterning of OSC during meniscus – guided coating.....	58
References.....	59
Chapter 2 Optimized charge transport in molecular semiconductors by control of fluid – dynamics and crystallization in meniscus – guided coating.....	71
2.1 Introduction.....	71
2.2 Results and discussion	73
2.2.1 C8 – BTBT morphology.....	73
2.2.2 Numerical analysis in coating bead and crystallization.....	77
2.2.3 Molecular organization.....	88
2.2.4 OFETs.....	92
2.3 Conclusion	96
References.....	98

Chapter 3 Role of meniscus shape on crystallization of molecular semiconductors and fluid dynamics during meniscus-guided coating.....	102
3.1 Introduction.....	102
3.2 Results and discussion.....	104
3.2.1 TIPS – pentacene morphology.....	104
3.2.2 Numerical analysis in coating bead.....	110
3.2.3 Molecular organization.....	116
3.2.4 OFETs.....	120
3.3 Conclusion	124
References.....	126
Chapter 4 Meniscus wettability – guided crystallization of molecular semiconductors.....	129
4.1 Introduction.....	129
4.2 Results and discussion	131
4.2.1 Patterning strategy.....	131
4.2.2 Morphology mapping.....	134
4.2.3 OFETs.....	137
4.3 Conclusion	141
References.....	142
Chapter 5 Conclusions.....	144
Chapter 6 Experimental appendix.....	146
Acknowledgements.....	150
List of publications.....	152
Curriculum vitae.....	153

Chapter 1 Introduction

The 20th and 21st centuries have seen remarkable technological advancements in the field of microelectronics. Today, microelectronics plays a crucial role in our modern daily life, affecting the information and communication technology[1], transportation[2], industrial processes[3], construction[4], health[5], energy[6], digital revolution[7] etc. In particular, the invention of the field-effect transistor (FET), as a main electronic component in the design of microelectronics, paved the way for all these developments.[8, 9] Many electronic applications have become possible owing to the switching and amplification features of transistors.[10, 11] For instance, transistors are used as power amplifiers in radio-frequency electronic applications to convert the low input signals into higher output signals with a defined gain. Especially, they are utilized in the antenna before transmitting the signal to improve the bandwidth, power efficiency, linearity and heat dissipation.[12] Power amplifier circuits are also used to convert audio (sound) signals, where the volume of the speakers can be adjusted by controlling the gain level.[13] On the other hand, transistors are also widely used as logic switches in integrated circuits. For example, central processing units (CPU) in modern computers use a binary system that receives, transmits and stores data by combining multiple “1” and “0”. A bit refers to the smallest unit of memory in a computer that is represented by either “1” or “0” with respect to the electrical status of a transistor. Here, “1” and “0” denote the switching characteristic of a transistor in terms of electrically on-(“1”) and off-(“0”) device. In a CPU, transistors as electronic switches are organized in logic gates where the logic gates operate based on binary inputs to produce binary outputs.[14, 15] The number of examples can be increased as transistors have been used in numerous electronic applications for over eighty years. The following is a discussion of the historical background and developmental stages of transistors.

In the 1940s, three scientists at Bell Laboratories, John Bardeen, Walter H. Brattain, and William Shockley, conducted a series of studies to create an amplifier to use in a telephone. In 1947, Bardeen and Brattain invented the point-contact transistor (PCT) where the transistor effect was observed for the first time and a device based on germanium as semiconductor was able to amplify a microphone input signal about eighteen times.[16] **Figure 1.1** presents the device configuration of the first invented transistor; where a PCT operates when a bias is applied to the collector and base and the emitter is kept grounded. Here, charge carriers are injected through the emitter consisting of a gold foil into the germanium semiconductor and are being collected at the collector. In this configuration, the biased metal base induces an electric field that polarizes the charges in the germanium and assists transferring a greater number of charge carriers to the collector.[17] A year later, Shockley invented the bipolar junction transistor (BJT) that led to the first appearance of transistors in production in the 1950s.[18] However, the BJT works differently from a PCT by dividing the semiconducting layer into three doped region, *pnp* or *npn*, where *p* and *n* refer to the hole and electron doped area, respectively. One of the most crucial parameters for evaluating a transistor is its gain, which represents the ratio between the current at the emitter and the current at the collector. This parameter strongly improved as the transistor technology evolved from PCT to BJT. These three scientists received jointly the Physics Nobel Prize in 1956 for the invention of the transistor and description of its working mechanism.[19]

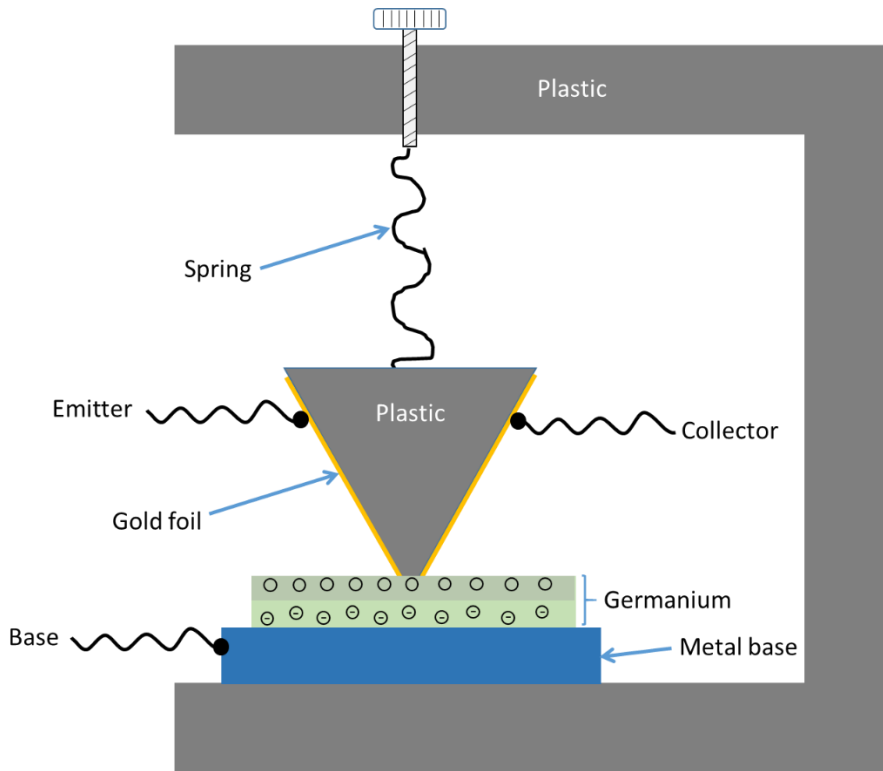


Figure 1.1 Sketch of a point-contact transistor. Gold foils are on the two sides of isolating plastic that assists the foils to contact the germanium semiconductor, which has a metal base at the bottom.

Another breaking point came when Mohamed Atalla and Dawon Kahng invented the metal-oxide semiconductor field-effect transistor (MOSFET) in 1959. Differently, the MOSFET solved the problem of charge diffusion into the gate terminal by using silicon dioxide as passivation layer on top of the silicon gate.[20] A short time after, Frank Wanlass and Chih-Tang Sah presented the concept of complementary metal-oxide semiconductor (CMOS) to be used for logic functions in 1963.[21] CMOS technology leads the way to construct integrated circuits such as microprocessors, memory chips, data converters, microcontrollers and other digital logic circuits.[22]

In the last decades, the mass production of electronic devices based on silicon technology has prompted an exploration of alternative FETs. This was mainly due to the potential shortage of silicon in the future and high material and manufacturing costs. An alternative was found in 1986, when Mitsubishi Electric researchers Koezuka, Tsumura and Ando reported the first organic field-effect transistor (OFET) based on a thiophene based conjugated polymer.[23, 24] The most important difference of OFETs from previous MOSFETs is the channel material, which is an organic semiconductor (OSC). There are several important differences between inorganic and organic semiconductors. First, the inorganic semiconductors used in MOSFETs are solid state structures from group III, IV and V elements of the periodic table and metal oxides / chalcogenides.[25] However, an OSC is a carbon based compound relying on the combination with different elements such as hydrogen, oxygen and nitrogen.[26] Secondly, adjacent atoms in the inorganic semiconductors share valence electrons that form a strong covalent bond.[27] In contrast, organic molecules in an OSC film are held together by a weak van der Waals interaction.[26] The type of bond between adjacent atoms or molecules is one of the most important parameters defining the charge transport mechanism, where this is band-type transport for inorganic semiconductors[28] and hopping transport for OSCs[29]. However, an exception rather than the rule is that a single crystal OSC may also be capable of exhibiting band-type transport.[30] At last, OSCs have several advantages over inorganic semiconductors because they are flexible, lightweight and have low-cost fabrication in terms of synthesis and deposition.[31, 32] A more detailed discussion regarding the differences between an inorganic semiconductor and OSC can be found in section 1.2.

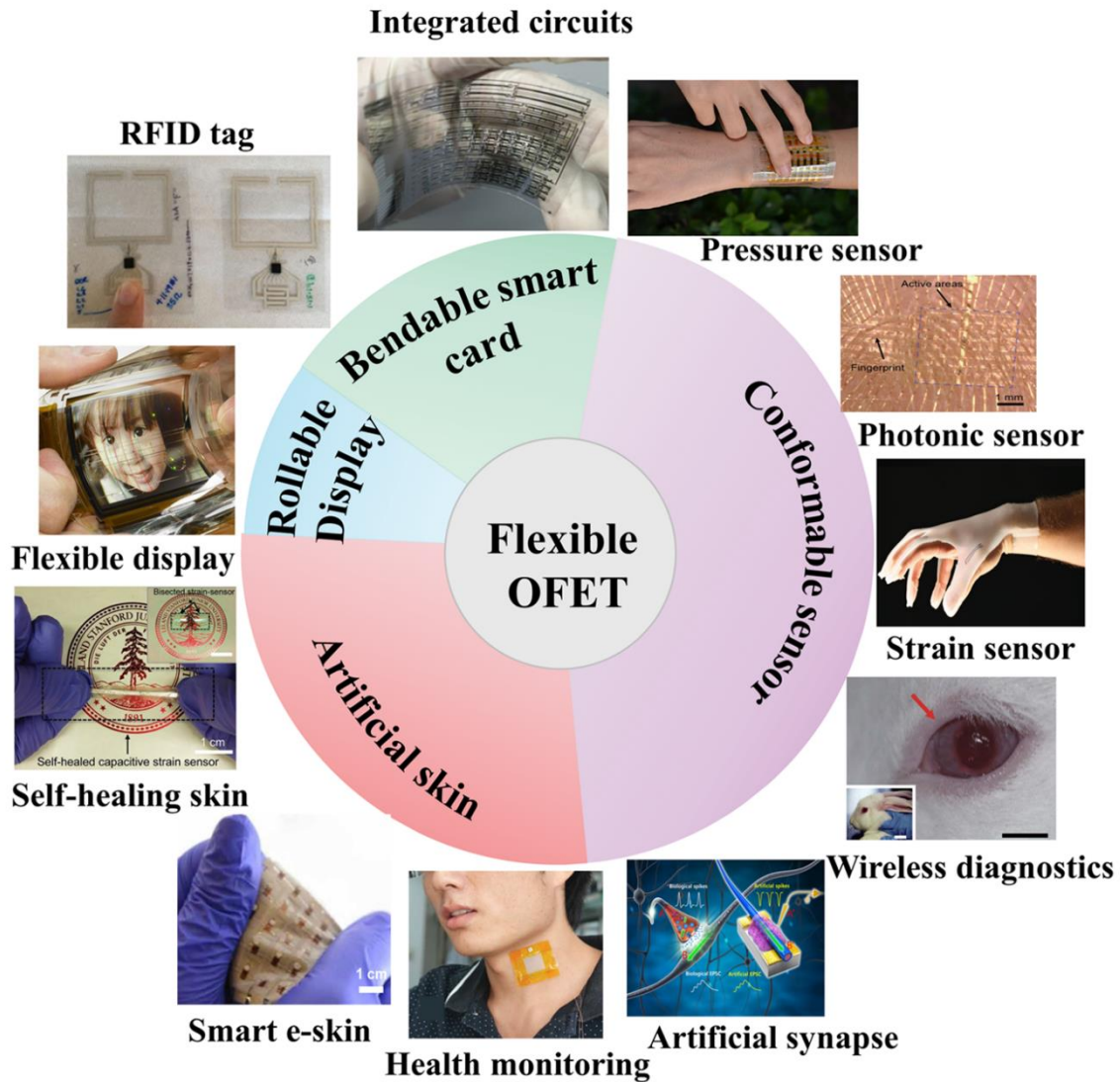


Figure 1.2 Example of various OFET applications such as rollable displays, bendable smart cards, conformable sensors and artificial skin.[33]

Since the second half of the 1980s, numerous research efforts have been dedicated to the study of OFETs by both the academia and industry. A noticeable progress has been observed in the implementation of next generation electronics, especially in flexible[33] and printed electronics[34]. Several key aspects have been investigated, including: i) improving electrical performance[35], ii) creating an environmentally stable device[36], iii) large area coverage[37],

and iv) longer device lifetime[38]. The primary focus of this thesis revolves around the first aspect, where the electrical performance is evaluated based on various device operation parameters. Among these parameters, charge carrier mobility is a main parameter, representing the drift velocity of the charge carriers under an applied electric field. Significant advancements have been made, with hole mobilities rising from $10^{-5} \text{ cm}^2 \text{ V}^{-1} \text{ s}^{-1}$ to $40 \text{ cm}^2 \text{ V}^{-1} \text{ s}^{-1}$ and electron mobilities reaching to $11 \text{ cm}^2 \text{ V}^{-1} \text{ s}^{-1}$. [39] Undoubtedly, this progress is a result of multiple successful approaches that are essentially driven by the design of novel OSC compounds, improvement in device deposition techniques, enhanced interface engineering and diverse approaches to reduce the impurities in OSC etc. As an outcome of intensive research activities, various electronic applications have become possible, such as rollable display, bendable smart card, conformable sensor and artificial skin, shown in **Figure 1.2**. [33, 35]

1.2 Device Physics of OFETs

OFETs differ from other types of FETs because of their active layer, which is an organic semiconductor. An OFET essentially is composed of three electrodes (source, drain and gate), a dielectric layer and an OSC active layer. [40, 41]

Source, drain and gate electrodes are the conductive metals playing a role in controlling the direction of the charges in the OSC. The source electrode serves as the terminal through which the charge carriers, either holes or electrons, are injected. Conversely, the drain electrode functions as the terminal where these carriers are ejected. Positioned between them, the gate electrode generates an additional electric field between itself and the source, increasing the number of injected charge carriers and fasten them towards the drain terminal. [42] The drain and source electrodes are typically selected with respect to several criteria that are environmental stability, compatibility of the work function with the energy diagram of the OSC,

and flat interface morphology between the electrodes and target substrate. Nevertheless, the gate electrode differently has to create a good interface morphology with the dielectric in order to maintain a homogeneous electric field.

Secondly, the dielectric layer is an insulating material used in conjunction with the gate electrode. The gate electrode under bias attracts the charge carriers from the source towards the dielectric layer because the biased gate generates an electric field within the dielectric material and active layer. In this process, the charge carriers move within a few monolayers of the OSC, following the path along the dielectric material, before eventually reaching the drain electrode.[43] The most commonly utilized combination in this context is heavily p-type doped silicon Si^{++} (gate) with silicon dioxide SiO_2 (dielectric).[44] Additionally, other dielectric layers such as inorganic insulators (e.g. Al_2O_3 [45] and Si_3N_4 [46]) and polymeric insulators (e.g. polymethylmethacrylate (PMMA)[47] and poly(4-vinylphenol) (PVP)[48]) are also employed in variable OFET applications. The selection of the dielectric layer is crucial because the relative permittivity- ϵ_r defines the dielectric capacity of the stored charges.[49, 50] The ϵ_r is the ratio between the complex frequency-dependent permeability of the substance ϵ and vacuum permeability ϵ_0 as shown in equation 1.[51]

$$\epsilon(\omega) = \epsilon_r(\omega)\epsilon_0 \quad (1)$$

In microelectronics, one strategy employed for circuit miniaturization is the utilization of a dielectric layer with a high relative permittivity $-\epsilon_r$. This is because the dielectric layer can store more charges per unit voltage, enhancing the electric field that it can generate with the same bias in a smaller area compared to a material with a lower relative permittivity $-\epsilon_r$. [50] This approach aligns with Moore's Law, which described an increase in the number of transistors per unit area over time[52]. The capacitance, denoted as C , is commonly used to

describe the electrical charge capacity of dielectric materials. It is a measure of the substance's permeability per unit area. The C is calculated as shown in eqn.2[53];

$$C = \frac{\varepsilon(\omega)A}{d} \quad (2)$$

where A is the capacitor area and d the thickness of the dielectric layer.

Thirdly, the semiconductor layer is crucial, as it is where the charge transport takes place during the operation of FETs. Commercialized inorganic FETs use the dopant ion implantation approach to control the charge carrier concentration within the semiconductor. For example, industrial MOSFETs based on silicon (Si) often use phosphorus (n-doping, electron donor) or boron (p-doping, electron acceptor) doping in their semiconductor components.[54, 55] A phosphorus atom has five electrons in its outer shell, while a silicon atom has 4 electrons. When a phosphorus atom is placed between four silicon atoms and activated by annealing at high temperature (e.g. 1000°C), its four electrons form covalent bonds with each silicon atom and the one electron remaining from the phosphorus acts as a free charge carrier.[56] This free charge carrier electron needs much less energy to occupy the conduction band as compared to an electron that needs to be excited from the valence band to the conduction band. On the other hand, boron, which has three outer electrons in its outer shell, is also widely used as dopant that forms bonds with silicon atoms. In this case, however, due to the missing electron the fourth silicon atom gains an extra hole that acts as a free charge carrier.[57] This arrangement contributes to the overall conductivity of the material, either phosphorus-doped silicon, where the majority of charge carriers are electrons, or boron-doped silicon, where the majority of charge carriers are holes.[58] In another example, gallium nitride (GaN) high-electron mobility transistors (HEMT) use the Si-ion implantation approach under the source and the drain electrodes to create an Ohmic (trap free) contact by minimizing the contact resistance. When a silicon atom is placed between three nitride atoms and share its three electrodes with each

nitride atom after annealing at high temperature (e.g. $\geq 1000^\circ\text{C}$), the fourth electron of Si becomes a free-charge carrier.[59] Consequently, the dopant ion implantation approach is utilized in inorganic transistors to modify the key electrical parameters such as carrier concentration, charge carrier mobility, threshold voltage, electrical on / off characteristics, contact resistance, and subthreshold slope (these parameters are explained in details in section 1.2.3 and experimental appendix). However, OFETs do not have the opportunity to employ this approach for two primary reasons: i) OSC molecules are weakly bound and cannot readily form covalent bonds with other molecules, and ii) many OSCs are sensitive and prone to damage when subjected to annealing temperatures exceeding 100°C . So far, various approaches have been developed to control the electrical parameters of OFETs. Particularly, achieving a trap-free OSC thin film stands out as a primary objective for researchers, accomplished either through the chemical design of OSCs or by controlling the morphology of existing OSC compounds. Here, I follow the second strategy and go into the details of the morphology control strategies for OSCs and its impact on the electrical parameters of OFETs in section 1.3.3.

OSC is divided into two categories based on their weight, which are high molecular weight (polymers) and low molecular weight (small molecules) materials. A polymer is formed from chains of monomers by linking monomers together by strong covalent bonds, through a process called polymerization[60] whereas small molecules are held together by a weak van der Waals interaction[61].

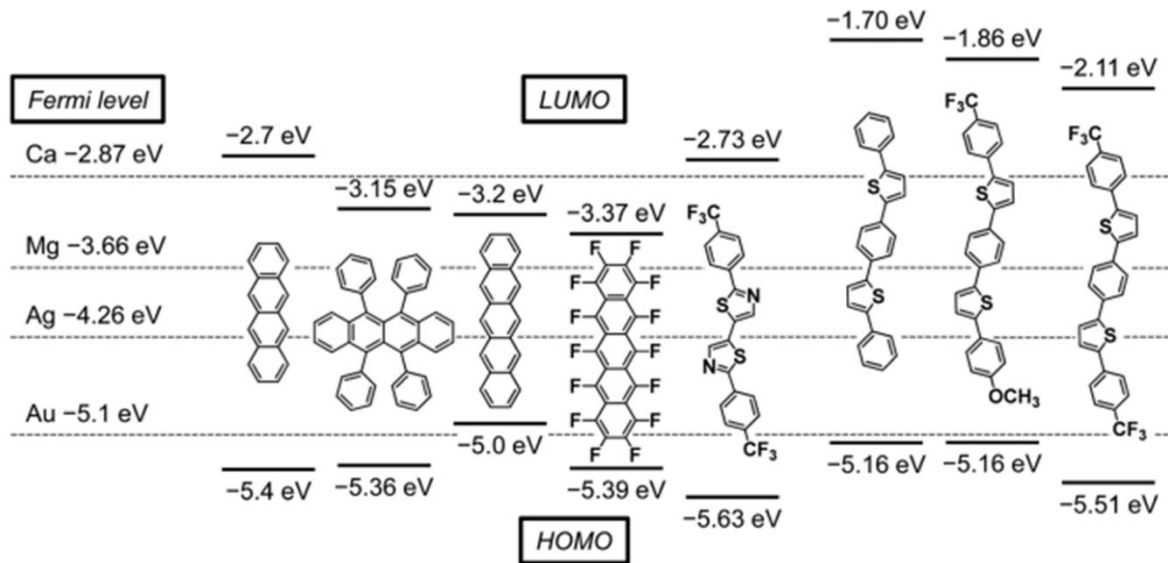


Figure 1.3 HOMO and LUMO level of various organic semiconductors with respect to the Fermi level of different metal electrodes.[62]

The energy band diagram of different OSCs shown in **Figure 1.3** illustrates that their electronic properties, including the HOMO / LUMO levels, can be tuned through molecular design.[26] The bandgap of OSCs typically ranges between 0.1 and 3.0 eV showing variation depending on the molecular structure.[63] The electrical characteristics of OFETs are highly connected with the occurrence of charge traps at the OSC / electrode interface and in the OSC channel. Particularly, the charge traps at the OSC / electrode interface can be prevented in the device design by finding a good match between the Fermi level of the metal electrode and HOMO (for p – type semiconductor) or LUMO (for n – type semiconductor) of OSCs, which significantly reduces the contact resistance in OFETs.[64] In **Figure 1.3**, the Fermi level of various metal electrodes is shown with respect to the HOMO and LUMO levels of different OSCs.[62, 65, 66] The energy difference between the Fermi level of the metal electrode and the HOMO (or LUMO) of the OSC is referred to as the Schottky barrier height.[67, 68] Reducing Schottky barrier height constitutes an essential strategy for diminishing the contact

resistance and prevents energy loss of charge carriers in the metal / OSC junction.[69] Achieving an Ohmic (trap-free) contact is highly desired to obtain high performance OFETs but it requires two conditions: i) minimizing the Schottky barrier and ii) creating a defect-free interface morphology between OSC and electrode.

An OSC can show either band-like transport or hopping transport. This depends on the crystallinity and the molecular order of the OSC. Single crystal OSCs mostly have shown to exhibit band-like transport (known as Boltzmann band) due to their high structural quality and chemical purity.[70, 71] The dynamic disorder in the molecular organization of an OSC film defines the type of charge transport. When the dynamics disorder is high and results in a low mobility, it is considered hopping transport. Conversely, when the dynamic disorder is low resulting in a high mobility, it is referred to as band-like transport. One way to determine the type of charge transport in an OSC is to check the relation between the charge carrier mobility and temperature. Band-like transport demonstrates an increase in mobility upon decreasing the temperature while it is opposite for hopping transport.[72] Because the band-like transport is limited due to phonon scattering (or lattice vibrations) and phonon scattering decreases with decreasing the temperature, resulting in the mobility increase.[73] However, hopping transport shows a thermally activated behavior.[74] In that case, mobile charges hop from one molecular orbital to another with a condition that a certain π - π stack distance must be maintained. The smaller the π - π stack distance is, the faster mobile charges can move.[75]

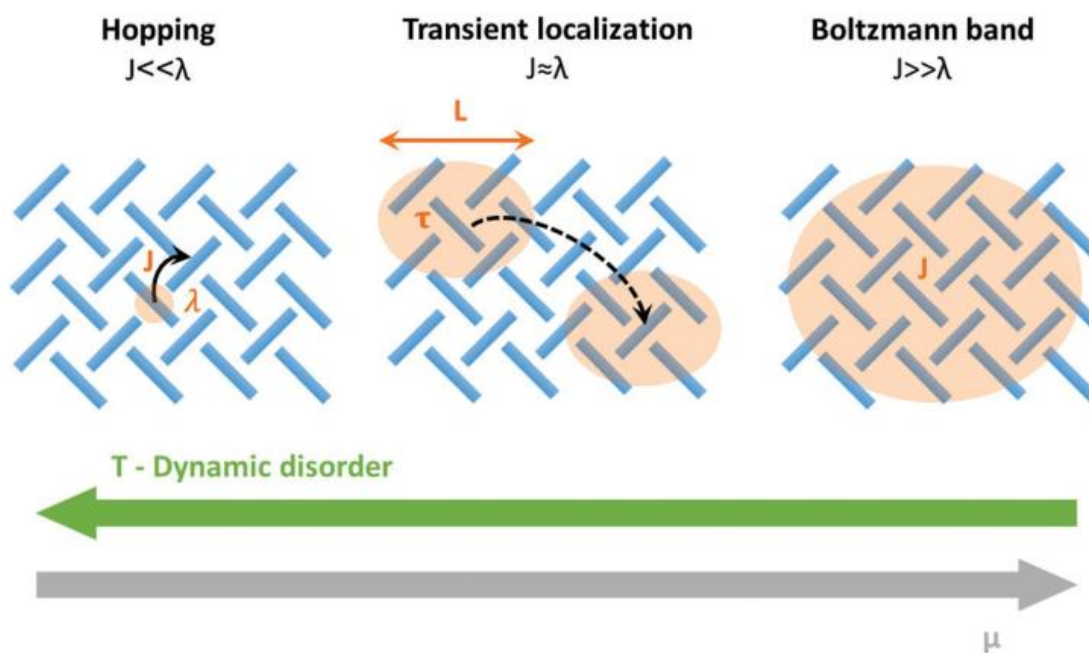


Figure 1.4 Sketch of charge transport mechanism showing three cases: hopping, transient localization and Boltzmann band (band-like) model. The orange areas disclose the charge delocalization. Each blue rectangle represents one molecule. [76]

An explicit description of the charge transport mechanism in solids exists for two extreme cases of very low ($\mu \ll 1 \text{ cm}^2 \text{ V}^{-1} \text{ s}^{-1}$) and very high charge carrier mobility ($\mu \gg 1 \text{ cm}^2 \text{ V}^{-1} \text{ s}^{-1}$) as shown in **Figure 1.4**. [76] These two extreme regimes can be described in terms of incoherent hopping of localized charges between sites [77] and Boltzmann band transport of delocalized Bloch electrons [78]. At the microscopic level, comparing the electronic coupling (or transfer integral) J with the reorganization energy λ provides an insight into the charge transport. J corresponds to the wave function overlap of the orbitals of neighboring molecules and λ refers to inner and outer reorganization energies. The inner and outer reorganization energies correspond to the sum of geometry relaxation energies in the molecule and medium nuclear polarization energy. They are typically seen in the range $10 \leq J \leq 100 \text{ meV}$ and $50 \leq \lambda$

≤ 500 meV.[29, 79, 80] As it is schematically presented in **Figure 1.4**, when $J \ll \lambda$ (weak coupling regime), the charge wave function localizes to a single molecule and a series of incoherent hopping events dominate the transport. Conversely, when $J \gg \lambda$ (strong coupling regime), the charge wave function delocalizes over several molecules and charges propagate by diffusion. In recent studies, the transient localization scenario for $J \approx \lambda$ shows that thermal lattice fluctuations result in temporal variations of the electronic coupling and site energies along the molecular lattice.[81, 82] As a result, the dynamic disorder limits the charge transport and reduces primarily the charge carrier mobility; therefore, control strategies of improving molecular order and orientation are inevitably crucial.

1.2.1 Device architectures

There are four typical OFET device configurations, as shown in **Figure 1.5**. In the bottom-gate and bottom-contact (BG / BC) device configuration, source and drain electrodes are first deposited on a dielectric layer, then a semiconductor is deposited on top of the dielectric and the source – drain electrodes.[83] OSC crystallization on a target substrate is influenced by several parameters such as surface roughness[84], surface tension[85], the presence of functional groups on the target surface[86] and substrate temperature[87].

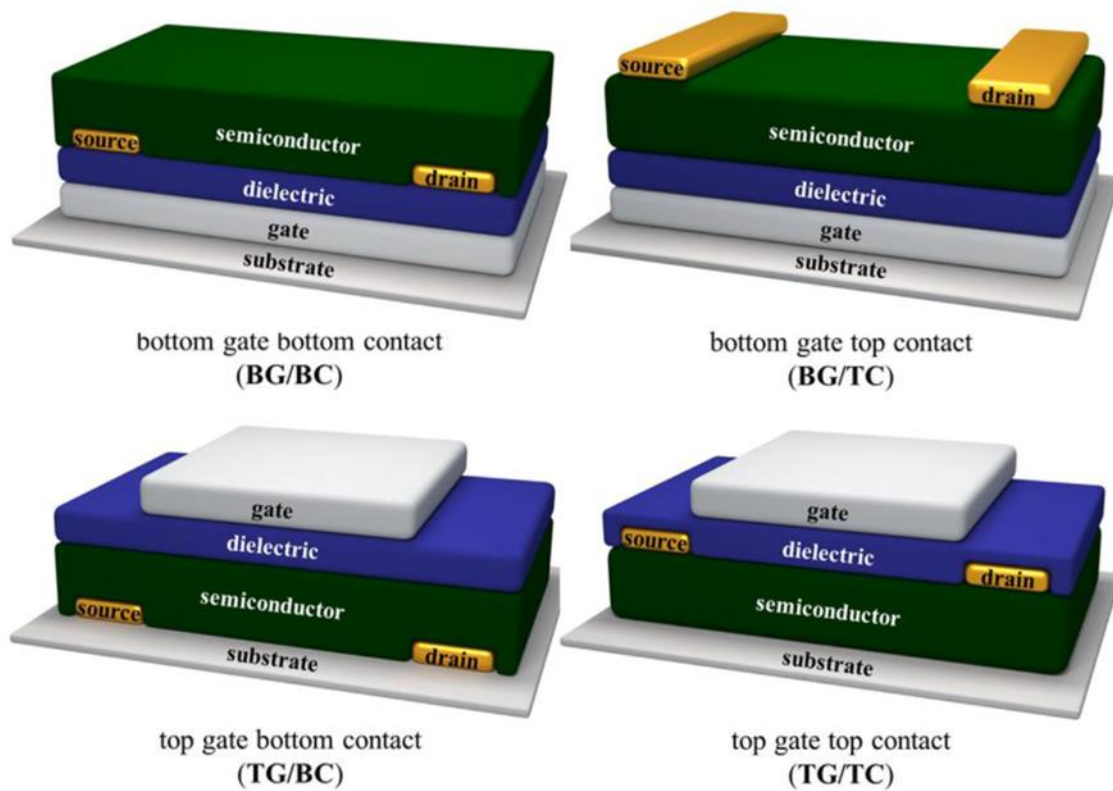


Figure 1.5 Four classical device architectures of OFETs; (a) bottom-gate bottom-contact (BG / BC), (b) bottom-gate top-contact (BG / TC), (c) top-gate bottom-contact (TG / BC) and (d) top-gate top-contact (TG / TC).[88]

The challenge in the BG / BC device configuration arises from the simultaneous crystallization of the OSC on both the metal electrode and the dielectric layer. This phenomenon can lead to discrepancies in molecular arrangement and the formation of crystal grains. These variations are attributed to the factors mentioned earlier, as well as the height difference between the dielectric and metal layers. For instance, spin – coating of fluorinated 5, 11-bis(triethylsilylethynyl) anthradithiophene (diF – TESADT) on a BG / BC (SiO_2 / Au) architecture leads to the growth of small grains on untreated Au electrodes while the larger grains are formed on SiO_2 . Particularly, the disparity in the OSC grain size between Au and SiO_2 primarily originates from the impact of the surface wettability. SiO_2 offers a higher

wettability platform for OSC crystallization, resulting in a larger grain size. Applying a pentafluorobenzene thiol (PFBT) treatment to the Au electrodes improves the surface wettability, thereby promoting the formation of larger diF-TESADT crystal grains and reducing the size difference of OSC crystals on the Au and SiO₂.^[89] Likewise, surface-dependent differences in OSC crystallization can also be observed on TG / BC configuration. Addressing this design concern, both BG / TC and TG / TC configurations hold an advantage, as OSC crystallization only takes place on a single target surface providing a homogeneous distribution. More detailed discussion on OSC crystallization can be found in section 1.3.3.

In the BG / BC and TG / TC configurations, a co-planar charge transport path is established from the source to the drain along the OSC channel. Particularly, the source electrode directly contacts both the dielectric and OSC layers, resulting in higher contact resistance due to the narrower transition zone between the source and OSC. As a result, the concentration of charge carriers at the source / OSC interface is higher than at the drain / OSC interface. However, in BG / TC and TG / BC configurations, a staggered charge transport path is formed, involving direct contact of the OSC only with the dielectric layer. This configuration leads to an equal distribution of the charge carrier concentration between the source and the drain within the OSC channel, consequently leading to a lower contact resistance.^[90] The contact resistance issue in OFETs is widely discussed in the section 1.3.1.

Finally, I selected the BG / TC device configuration for the experiments due to two advantages: the homogeneous formation of OSC crystal grains on a single target surface and an equal distribution of charge carrier concentration, generating a lower contact resistance at the source / OSC interface.

1.2.2 Operation principles of OFETs

To observe the transistor operation, a bias voltage is applied to the drain V_{ds} and gate V_{gs} electrodes, while the source electrode is grounded. The transport of charge carriers is driven by the combination of electric fields generated by the gate voltage V_{gs} and drain voltage V_{ds} . The V_{gs} bias at the gate electrode induces an electric field in the OSC and the dielectric layer that attracts the charge carriers from the source towards the dielectric within the OSC, meanwhile V_{ds} generates another electric field between the source and the drain electrodes that moves the charge carriers within the OSC towards the drain electrode where they are ejected. This trajectory of charge carriers, as shown in **Figure 1.6a**, occurs due to the higher electric field obtained by V_{ds} and the insulating property of the dielectric layer, the latter not allowing a significant current flow through the gate electrode. Depending on the type of the charge carriers, either electrons (n-type) or holes (p-type), the applied bias voltage should be positive or negative, respectively. For example, to operate a p-type transistor, a negative bias $V_{gs} < 0$ and $V_{ds} < 0$ must be applied to move the holes from the source to the drain (see **Figure 1.6a**). It is vice versa for n-type transistor, a positive bias $V_{gs} > 0$ and $V_{ds} > 0$ must be applied to move the electrons from the source to the drain. Lastly, ambipolar transistors can show both n-type and p-type operation functions.[42, 91] To measure an ambipolar OFET, a bias of $V_{gs} < 0$ and $V_{ds} < 0$ is applied to the electrodes for hole transport, followed by $V_{gs} > 0$ and $V_{ds} > 0$ for electron transport.

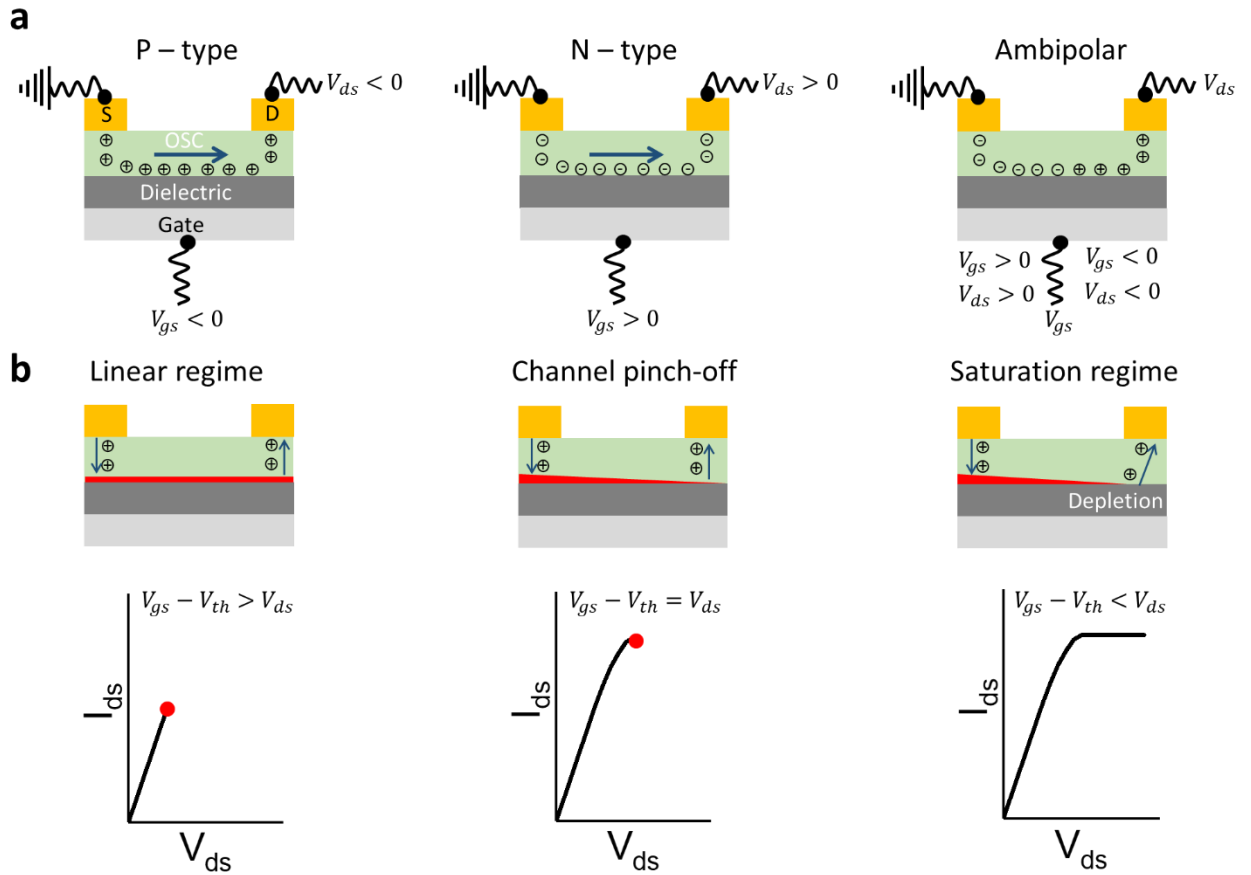


Figure 1.6 a) Charge transport in BG / TC device configuration is shown for p – type, n – type and ambipolar transistors. b) When sweeping V_{ds} , three regimes occur: linear regime, channel pinch-off and saturation regime. The red color within the OSC above the dielectric refers to the distribution of charge carriers.

The drain current I_{ds} highly depends on the density of charge carriers whereas charge traps reflected by a high resistance within the OSC, more specifically at the electrode / OSC interface and OSC / dielectric interface. The V_{th} is the required gate bias to fill all the charge traps in an OSC in order to switch the transistor electrically on.[92] The operation of a transistor is characterized by two regimes; a linear and saturation regime as shown in **Figure 1.6b**. When $V_{gs} - V_{th} > V_{ds}$, charge carriers are uniformly distributed between the source and the drain, this

region is called the linear regime. In this region, the drain current I_{ds} is proportional to V_{ds} . Upon increasing V_{ds} , a pitch-off point appears at a point where $V_{gs} - V_{th} = V_{ds}$. The pitch-off point is formed due to the narrower transition zone within the OSC from the dielectric to the drain when V_{ds} is high enough. In other words, as shown in **Figure 1.6b**, the channel depletes when the number of charge carriers attracted by the drain electrode is sufficiently high leading to the inhomogeneous distribution of the carrier density above the dielectric within OSC.[42] Then, I_{ds} reaches to the saturation and remains unchanged even V_{ds} increases further, this is called the saturation regime.[93]

1.2.3 Electrical characterization

Characterizing a transistor can be performed with two fundamental current-voltage curves, transfer and output, as shown for a p-type OFET in **Figure 1.7a-b**. Several important parameters can be extracted from these curves to evaluate the performance of a transistor such as charge carrier mobility, threshold voltage, on/off ratio, and subthreshold slope (swing).

An output curve, as depicted in **Figure 1.7a**, encompasses both the linear and the saturation regime. Building upon the previously provided information, **Figure 1.7a** presents I_{ds} for a sweeping V_{ds} under varying V_{gs} conditions. The V_{gs} bias induces the electric field which modulates the number of charge carriers transferred across the drain electrode and its impact is seen on the linear and the saturation regimes. Notably, I_{ds} at the saturation increases with V_{gs} .

The output characterization offers crucial insights into both the contact resistance and the evaluation of the OSC / electrode interface quality. Contact resistance is determined using the transfer length method (TLM) by fitting resistance data for varying channel lengths. This data is obtained from the linear regime of the output curve shown in **Figure 1.7a**. Moreover,

the examination of the contact between the metal electrode and OSC can be performed using the output curve. If I_{ds} linearly follows V_{ds} in compliance with Ohm's law, then the contact is considered Ohmic.[94, 95]

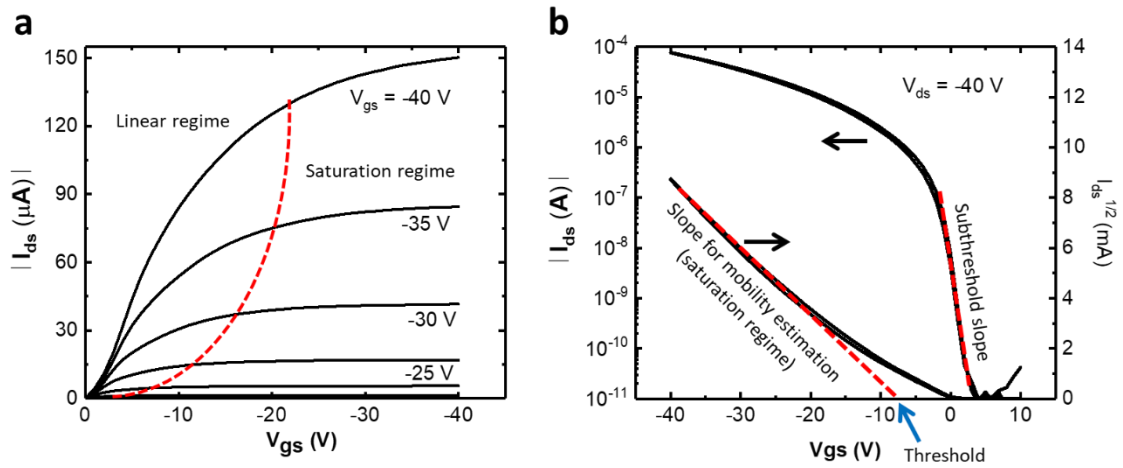


Figure 1.7 An example of (a) output and (b) transfer curves shown for a p-type OFET.

The second type of I-V characteristic, as shown in **Figure 1.7b**, is the transfer curve presenting I_{ds} for a sweeping V_{gs} under a constant V_{ds} . When I_{ds} is plotted on a logarithmic scale, the subthreshold slope (V_{gs}/I_{ds}) is calculated, indicating an order of magnitude increase in I_{ds} with respect to the applied V_{gs} . The subthreshold slope demonstrates the speed at which charge carriers move within the OSC in response to the electric field induced by the gate electrode. Therefore, it is widely used to evaluate the performance of the selected OSC or to numerically evaluate and compare the deposition conditions of the selected OSC. In addition, when $I_{ds}^{1/2}$ is plotted with respect to V_{gs} in **Figure 1.7b**, the mobility of the charge carriers in the transistor can be evaluated. Two types of mobility can be calculated, linear mobility in the linear regime and saturation mobility in the saturation regime. The mobility in the saturation

regime is a key factor showing how fast the mobile charges move in the presence of an applied electric field.[96] The threshold voltage is found by extending the fit of the slope for the mobility estimation to the x axis where $I_{ds}^{1/2} = 0$, the value of V_{gs} at this point gives the threshold voltage. The threshold voltage holds a distinct physical meaning: it represents the gate voltage required to establish a conductive channel between the source and the drain. This is hindered by charge traps, which prevent charge carriers from reaching the drain electrode. Consequently, some charge carriers are trapped before they can reach the drain electrode, and the threshold voltage is the point at which all these traps are filled.

The mathematical model behind the mobility extraction and its correlations with other parameters are crucial to understand the physical meaning of the charge carrier transport in FETs. For this reason, the gradual channel approximation is described in the following. An idealized condition for the one-dimensional approximation of the potential distribution provides a simple approach to show how the accumulated charges $Q_s(x)$ at the spatial position x is related to the potential profile V_{gs} along the channel;

$$Q_s = C_i V_{gs} \quad (3)$$

where C_i is the capacitance of the dielectric. As a result, I_{ds} can be calculated using the following eqn.;

$$I_{ds} = \frac{1}{L} \int_0^L E Q_s \mu dx \quad (4)$$

where L is the length of the channel, E the electric field and μ the mobility. By substituting eqn. 3 into eqn. 4, a widely used eqn. can be derived;

$$I_{ds} = C_i \mu_{lin} \frac{W}{L} (V_{gs} - V_{th} - \frac{1}{2} V_{ds}) V_{ds} \quad (5)$$

for $|V_{ds}| \ll |V_{gs} - V_{th}|$.

$$I_{ds} = C_i \mu_{sat} \frac{W}{2L} (V_{gs} - V_{ds})^2 \quad (6)$$

for $|V_{ds}| \geq |V_{gs} - V_{th}|$. In eqn.5 and 6, W is the width of the channel, μ_{lin} the linear mobility and μ_{sat} the saturation mobility.

Therefore, the linear and the saturation mobility can be written as;

$$\mu_{lin} = \frac{1}{WC_i V_{ds}} \frac{\partial I_{ds}}{\partial V_{gs}} \quad (7)$$

$$\mu_{sat} = \frac{2L}{WC_i} \left(\frac{\partial \sqrt{I_{ds}}}{\partial V_{gs}} \right)^2 \quad (8)$$

The detailed explanation of other parameters (threshold voltage, switch on / off ratio, subthreshold slope and switch on voltage) used in the performance evaluation of OFETs are in the Experimental Appendix.

1.3 Factors that affect OFET Performance

In this chapter, I explore the key factors that influence OFET performance. Previously established information has provided an essential insight into OFETs, covering device architecture, operational principles, charge transport mechanisms, and key current-voltage characteristics used to evaluate performance. Three significant factors play a critical role in performance: contact and channel resistance, molecular organization and order, and film morphology.

1.3.1 Contact resistance and channel resistance

The resistance at the interface of two materials during the flow of electrical current is called contact resistance. In OFETs, contact resistance occurs at the source electrode / OSC interface and at the drain electrode / OSC interface. Contact resistance can be caused by interfacial roughness, material impurities and Schottky barrier height. It has a critical effect on the device performance. Decades of research into OFETs has led to a good understanding of contact resistance and several solutions to reduce it.[95, 97, 98]

A simple circuit model is shown for BG / BC (**Figure 1.8a**) and BG / TC (**Figure 1.8c**) device configurations, and the corresponding resistance profiles are shown in **Figure 1.8b** and **1.8d**. The schematic sketch in **Figure 1.8a** and **1.8c** shows the injected current J_{int} and the device current J_{FET} as a result of the applied electric field \vec{E}_{\perp} between the source and the gate, and from the electric field \vec{E}_{\parallel} between the source and the drain. The resistance profiles in **Figure 1.8b** and **1.8d** include the contact resistance $R_{C,int}$ with the interface capacitance C_{int} at the electrode / OSC interface and the channel resistance R_{ch} in the OSC. In addition, the bulk resistance $R_{C,bulk}$ is formed for BG / TC due to the path followed by the charge carriers, which is perpendicular to the in-plane transport.[95] The final electrical behavior of OFETs can be influenced by the $R_{C,int}$, $R_{C,bulk}$ and R_{ch} , in such a way that capacitive effects introduce a time constant that affects the rate of charging and discharging, thus impacting the switching speed of the OFET. Moreover, they can alter the threshold voltage as well as the turn-on and turn-off characteristics of the OFETs. In conclusion, $R_{C,int}$, $R_{C,bulk}$ and R_{ch} should be minimized to ensure the operation stability and improved performance of the OFETs.

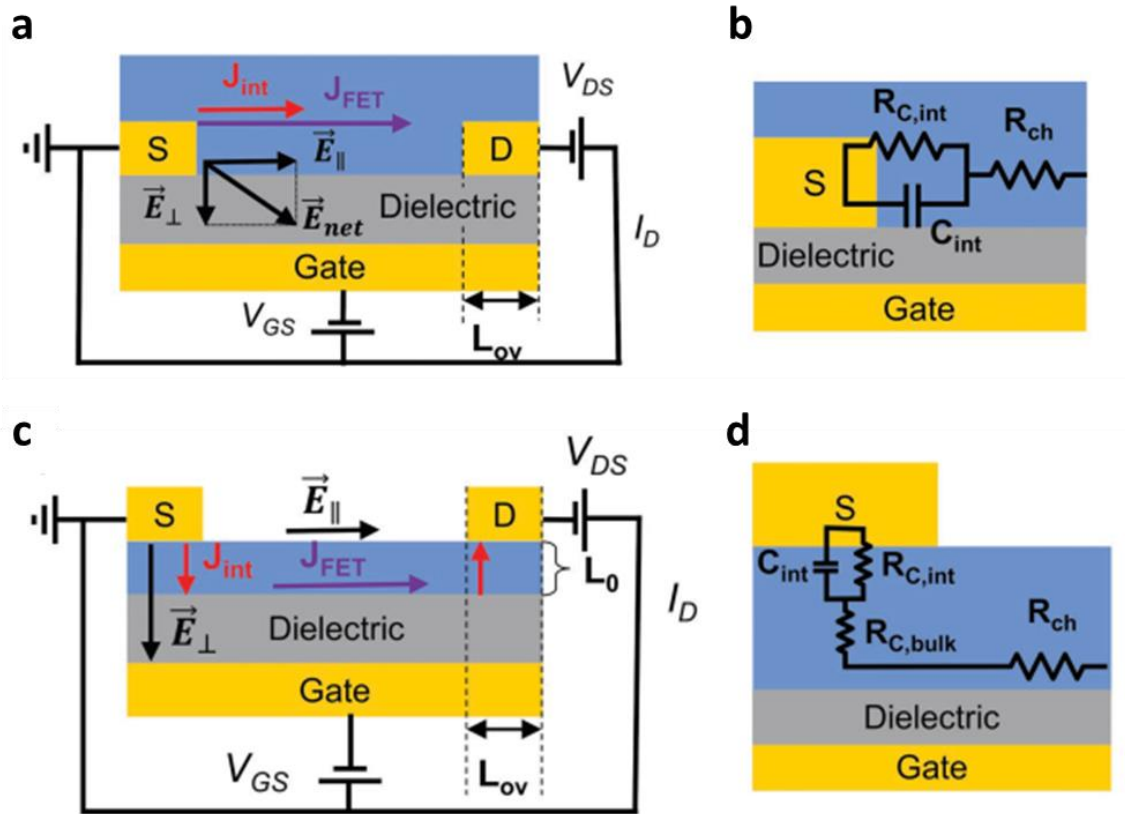


Figure 1.8 Electric fields \vec{E}_{\parallel} and \vec{E}_{\perp} generated by V_{DS} and V_{GS} are shown for (a) BG / BC and (c) BG / TC device configurations. Injected current J_{int} flows perpendicular to the device current J_{FET} at (a) and parallel to J_{FET} at (c). A simple circuit model for OFET in (b) and (d) displays the resistance profile where $R_{C,int}$ the contact resistance between the metal electrode and the semiconductor, and R_{ch} the channel resistance in the semiconductor above the dielectric. Lastly, $R_{C,bulk}$ the bulk resistance for BG / TC device is shown at (d).[95]

One of the strategies to reduce $R_{C,int}$ and $R_{C,bulk}$ is the control of the electrode / OSC and OSC / dielectric interfaces by using a self – assembled monolayer (SAM). A SAM can be used either at the electrode / OSC interface or at the OSC / dielectric interface. In the first case, SAM’s dipole moment can induce a redistribution of charges at the metal / SAM interface, thereby shifting the work function of the metal.[99] Secondly, it has the ability to block the

hydroxyl groups on the dielectric surface by forming a chemical bond between the head of the SAM and the hydroxyl group on the substrate. In this way, a SAM successfully prevents the hydroxyl group related charge trapping at the OSC / dielectric interface.[100] For instance, **Figure 1.9a** and **1.9b** show how a SAM is utilized depending on the device configuration and the deposited surface. A pentafluorobenzenethiol (PFBT) treatment is applied on Au for the BG / BC device configuration because PFBT can create dipoles due to the high density of fluorine atoms in its structure, which would increase the work *function* of the metal. The n-tetradecylphosphonic acid (HC₁₄-PA) is applied on aluminum oxide and reacts with the hydroxyl group to provide a platform that eliminates interfacial charge traps. **Figure 1.9c** displays the contact resistance of both device configurations, where BC achieves a lower value of 29 Ω cm due to the modified work function of PBFT, which reduces the charge injection barrier.[101]

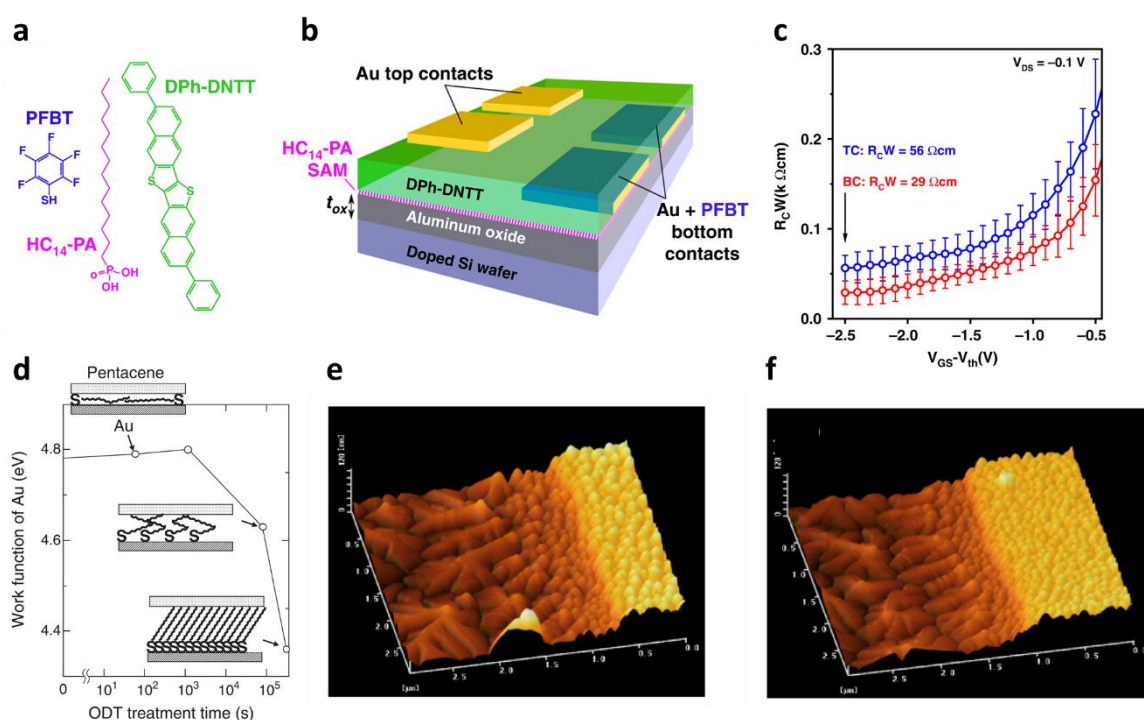


Figure 1.9 a) Chemical structure of pentafluorobenzenethiol (PFBT), n-tetradecylphosphonic acid (HC₁₄-PA) self-assembled monolayers (SAMs) and 2,9-diphenyl-dinaphtho-[2,3-b:2',3'-

f]thieno[3,2-b]thiophene (DPh-DNTT) OSC. b) Schematic illustration of OFET where aluminium oxide was treated by a HC₁₄-PA SAM in the BG / TC device configuration and the Au electrode was treated by a PFBT SAM in the BG / BC device configuration. c) Corresponding contact resistance R_C for both device configurations. d) Work function of the Au electrode as a function of octadecanethiol (ODT) SAM treatment time. The $3 \times 3 \mu\text{m}^2$ AFM images of pentacene films on SiO₂ and Au without ODT (e) and with ODT SAM (f). (a, b, c) are for ref. [101] and (d, e, f) are for ref. [102].

Furthermore, the device parameters such as the charge carrier mobility and the contact resistance are strongly influenced by the density of SAM molecules on the surface and its molecular alignment. For instance, the density of octadecanethiol (ODT) and its orientation on an Au surface changes with the deposition time as shown in **Figure 1.9d**. The work function of Au decreases from 4.8 to 4.4 eV as the deposition time of ODT SAM increases from ~1 min to ~170 min, where it is the main factor controlling the contact resistance. **Figure 1.9e** and **1.9f** contain AFM images of pentacene OSC on SiO₂ / Au without and with an ODT SAM (~1 min treatment time). These images clearly indicate the difference, a monolayer of ODT leads to a larger crystal grain, thereby decreasing the contact resistance from $\sim 1.4 \times 10^5$ to $\sim 0.9 \times 10^5 \Omega$. The lower contact resistance is a result of the improved crystallization of pentacene on the ODT SAM, which could be attributed to a better wettability. Finally, the saturation mobility rises from 0.05 to 0.08 cm² V⁻¹ s⁻¹ owing to the lower contact resistance and the modified work function of Au.[102]

1.3.2 Molecular organization and order

The molecular organization of an OSC can take one of the following three forms: amorphous, semi-crystalline, or crystalline. In particular, for the crystalline structures of low molecular weight OSCs, there are four common types of molecular packing motifs, which are herringbone, slipped π -stacking, slipped-stack and brick-wall arrangements, as shown in **Figure 1.10**.^[76, 103] The x and y coordinates in **Figure 1.10a** reveal the most likely plane of the charge transport with respect to the molecular arrangement, in some cases the charges can also move in the z direction as well.^[104]

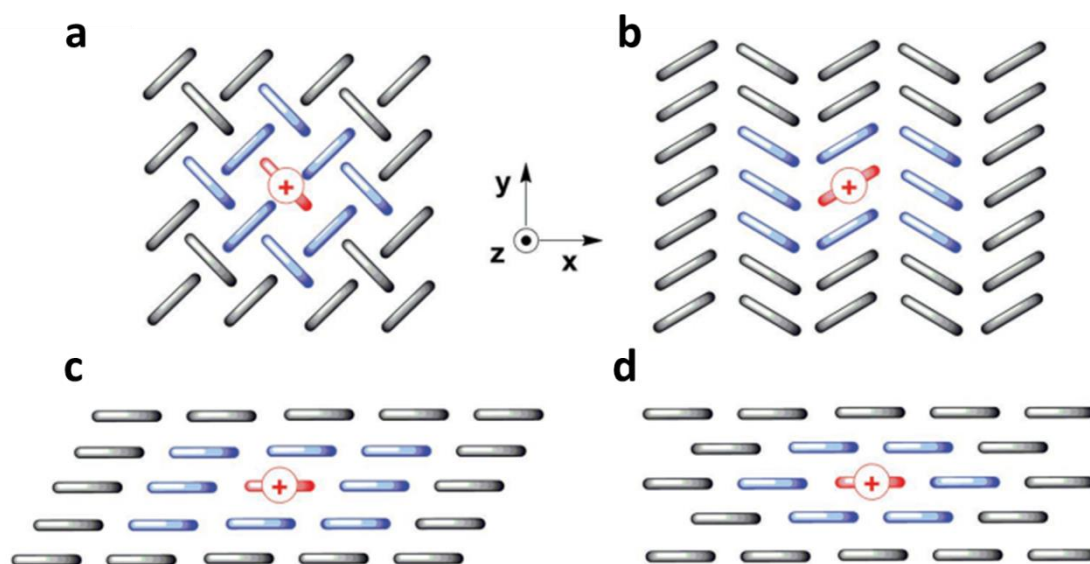


Figure 1.10 Most common packing motifs of organic semiconductors in a crystal are shown. A hole on a molecule is highlighted in red and the first neighbor molecules are colored in blue. a) Herringbone arrangement with charge transport dominated by edge-to-face interactions (eight first neighbors). b) Slipped π -stacking (eight first neighbors). c) Slipped-stack packing (eight first neighbors). d) Brick-wall arrangement (six first neighbors). The x-y plane is the plane of the charge transport.^[76]

In π -conjugated systems, weak van der Waals interactions are preserved between the adjacent molecules. Especially, the energies of the frontier molecular orbitals and the orbital distribution of a π -conjugated molecule have significant roles in intramolecular and intermolecular charge transport.[26, 29]

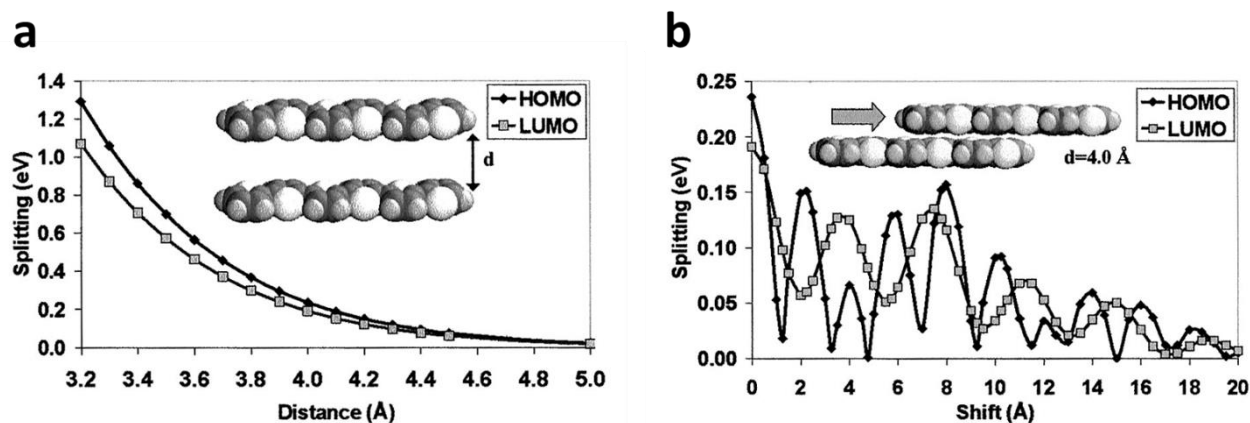


Figure 1.11 Electronic splitting of HOMO and LUMO levels in a dimer consisting of two sexithienyl molecules as a function of (a) variable distances d , and (b) degree of translation of one molecule along its main chain axis at $d = 4.0$ Å.[105]

The molecular geometry and packing of OSCs are crucial in defining their HOMO and LUMO levels. In **Figure 1.11a**, the electronic splitting (HOMO and LUMO) of a cofacial dimer made up of two sexithienyl molecules is plotted with respect to the distance d between the two adjacent molecules. As observed, the splitting energy for both the HOMO and LUMO is higher at a smaller d and decreases as d increases. This phenomenon is attributed to the weakening of electronic interactions between two adjacent molecules as d increases. Moreover, **Figure 1.11b** presents the variation in the splitting of the HOMO and LUMO levels in relation to the degree of translation of a molecule along its main chain axis at a constant $d = 4.0$ Å. Interestingly, the

energy splitting results in an oscillating behavior in the HOMO and LUMO; however, the oscillations in the HOMO and LUMO are different from each other and do not follow an overlapping trend. This trend indicates that, depending on the shift value, the splitting of the LUMO level can be higher than the HOMO, implying that the electrons could be more mobile than the holes.[105] As a result, the HOMO and LUMO levels, which play a crucial role in the charge transport properties of an OSC, can be tuned by controlling the molecular geometry and packing of an OSC.

Nonetheless, it is crucial to consider the chemical structure of OSCs, as it significantly influences the molecular motifs and their arrangement.[106] For instance, **Figure 1.12** illustrates rubrene derivatives, where R represents the functionalized component of the chemical structure. Additionally, **Figure 1.12** demonstrates the effect of different functional groups on molecular motifs and charge carrier transport. These findings are based on functional density theory and molecular dynamics simulations. Functionalized groups such as -CN, -CF₃, fluorination, and thiophene lead to distinct outcomes: poor packing motifs without π -stacking, 1D π -stacking with low mobility, 2D brick packing with low mobility, and herringbone-like π -stacking with high mobility.[107] Therefore, it is essential to understand that functionalized groups in the chemical structure of OSCs not only adjust molecular motifs, but also influence the π -stacking, thereby affecting charge carrier mobility.[26]

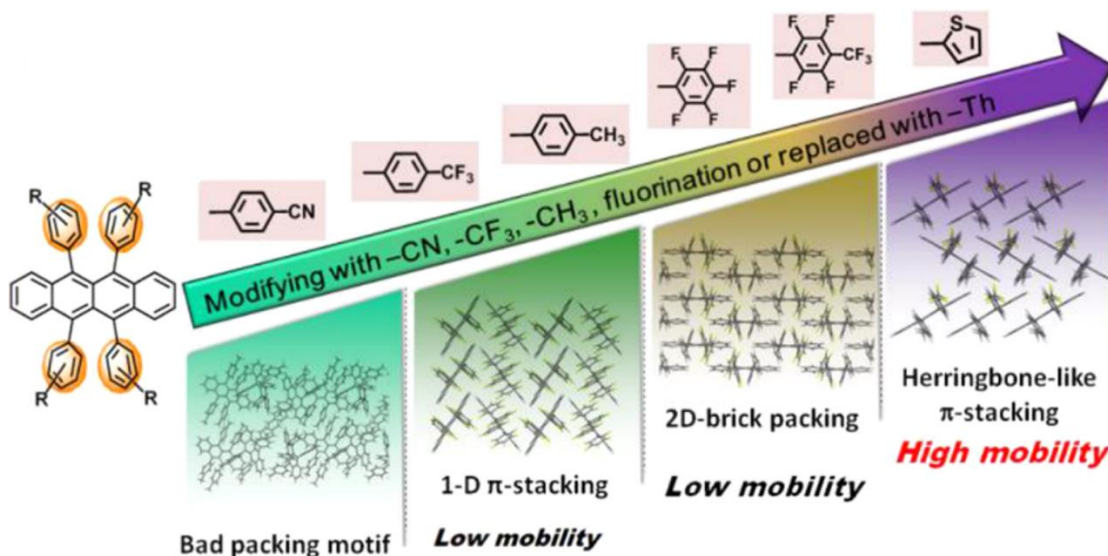


Figure 1.12 Modified rubrene derivatives that are functionalized with electron-withdrawing groups (-CN, -CF₃, -CH₃, or fluorination) on the peripheral phenyls influence the molecular packing and the mobility.[107]

In conclusion, achieving efficient charge transport in an OSC requires the optimization of the chemical structure, which defines the molecular motifs, geometry, packing, and electronic splitting between adjacent molecules. Next, I discuss the relation of film morphology with molecular organization and charge transport, and the methods of controlling it.

1.3.3 Film morphology

Charge transport in OSCs relies on the details of molecular arrangement, mesoscale microstructure, and morphology. Although it is difficult to have a precise control on the morphology and obtain a defect-free structure due to the weak van der Waals interaction between neighboring molecules, one may tune the local intermolecular charge transfer by molecular design and chemistry.[108-110] These changes in molecular design and chemistry

affect not only the molecular packing, but also the formation of the device scale morphology (microstructure and mesoscale long range organization in the device channel), therefore have a decisive influence on the electronic properties.[106]

An outline of different physical features depending on the scale is shown in **Figure 1.13a**. Here, the sketches in the squares with a scale ruler present length-specific physical information for the low molecular weight semiconductor (TIPS-pentacene). Beginning from the angstrom level, molecular scale packing and π -stacking are seen, followed by the appearance of local defects, lattice order and grain boundaries around the 1-10 nm scale. In addition, grain and domain boundaries become visible as well as their size, orientation, and distribution from 10 to 100 nm. Finally, the device scale arrangement with grain boundaries and domain size appear from 100 nm to several μm length.[108] The film morphology in the device scale arrangement shown for an OFET with a TIPS-pentacene active layer in **Figure 1.13a** influences the electronic properties. In general, the defects and grain boundaries are obstacles to charge carriers and act as charge traps, which would rise the contact resistance and the channel resistance as discussed in the section 1.3.1. Particularly, the transfer and output curves (discussed in detail in section 1.2.3) and the relative parameters used to evaluate the performance of an OFET are strongly influenced by the defects and grain boundaries. Charge carrier mobility and grain boundary density have an indirect relation, minimizing grain boundary density enhances charge carrier mobility.[111]

Furthermore, **Figure 1.13 b-d** displays an example of how molecular orientation can be examined using grazing incidence wide-angle X-ray scattering (GIWAXS).[108] The molecules are randomly oriented in thin films, as shown in **Figure 1.13b**, which results in a random scattering of incoming light with variable angles (χ) in three dimensions, hence the relative GIWAXS pattern shows a ring-like shape formation. **Figure 1.13c** exhibits partially

oriented molecules that allows the separation of out of plane (q_z) and in-plane (q_{xy}) peaks. At last, **Figure 1.13d** presents an example of a highly oriented molecular arrangement and its GIWAXS pattern reveals the uniformity of scattered light with respect to the molecular orientation, providing clear evidence of high crystallinity.[108, 110, 112, 113]

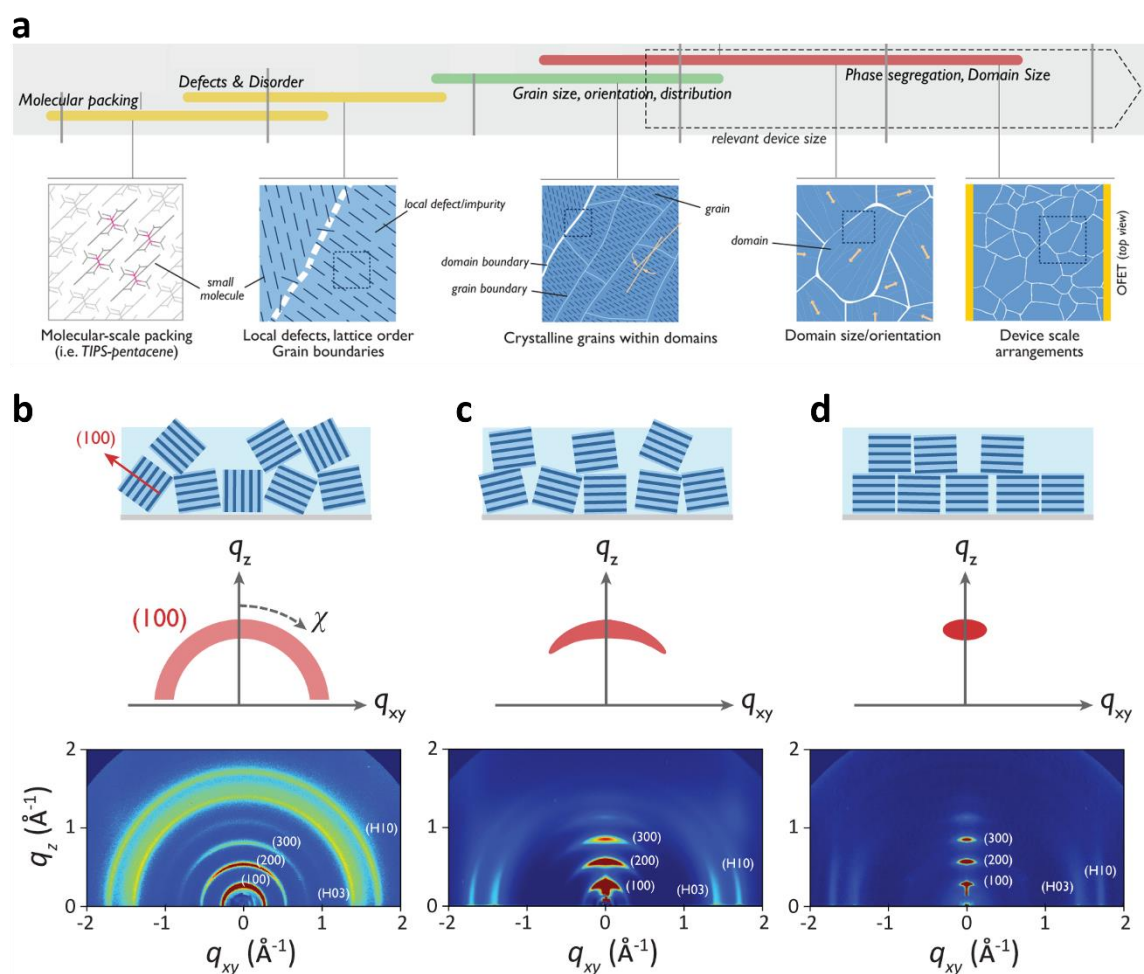


Figure 1.13 a) Morphological features for variable scales are shown from 1.0 Å to 10.0 μm. Each square corresponds to a range of scales and physical features. The series show single – component small molecule semiconductor (TIPS-pentacene) used in organic thin-film transistors (OTFTs). Domains refer to similarly oriented grains. b) Randomly oriented crystallites with no preferred growth direction. c) Oriented crystallites with a distribution of

crystallite orientations. d) Highly oriented film. (b, c, d) GIWAXS patterns of the corresponding films are at the bottom, described in the text.[108]

Not only the chemical structure of OSCs has a crucial effect on the charge transport, but also the deposition method of OSCs has dramatic effects on the physical features of the final OSC morphology. In terms of morphology, defects, the alignment of crystalline grains, grain size, homogeneity and density of grain boundaries need to be controlled, as these morphological features play a significant role in the transport of charge carriers in an OSC film.[73, 114-116] Therefore, researchers have developed numerous solutions to overcome the above-mentioned morphological problems for more than three decades. In the following paragraphs, I will elaborate different approaches to control the film morphology of OSCs.

A widely used strategy to control the morphology, crystallinity, and molecular orientation of OSCs is based on the deposition technique. There are various solution processing techniques used to deposit an OSC, as shown in **Figure 1.14**. [114] They are based on the OSC solution consisting of a solute and a solvent, in which the evaporating solvent simultaneously allows the solute to crystallize. Drop-casting and spin-coating are the two most commonly used techniques. Subsequently, printing and meniscus-guided coating techniques are two different classes of deposition techniques that represent more versatile and controllable film deposition of the solution process.

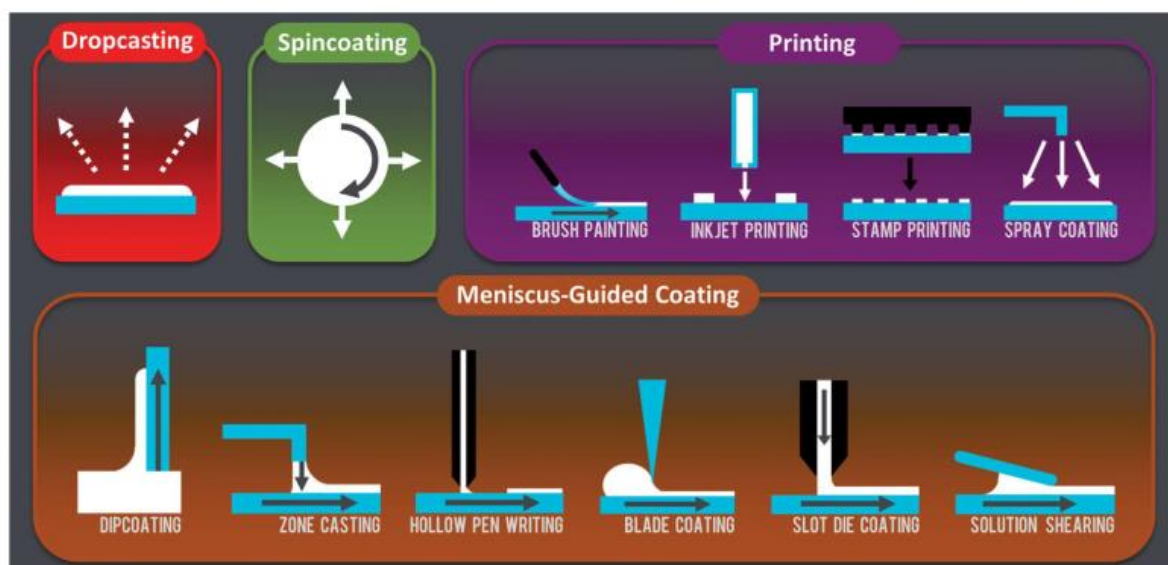


Figure 1.14 Schematic sketch of variable solution based processing techniques.[114]

Drop-casting is a simple and rapid method of dropping OSC solution onto the target substrate using a pipette or syringe. The solvent then substantially evaporates at the liquid / substrate / air interface and the liquid is withdrawn in the drying direction. Several morphology control strategies have been offered for drop-casting OSC materials. The main controllable parameters in drop-casting include the choice of solvent, fluid flow[117], solvent evaporation and processing temperature. Particularly, the choice of solvent and the control of fluid flow are commonly employed strategies in drop-casting. An illustration of the effect of solvent choice is given in **Figure 1.15**, where **Figure 1.15a** shows four optical images (OM) of drop-cast TIPS-pentacene. Each image corresponds to a different solvent used in the solution: (i) toluene, (ii) chlorobenzene, (iii) tetrahydrofuran, and (iv) chloroform. The films deposited with (i) toluene and (ii) chlorobenzene exhibited large crystal grains, measuring several hundred micrometers. Conversely, (iii) tetrahydrofuran and (iv) chloroform exhibited a microcrystalline structure with a high density of grain boundaries. This difference can be attributed to the boiling temperature of the solvent. Tetrahydrofuran and chloroform, which have lower boiling points (61°C and 66°C, respectively), allowed faster crystallization and limited structural

rearrangement compared to toluene and chlorobenzene (110°C and 131°C). In addition, the difference in the crystallinity of these films was analyzed using XRD measurements, as shown in **Figure 1.15b**. The film deposited from toluene exhibited the most intense peaks referring to higher crystallinity, as evidenced by numerous Bragg peaks assigned to the (00*l*) reflections of TIPS-pentacene.[118] Consequently, the choice of solvent and the process temperature significantly influence the film morphology during the drop-casting of OSC solutions.

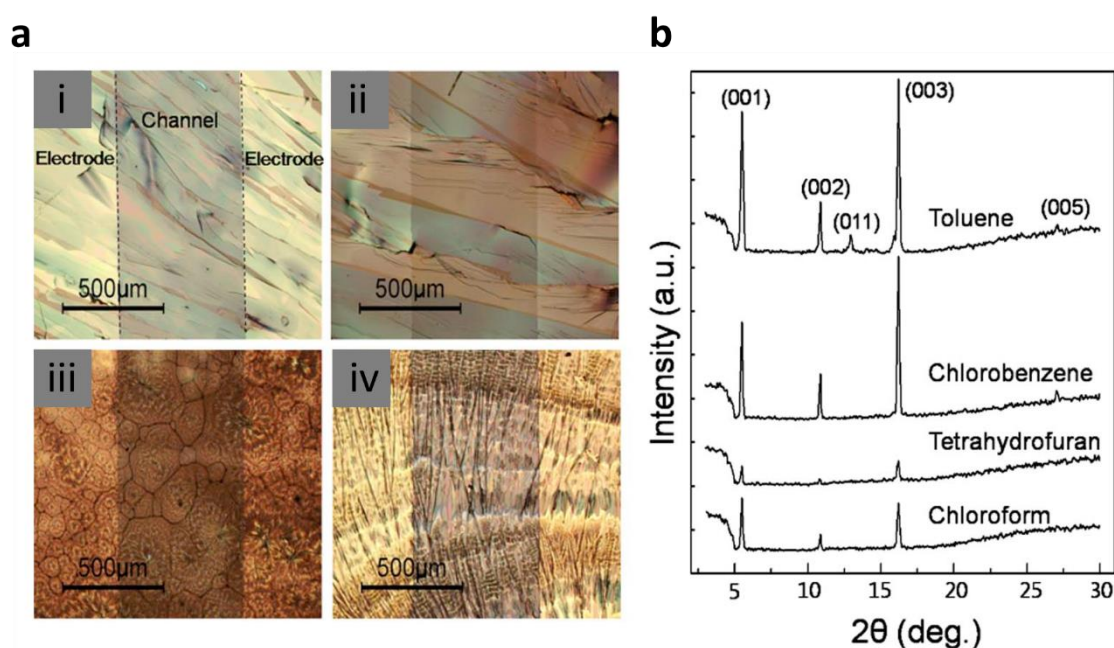


Figure 1.15 a) Optical images of drop-cast TIPS-pentacene deposited in the channel region of OFET using the following solvents: (i) toluene, (ii) chlorobenzene, (iii) tetrahydrofuran and (iv) chloroform. b) XRD patterns of TIPS-pentacene deposited using various solvents. (a, b) are from ref.[118],

Another example of the strategy of controlling the direction of fluid flow during drop-casting is presented in **Figure 1.16**. In this case, a BPEA:mesitylene solution was deposited on

a pre-heated substrate, and a coverslip was placed under the corner of the substrate to create a slight slope (as shown in **Figure 1.16a**) to direct the crystallization. This tiny slope influenced the receding path of the solution as well as the formation direction of the BPEA crystal arrays. **Figure 1.16b** shows OM images of well-aligned BPEA single crystals on (i) SiO₂ and (ii) glass, but the uniformity of the crystals is better on (i) the SiO₂ surface while the crystals are wider on (ii) the glass surface.[117] Consequently, not only the fluid flow control but also the surface that the crystallization occurs on has an impact on the morphology of crystals. Although the receding direction defines the growth orientation of BPEA crystals (**Figure 1.16a**), the issue of misalignment of crystal orientation persists.

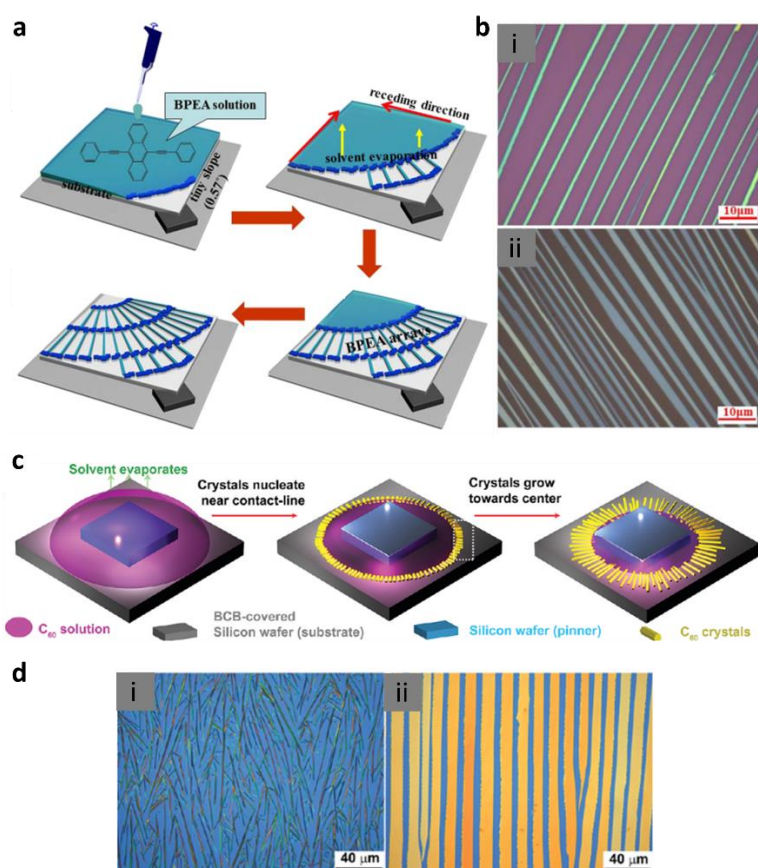


Figure 1.16 a) A schematic sketch of drop-casting 9,10-bis (phenylethynyl) anthracene (BPEA) OSC solution. A coverslip under the corner of the substrate was located to provide a height to

induce the nucleation. b) BPEA arrays (i) on SiO₂ and (ii) on glass. c) Droplet-pinned crystallization (DPC) method used to deposit C₆₀ solution on the divinyltetramethyldisiloxane bis(benzocyclobutene) (BCB) SAM coated silicon wafer. d) OM images of C₆₀ deposited by DPC using only (i) m-xylene and (ii) CCl₄:m-xylene dual solvent. (a, b) are from ref.[117] and (c, d) are from ref.[119].

Another fluid flow control strategy is illustrated in **Figure 1.16c**. The C₆₀ solution was dripped onto the BCB-coated silicon wafer and another smaller silicon wafer was placed on the top of the target substrate as a pinner. Due to the pinning of the droplet, the growth direction of the C₆₀ crystals is towards the center of the droplet. **Figure 1.16d** shows OM images with (i) needle and (ii) ribbon type morphologies deposited from the solvent (i) m-xylene and the binary solvent (ii) CCl₄:m-xylene.[119] As a result, the binary solvent resulted in a better alignment of crystals and higher crystalline structure due to the faster nucleation of the molecules with faster evaporation of the solvent, proving the importance of solvent selection on the final morphology. It should be underlined that the drop-casting method, even with the enhanced strategies discussed in **Figure 1.16**, has limitations owing to the challenge of aligning the crystals parallel to each other. Achieving such alignment is not likely possible with the drop-casting technique. This limitation has implications for the charge transport in OFET applications, where the crystals should ideally be perpendicular from source to drain electrodes and parallel to each other.

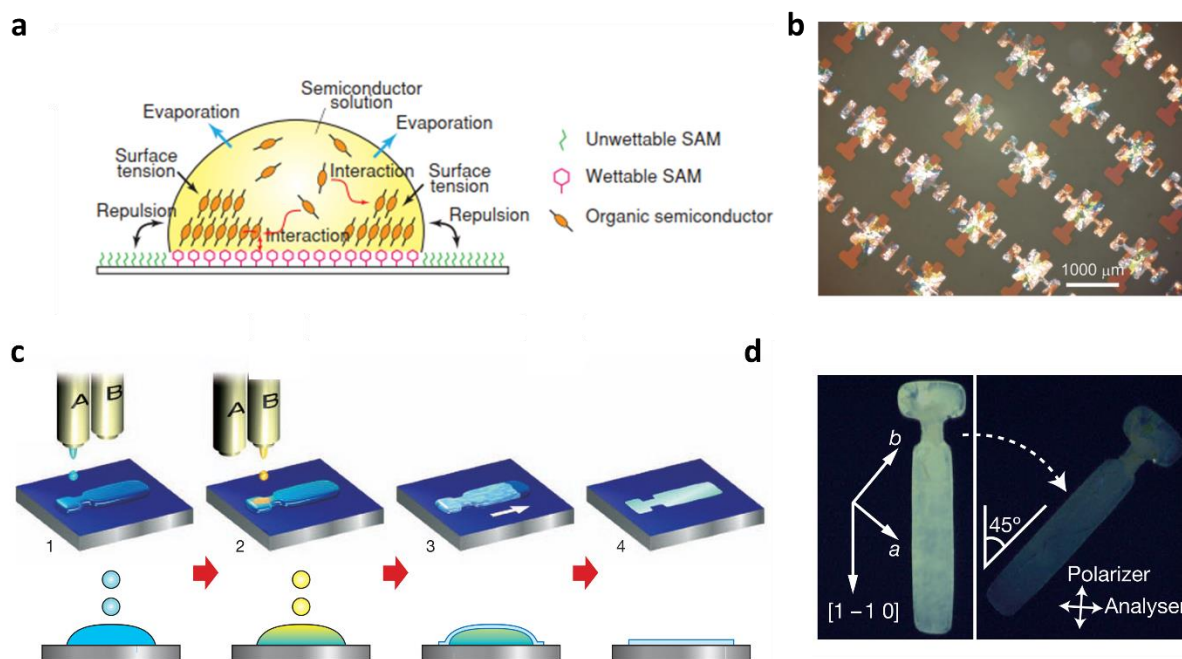


Figure 1.17 a) A sketch of the surface selective deposition (SSD) shows that an OSC solution is dropped on the modified substrate. The substrate is patterned by two different SAMs, one hydrophobic (unwettable) and the other hydrophilic (wetable). b) POM image of OFET arrays after drop-cast 2,7-dioctyl[1]benzothieno[3,2-b][1]benzothiophen (C8-BTBT) deposition on the modified substrate. c) Process sketch for the inkjet printing of OSC crystals is illustrated. “A” and “B” represent *N,N*-dimethylformamide (DMF) as antisolvent and 1,2-dichlorobenzene (DCB) as solvent used with C8-BTBT OSC. In step 1, DMF is initially deposited on the SiO₂ / Si substrate, followed by the deposition of the OSC solution (C8-BTBT:DCB) in step 2. Steps 3 and 4 illustrate the crystallization process, indicating the drying direction and the resulting C8-BTBT single crystal. d) Cross polarized OM image of C8-BTBT single crystal. (a, b) are from ref.[120] and (c, d) are from ref.[121].

Moreover, OSC crystallization by drop-casting can be selectively regulated using solution wettable (hydrophilic) and unwettable (hydrophobic) SAMs. A SAM treatment allows

modulating the hydrophilicity and hydrophobicity of a substrate, therefore, the contact angle of an OSC solution at the liquid / substrate interface. **Figure 1.17a** shows an exemplary operation where the OSC solution was deposited on a surface modified with partially wettable and unwettable SAMs. Then, the OSC crystallization only takes place on the wettable SAM modified surface while the unwettable SAM repels the solution to the wettable area. **Figure 1.17b** reveals an optical microscope (OM) image of C8-BTBT crystals on the active channel of OFETs after applying this strategy.[120] Last but not least, another strategy involves a novel inkjet printing process for the deposition of single crystal OSCs, shown in **Figure 1.17 c-d**. In this method, firstly, a SiO₂ / Si substrate was patterned into wettable (HMDS SAM) and unwettable (ultraviolet / ozone treatment) areas. Secondly, a two-step solution process was employed, where the antisolvent DMF was deposited on the wettable area, followed by the deposition of the OSC solution (C8-BTBT:DCB) on top of DMF, shown in **Figure 1.17c**. At 20°C, DCB exhibits a solubility that is 400 times higher than that of DMF. Upon depositing the C8-BTBT:DCB solution on top of DMF, an intermixed liquid is formed. This intermixed liquid induces the supersaturation of the solute before the liquid starts to evaporate. The process initiates the formation of crystalline nuclei within the liquid, and these nuclei serve as local seeds for the growth of a single crystal of C8-BTBT. As the intermixed liquid evaporates from the beginning of the droplet to the end, it leaves behind a single crystal of C8-BTBT, shown in **Figure 1.17d**. [121] Another commonly used coating technique is spin-coating where an OSC solution is dropped onto the target substrate, immediately followed by the substrate spinning around itself at a constant or accelerating speed. In this way, most of the solution diffuses out of the substrate, but the remaining solution crystallizes, as the solvent evaporates. [122, 123] Depositing a homogeneous film by spin-coating requires an optimization of a couple parameters such as solution concentration, solvent selection, spinning speed and duration. Especially, spinning speed plays a crucial role in the crystallization kinetics, thus significantly

influences the resulting film morphology. For instance, a solution of TIPS-pentacene:toluene was deposited by spin-coating at various spinning speeds ranging from 1000 to 2000 rpm, and the resulting film morphologies are presented in **Figure 1.18a**. During the deposition process, the evolution of the *001* Bragg peaks was monitored through in-situ GIWAXS measurements, as depicted in (i) of **Figure 1.18b**. The crystallization kinetics, shown in (ii), are characterized by changes in the *001* peak intensity with respect to the spinning time. The sharp increase in peak intensity indicates fast crystallization, followed by a slower crystallization phase until saturation, where the intensity levels off (see (i) of **Figure 1.18b**). The two-film morphology was compared in OFET configuration, the lowest speed of 1000 rpm gave a mobility of $2.2 \times 10^{-2} \text{ cm}^2 \text{ V}^{-1} \text{ s}^{-1}$, while the highest speed of 2000 rpm gave a lower mobility of $5 \times 10^{-4} \text{ cm}^2 \text{ V}^{-1} \text{ s}^{-1}$. Lastly, the relationship between crystallization kinetics and mobility reveals that achieving higher crystallinity requires a longer, slower crystallization process. This slower process allows for the formation of larger crystal grains and minimizes the presence of solvent residues in the thin film.[124]

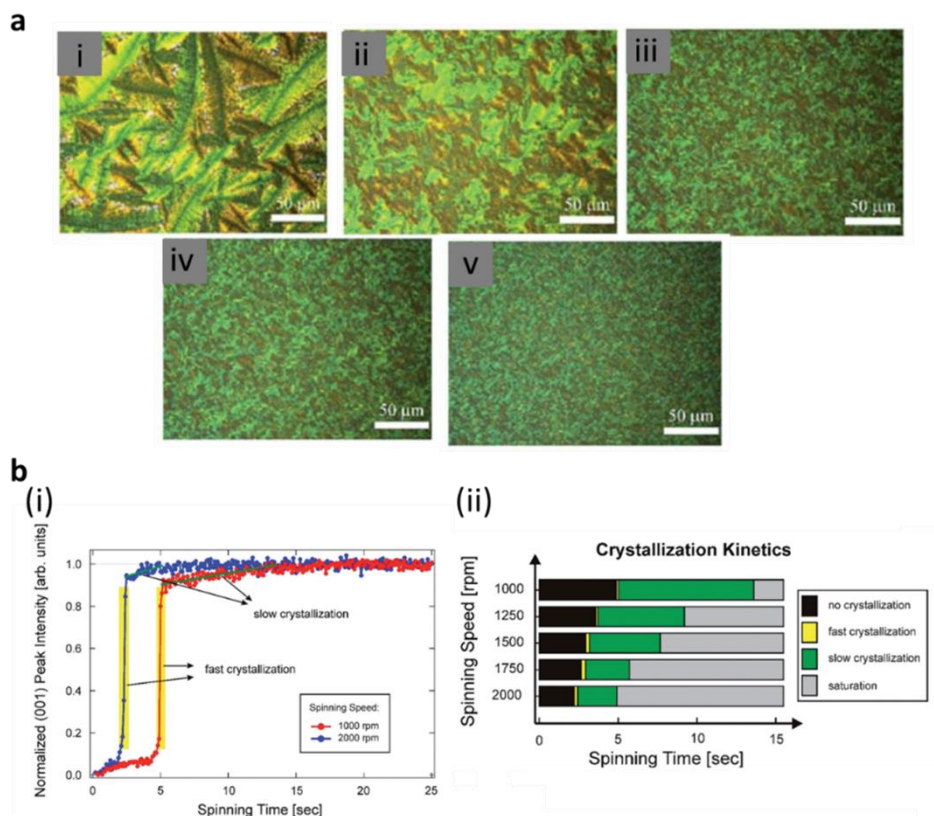


Figure 1.18 a) OM images of spin-coated TIPS-pentacene at different spinning speeds: (i) 1000 rpm, (ii) 1250 rpm, (iii) 1500 rpm, (iv) 1750 rpm and (v) 2000 rpm. b) (i) In-situ GIWAXS measurement during spin-coating was performed and the evolution of 001 peak (corresponding to interlayer distance) with respect to spinning time was tracked, (ii) crystallization kinetics were extracted from (i). (a, b) are from ref.[124].

Crystallization of an OSC polymer blend solution was induced by placing the substrate at an off – center position during spin-coating, as illustrated in **Figure 1.19a**. Deposition of a C8-BTBT:PS blend with on-center and off-center spin-coating revealed a notable difference in the crystal lattice structure. As seen in **Figure 1.19b**, the GIXD pattern for the on-center spin-coated C8-BTBT:PS blend discloses polycrystalline domains by broadened diffraction peaks. In contrast, when the same blend was off-center spin-coated, it showed a single crystal domain

with unity of diffraction peaks in the GIXD pattern. Such a difference was observed due to enhanced crystal growth of the C8-BTBT:PS blend in the radial direction when off-center spin-coated.[125] While spin-coating enables control over the crystallinity of OSCs, a considerable amount of the solution diffuses away from the substrate and is wasted. Moreover, achieving precise molecular orientation and alignment over large areas is difficult. In addition, spinning the substrate at high speed does not uniformly distribute the solution from the center of the substrate to the edges, resulting in a variation of film thickness and the presence of structural defects (unit cell deformation and grain boundaries).

Besides drop-casting and spin-coating, meniscus-guided coating (MGC) techniques such as dip-coating[126], slot-die coating[127], bar-assisted meniscus shearing[128] and zone-casting[129] have attracted enormous attention due to their ability to deposit highly crystalline and aligned thin films. Compared to drop-casting and spin-coating, MGC techniques enable the homogeneous deposition of materials over larger areas and offer the potential to control the molecular orientation and alignment. The first MGC technique employed on the industrial scale was slot – die coating used by Eastman Kodak in the 1950s to print rollable photographic papers.[130] Later, in the 1990s, this method was utilized to deposit organic materials for the application of photovoltaic cells, OFETs, organic electrochemical transistors (OECTs) and organic light-emitting diodes (OLEDs).[33] In general, MGC techniques rely on a solution forming a liquid meniscus between a coating head and a substrate. The substrate moves at a constant speed as the solvent evaporates, allowing the solute to crystallize and form the solid film.[87, 126, 131-133]

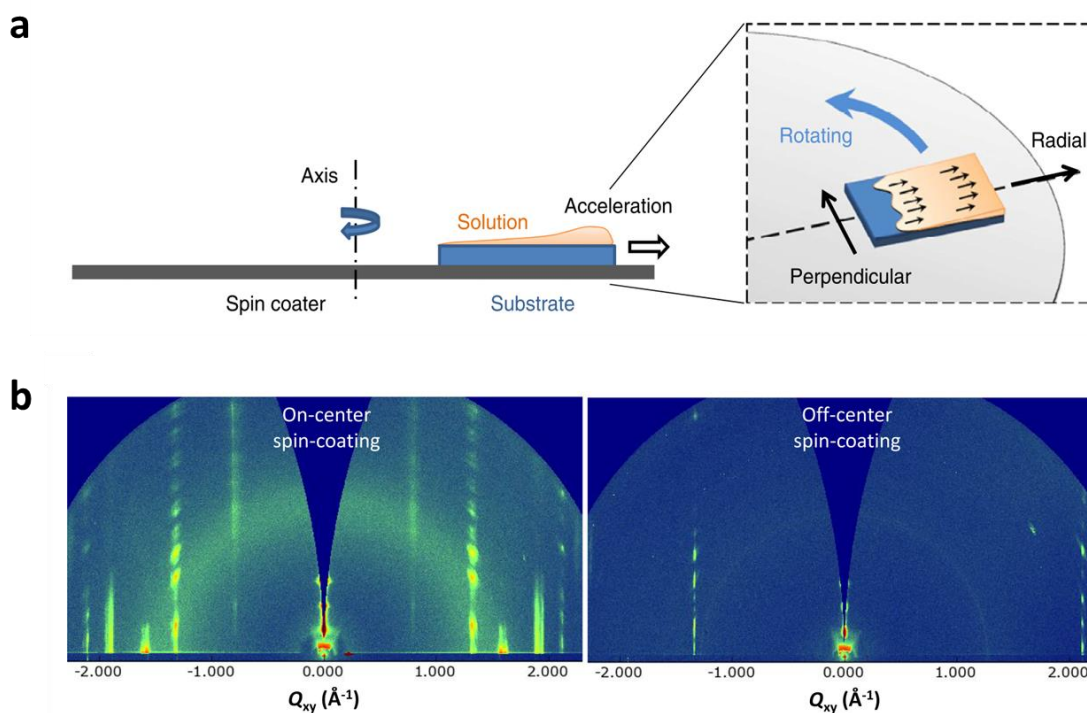


Figure 1.19 a) An illustration of off-center spin-coating (OCSC) method. b) The comparison of grazing incidence X-ray diffraction (GIXD) patterns of C8-BTBT:PS films deposited by on-centre and off-centre spin-coating. (a, b) are from ref.[125].

Deposition of an OSC by MGC requires defining several processing parameters such as casting speed, concentration, solvent selection, evaporation rate and gap distance between the coating head and the substrate.[134, 135] MGC techniques allow having control over the width, length and thickness of the film. **Figure 1.20a** reveals the relation between the casting speed and the film thickness of phospholipids, where the thickness follows a linear relation $h \sim v^{-1}$ with speed, this is called evaporation regime. Later, the film thickness makes a plateau in a small range of speed (mixed regime) then rises following a $h \sim v^{2/3}$ trend (Landau-Levich regime).[136] In the evaporation regime, the film crystallization is next to the front meniscus, but in Landau-Levich regime, the crystallization takes place out of the meniscus. This is because

the substrate at high casting speed drags the solution out by convective forces, so the wet film dries away from the meniscus.[134-136] A milestone work on controlling the OSC morphology through MGC deposition at different casting speeds (shear speed) was conducted by Bao et al.[116], as shown in **Figure 1.20b-c**. In this work, TIPS-pentacene was deposited using solution-shearing (one of the MGC methods, see **Figure 1.14**) at various speeds: (i) 0.4 mm s^{-1} , (ii) 1.6 mm s^{-1} , (iii) 2.8 mm s^{-1} , (iv) 4.0 mm s^{-1} , and (v) 8.0 mm s^{-1} , with the corresponding morphology images presented in **Figure 1.20b**. For a casting speed of 0.4 mm s^{-1} , oriented and millimeter-wide crystal domains with lengths up to a centimeter were observed. This trend continued at 1.6 mm s^{-1} and 2.8 mm s^{-1} , but the width of the crystal domains became narrower, and their length decreased. At 4.0 mm s^{-1} , the crystal domains transformed into comet-shaped morphologies, where the crystal width reduced to hundreds of micrometers and the length decreased to the millimeter range. At 8.0 mm s^{-1} , a spherulitic morphology was formed, which exhibited an orientation independent of the casting direction. The best performance among these morphologies in the OFET configuration was recorded at 2.8 mm s^{-1} , which achieved the highest saturation mobility, $\mu_{max} = 4.59 \text{ cm}^2 \text{ V}^{-1} \text{ s}^{-1}$, owing to the larger crystallite size (referring to the number of overlapping molecules within a domain of the lattice structure) in the casting direction, with the lowest density of grain boundaries compared to the other morphologies. **Figure 1.20c** presents the molecular packing of TIPS-pentacene thin films deposited by (i) evaporation and (ii) solution-shearing at 8.0 mm s^{-1} . As seen in **Figure 1.20c**, T1 and T2 represent molecular pairs indicating π - π stacking distances, distinguishing between the two deposition methods. T1 decreased from 3.33 \AA to 3.08 \AA when solution-sheared, while T2 increased from 3.49 \AA to 3.79 \AA . The latter revealed that solution-shearing provides a wide range of control possibilities over molecular packing, orientation, and charge transport. However, it should be underlined that the best-performing TIPS-pentacene film from solution-shearing in the OFET is not the one with the lowest π - π distance, because in the case of a thin

film deposited at 8.0 mm s^{-1} , it results in a high density of grain boundaries and defects.[116] In conclusion, the casting speed, as a deposition parameter in MGC, exerts a significant influence on the charge transport properties, thin film morphology, molecular packing, and orientation of OSC crystals. I have discussed the influence of a single parameter of MGC on OSC morphology and molecular packing. However, when casting speed is combined with other controllable parameters of MGC, the resulting effects remain unknown. Further investigations are needed to understand the relationship and effects of coupling multiple parameters in MGC.

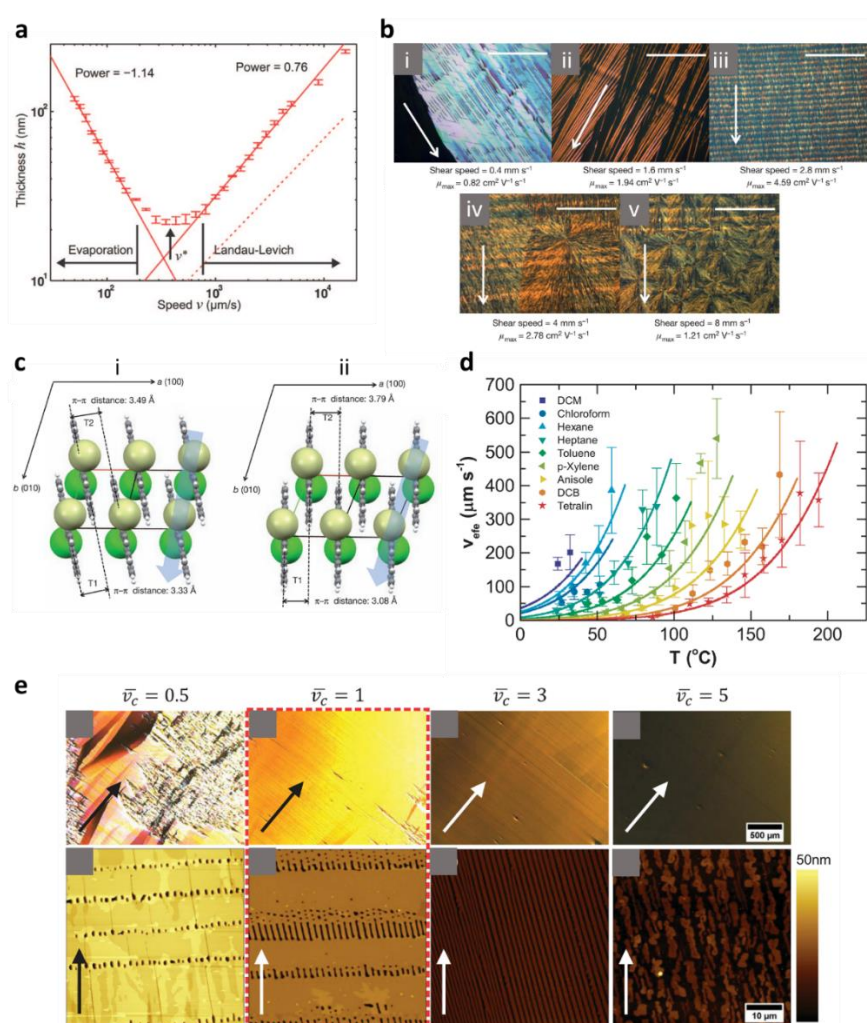


Figure 1.20 a) Film thickness h of phospholipids films as a function of casting speed v . [136] b) Cross-polarized OM images of solution-sheared TIPS-pentacene at various casting speeds with the highest saturation mobility obtained: (i) 0.4 mm s^{-1} with $\mu_{\text{max}} = 0.82 \text{ cm}^2 \text{ V}^{-1} \text{ s}^{-1}$, (ii)

1.6 mm s⁻¹ with 1.94 cm² V⁻¹ s⁻¹, (iii) 2.8 mm s⁻¹ with 4.59 cm² V⁻¹ s⁻¹, (iv) 4 mm s⁻¹ with 2.78 cm² V⁻¹ s⁻¹ and (v) 8 mm s⁻¹ with 1.21 cm² V⁻¹ s⁻¹. The scale bars correspond to 200 μm. c) Molecular packing of TIPS-pentacene thin films: (i) evaporated thin film and (ii) solution-sheared thin film at 8.0 mm s⁻¹. T1 and T2 denote molecular pairs forming π-π stacking. The blue arrow indicates the most efficient charge transport direction, wherein the casting direction for (ii) is b (010) axis. The (b) and (c) are from ref.[116]. d) Equilibrium front evaporation speed V_{efe} for nine different solvents as a function of substrate temperature. e) AFM and POM images of C8-BTBT films for variable casting speeds. All films were deposited at 50°C with C8-BTBT in heptane. The (d) and (e) are from ref.[87].

Moreover, the evaporation rate of the solvent, controlled by the substrate temperature, is very important influencing the film growth process.[134] Another milestone work by Janneck et al. presents the relation of equilibrium evaporation speed (V_{efe}) with respect to substrate temperature, as seen in **Figure 1.20d**. V_{efe} goes up with the substrate temperature, then reaches saturation, and the saturation point gradually follows the boiling temperature of the respective solvent. Accordingly, an optimal coating of organic thin films requires V_{efe} matching with the casting speed (v), thereby, the substrate motion retracts well the evaporating solvent and absorbing the solute. **Figure 1.20e** reveals AFM and POM images of zone-cast C8-BTBT thin films for different casting speeds, where $\bar{v}_c = V_{efe}/v$. The optimal morphology of the thin film was found for $\bar{v}_c = 1$ and it has the highest average effective mobility of 4.3 cm² V⁻¹ s⁻¹ among all morphologies.[87]

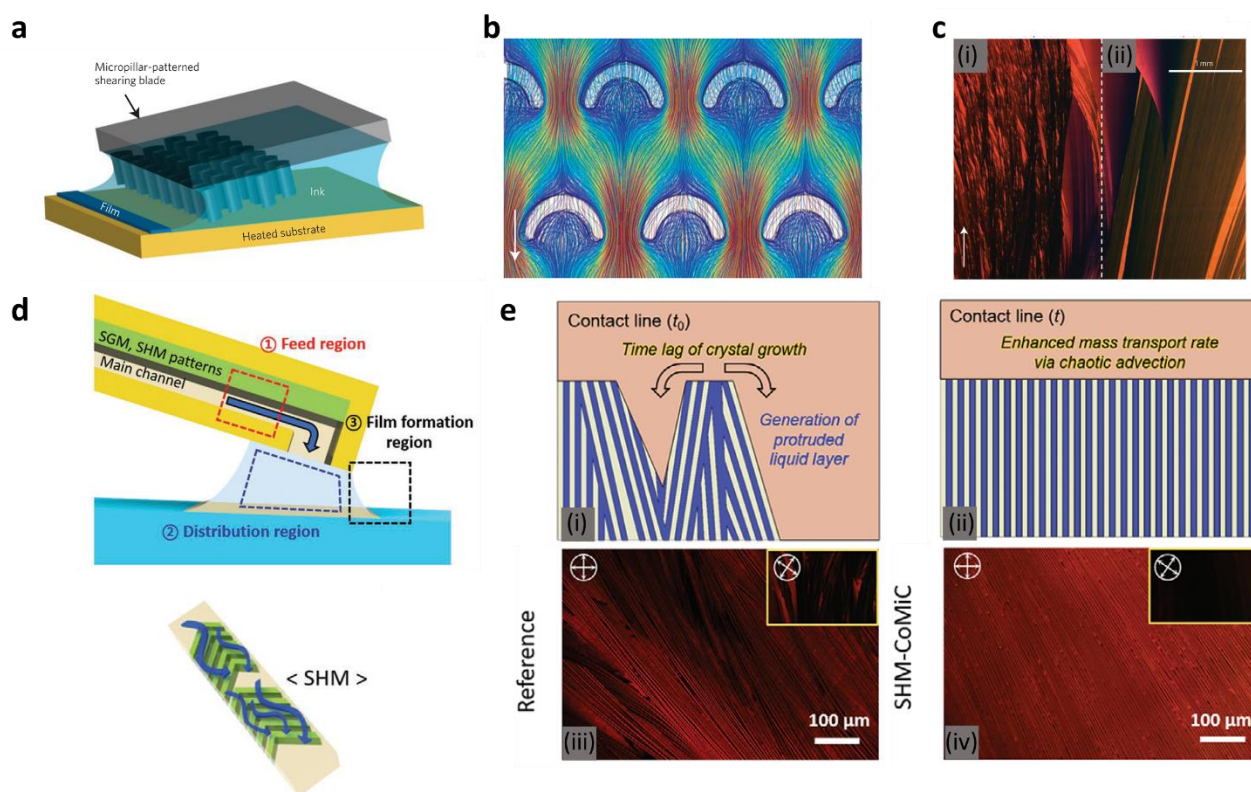


Figure 1.21 a) An illustration of solution-shearing modified by micropillar-patterned shearing blade. b) Simulated fluid flow of solution streamlines where the colors refer to the velocity of fluid flow ranging from 0.0 (deep blue) to 1.3 mm s⁻¹ (deep red). The arrow indicates the coating direction. c) POM images of TIPS-pentacene films deposited by solution-shearing with (ii) and without (i) micropillars. d) Schematic diagram of continuous-flow microfluidic-channel based meniscus-guided coating (CoMiC) that consist of three regions; the feed, distributions, and the film formation regions. A sketch of staggered herringbone microfluidic channel (SHM) stands at the bottom of CoMiC diagram. e) Schematic sketch of crystal growth process for (i) solution-shearing and (ii) CoMiC, and POM images of TIPS-pentacene films deposited by (iii) solution-shearing and (iv) CoMiC. (a, b, c) are from ref.[37] and (d, e) are from ref.[137].

Fluid flow in MGC refers to the motion of OSC solution during the thin film deposition. Controlling fluid-flow is one of the most important aspects to improve the crystallinity,

morphology and molecular organization of OSC thin films. Precisely tuning the fluid flow of MGC is required to improve the alignment of OSC crystals. Otherwise, poor mass transport to the nucleation site results in misaligned crystals. For instance, to enhance the fluid flow speed, a micropillar-shearing blade (**Figure 1.21a**) was developed in addition to conventional solution-shearing. Such micropillar-shearing blade induces an enhanced fluid flow as evidenced by the simulated fluid flow of solution streamlines in **Figure 1.21b**. In **Figure 1.21c**, the POM images of TIPS-pentacene films deposited with (ii) and without (i) micropillars clarify that an enhanced fluid flow improved the molecular alignment of TIPS-pentacene crystals in the coating direction. Correspondingly, the charge carrier mobility of the thin film was increased from (i) 2.3 to (ii) 8.1 cm² V⁻¹ s⁻¹.^[37] In another example, continuous-flow microfluidic-channel based meniscus-guided coating (CoMiC) (**Figure 1.21d**) is designed to upgrade conventional MGCs with an enhanced fluid flow and mass transport. **Figure 1.21e** demonstrates (i) poor mass transport or weak fluid flow results in a time lag during crystal growth that causes misalignment of crystals with respect to the coating direction, whereas in contrast, (ii) enhanced mass transport via chaotic advection by CoMiC-SHM (see **Figure 1.21d**) improved the crystal alignment by eliminating the time lag during crystal growth. The POM images of TIPS – pentacene films deposited with (iii) MGC and (iv) CoMiC-SHM evidences how mass transport plays a vital role on the molecular alignment at the contact line. Not only the crystal alignment changed but also the charge carrier mobility raised from (iii) 1 to (iv) 2 cm² V⁻¹ s⁻¹.^[137] To further understand the mechanism behind the morphological transitions and variations of MGC, one can look in the physics of MGC.

1.3.4 Physics of MGC

The physics of MGC combines theory and experimental observations to better understand the crystallization process, morphology and molecular packing of OSCs in terms of fluid dynamics, mass transport and heat transfer.

Advanced modelling for MGC was utilized in several studies to relate experimental observations to fluid dynamics.[128, 138, 139] In general, the Navier-Stokes (NS) equation (eqn. 10) is used to describe the fluid motion and the vapor phase.[140] It also corresponds to Newton's second law of motion for fluids. The NS eqn. is given by;

$$\rho \left(\frac{\partial u}{\partial t} + u \cdot \nabla u \right) = -\nabla p + \nabla \cdot \left(\mu (\nabla u + (\nabla u)^T) - \frac{2}{3} \mu (\nabla \cdot u) I \right) + F \quad (10)$$

where ρ is the fluid density, u the flow velocity, p the fluid pressure, μ the dynamic viscosity, T the temperature and F the external forces applied to the fluid. In another term, eqn. 10 states that inertial forces of fluid are equal to the sum of pressure forces, viscous forces and external forces. In addition, since the NS eqn. only includes conservation of momentum, the conservation of mass has to be obtained together with the NS eqn. by solving the continuity equation. The continuity eqn. in its general form is equal to;

$$\frac{\partial \rho}{\partial t} + \nabla \cdot (\rho u) = 0 \quad (11)$$

In eqn. 11, the time derivation of the fluid density indicates the accumulation or loss of mass in the system, while the divergence term refers to inflow or outflow. The continuity eqn. basically states that the mass entering the system is equal to the mass leaving the system and the mass within the system.

As a next step, the NS and continuity equations can be further simplified for MGC by specifying the flow regime. The dimensionless Reynolds number, $Re = \rho u L / \mu$, refers to the

ratio of inertial forces to viscous forces. A low Reynolds number ($Re \ll 1$) corresponds to a laminar flow, called Creeping flow (or Stokes flow); while a high Reynolds number ($Re \gg 1$) corresponds to turbulent flow. MGC in steady-state involves a laminar flow because the dynamic viscosity is a few orders of magnitude higher than inertial forces.[135] Another dimensionless parameter, the Mach number, $Ma = u/c$, expresses the ratio of the fluid velocity to the speed of sound in the fluid. It measures whether a fluid is compressible (high Ma) or incompressible (low Ma). Unlike compressible gases, the meniscus is incompressible as it is a fluid, the continuity eqn. then yields $\nabla u = 0$. Since the divergence of the velocity is equal to 0, we can remove the term $\frac{2}{3}\mu(\nabla \cdot u)I$ from eqn. 10. Moreover, since $Re \ll 1$ the inertial forces are very small, such that the term $\rho \left(\frac{\partial u}{\partial t} + u \cdot \nabla u \right)$ can also be neglected and removed from eqn. 10. Lastly, considering there is no external force and gravity has a minor effect on meniscus, we can remove F from eqn. 10 as well. Then, the NS eqn. reduces to;

$$0 = -\nabla p + \nabla \cdot (\mu(\nabla u + (\nabla u)^T)) \quad (12)$$

Until now, the motion of solvent is described in MGC using the NS and continuity equations. However, transport of a dilute solute dissolved in a solvent requires solving Fick's law of diffusion. It postulates that a fluid flow or a solute will go from a location of high concentration to a location of low concentration.[141] Driving forces by diffusion are solved by Fick's law, which applies when convection of solute pairs with a fluid flow via the fluid velocity u . [134]

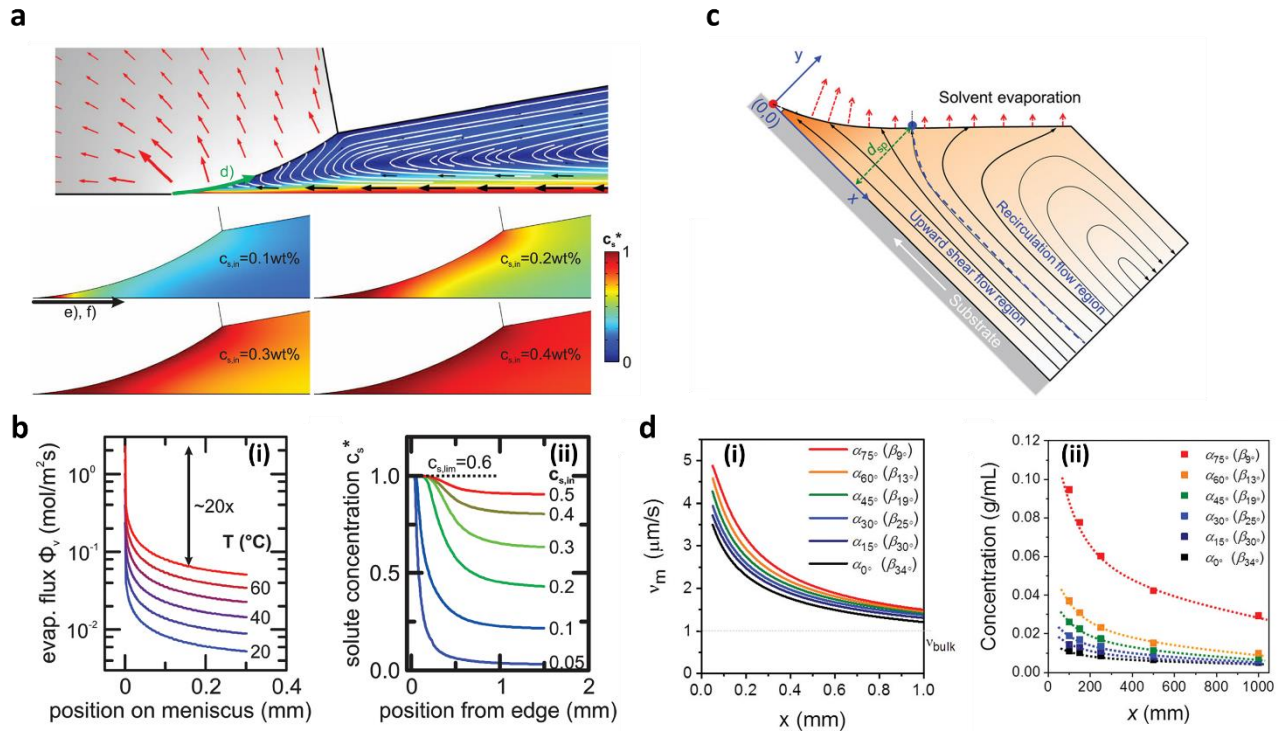


Figure 1.22 a) 2D simulation of zone – casting with heptane (process conditions: $T = 50^{\circ}\text{C}$ and $v = 90 \mu\text{m s}^{-1}$) for variable concentrations. Colors represent concentration from lowest (blue) to highest (red). b) (i) Evaporation flux ϕ_v as a function of position on meniscus (shown in (a) with a green arrow) and (ii) solute concentration c_s^* as a function of position from edge (shown in (a) with a black arrow). c) Fluid – flow simulation for angle dependent dip coating (ADDC). d) (i) Evaporation rate v_m and (ii) concentration as a function of x . x position is shown in (c).

To visualize realistically MGC in a simulation, the abovementioned equations are solved in a defined geometry of the meniscus.[128, 133, 139] For instance, **Figure 1.22a** shows how different solute concentration in an OSC solution affects the concentration gradient near the meniscus tip. Prior to this, boundary conditions were set for solvent evaporation at the meniscus interface, which decreases from the meniscus tip to the top of the interface. **Figure 1.22b** reveals (i) ‘evaporation rate of solvent (ϕ_v)’ at the interface as a function of ‘position on

meniscus' for different temperatures and (ii) 'solute concentration (c_s^*)' as a function of 'position from edge' for different solution concentrations. The substrate temperature varies from 20°C to 60°C that increases the 'evaporation rate of solvent' (i) for 'position on meniscus' but the maximum evaporation rate (at $x = 0$) remains the same at the meniscus tip and independent from substrate temperature. At a constant temperature of 50°C, the solute concentration depending on 'position from edge' (ii) increases gradually with increasing solution concentration. Therefore, higher concentration and improved solvent evaporation resulted in fewer defects in the film morphology due to sustained mass transfer to the supersaturating area of the solution.[139] Secondly, **Figure 1.22c** shows another example of MGC simulation, the angle dependent dip coating (ADDC) technique, which reveals that the rate of solvent evaporation and the concentration near the tip vary with the angle at which the substrate is pulled out from the OSC solution. From high to small angle β (liquid-substrate angle), **Figure 1.22d** reveals that the rate of solvent evaporation (i) and the concentration (ii) as a function of x goes up, explaining the improvement in the alignment and the coverage of the film.[133]

liquid transition phase) and reservoir zone (liquid film), where the coating direction is in the x -plane. Three differential equations (eqns. 13-15) are solved to calculate the variations in solute volume fraction $\phi(r, t)$, crystallinity $\eta_i(r, t)$ and normalized height $h(r, t)$. Eqn. 13 is a generalized diffusion equation, where the derivative of time of $\phi(r, t)$ changes with respect to the volumetric evaporative flux $\sigma_B(r, t)$ in which σ_B depends on the evaporative mass transport coefficient $k_e(x, t)$ and the chemical potential of the solvent. Eqn. 14 is the Allen-Cahn eqn. describing the dynamics of the non-conserved parameter. Lastly, eqn. 15 expresses the local changes in height. The terms $\Lambda(\phi)$ and $\Gamma(\phi)$ denote to the concentration dependent mobility and a kinetic coefficient, being functions of the self-diffusivity D_i and the mass transfer coefficient k_c . The structure formation is driven by minimization of the Helmholtz free energy $\mathcal{F}(\phi, \eta_i, \nabla\phi, \nabla\eta_i)$, which is a function of ϕ , η_i and their variation in Cartesian coordinates represented by $\nabla\phi$ and $\nabla\eta_i$. The term $\frac{\delta\mathcal{F}}{\delta\phi}$ corresponds to the exchange chemical potential, and the terms for thermal fluctuations in solute volume fraction and crystallinity are represented by θ_ϕ and θ_{η_i} . [142]

$$\frac{\partial\phi(\mathbf{r}, t)}{\partial t} = h(\mathbf{r}, t)^{-1} \nabla \cdot h(\mathbf{r}, t) \Lambda(\phi) \nabla \frac{\delta\mathcal{F}}{\delta\phi} + h(\mathbf{r}, t)^{-1} \phi(\mathbf{r}, t) \sigma_B(\mathbf{r}, t) + \theta_\phi(\mathbf{r}, t) \quad (13)$$

$$\frac{\partial\eta_i(\mathbf{r}, t)}{\partial t} = \Gamma(\phi) \frac{\delta\mathcal{F}}{\delta\eta_i} + \theta_{\eta_i}(\mathbf{r}, t) \quad (14)$$

$$\frac{\partial h(\mathbf{r}, t)}{\partial t} = -\sigma_B(\mathbf{r}, t) \quad (15)$$

As shown in **Figure 1.23a**, the evaporative mass transfer coefficient $\tilde{k}_e(\tilde{x}, \tilde{t})$ is defined between a limiting factor \tilde{k}_e^∞ for $\tilde{x} \ll \tilde{x}_{eb}$ and zero for $\tilde{x} \gg \tilde{x}_{eb}$. The characteristic length and timescales, λ and τ , are introduced in the simulation and the dimensionless coordinates $\tilde{x} = x/\lambda$, $\tilde{y} = y/\lambda$ and height $\tilde{h} = h/\lambda$, self-diffusivities $\tilde{D}_i = D_i\tau/\lambda^2$, mass transfer coefficients $\tilde{k}_e = k_e\tau/\lambda$ and $\tilde{k}_c = k_c\tau$, and coating speed $\tilde{U} = U\tau/\lambda$ are used. **Figure 1.23a** displays the initial conditions where $\{\phi_0, \tilde{h}_0, \tilde{k}_e\}$ was set in the reservoir zone, and their

translation across the evaporation border at $x = \tilde{x}_{eb}$. The corresponding revolution of solute volume fraction ϕ , crystallinity η_i and normalized height h are shown in the simulation domain by **Figure 1.24a** for a constant speed $\tilde{U} = 0.929$ ($496 \mu\text{m s}^{-1}$). Moreover, **Figure 1.24b** presents the morphologies of zone-cast DPP(Th_2Bn)₂ for variable speeds in the range $50 \mu\text{m s}^{-1} < \tilde{U} < 1000 \mu\text{m s}^{-1}$.

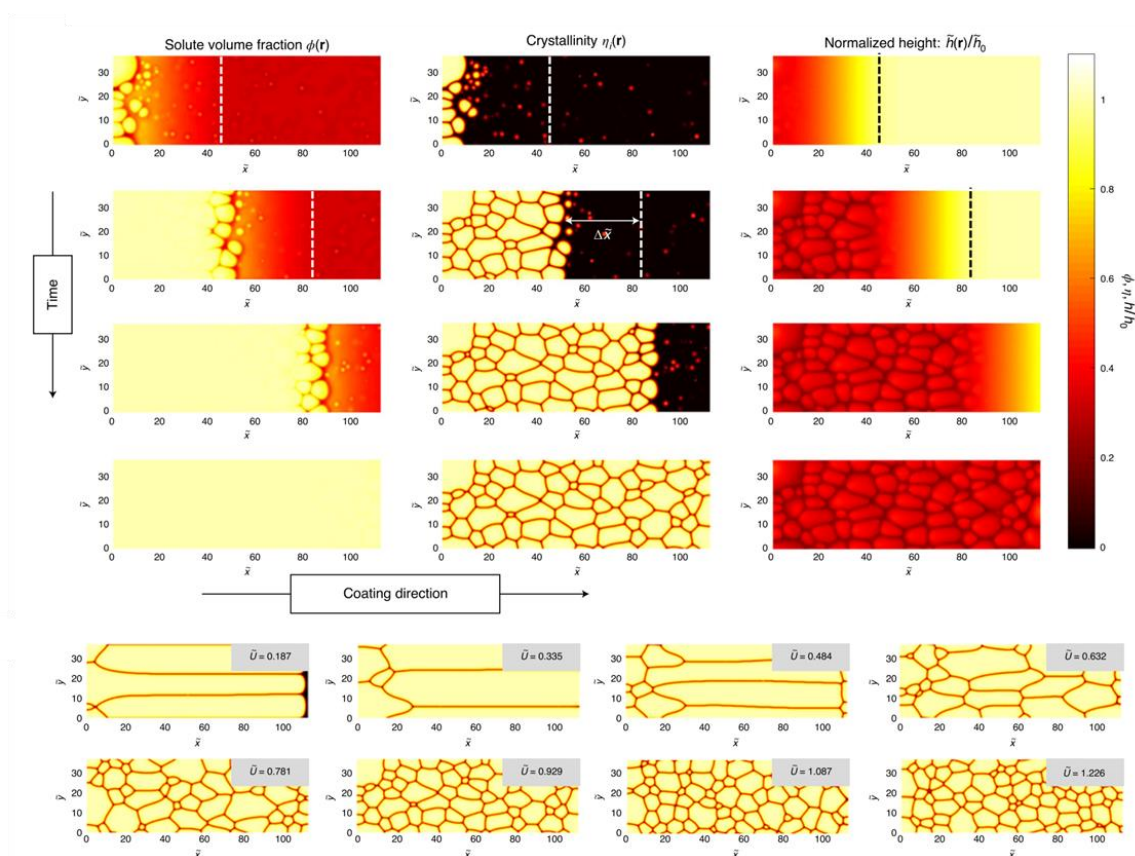


Figure 1.24 Numerical simulation of dry-film morphologies (crystallinity) as a function of casting speed.[142]

Figure 1.24a and **1.24b** exhibits the morphologies by simulation (crystallinity η_i) and experiment, where the speed varies in the range $0.187 < \tilde{U} < 1.226$ ($\sim 100 - 655 \mu\text{m s}^{-1}$). At this speed range, DPP(Th_2Bn)₂ films formed two sub-morphological regimes, aligned band for speeds $< 100 \mu\text{m s}^{-1}$ and impinged domain-like morphologies for speeds $> 100 \mu\text{m s}^{-1}$. Another

important trend seen in the morphology evolution with increasing speed is that the domain size becomes smaller for the impinged domain-like morphology, meaning that the grain boundary density of the film rises. The simulation results shown in **Figure 1.24a** successfully matched with the POM images shown in **Figure 1.23b**, proving that the experimental morphologies of MGC deposited DPP(Th₂Bn)₂ films can be predicted by the model in terms of crystal orientation, grain boundaries between crystals, and height of the film. Especially, the prediction of the grain boundary density in OSCs is vital because it defines the electrical behavior of OFETs. In the second part of this work, it is shown that the film deposited at low coating speed $\tilde{U} = 0.187$ (100 $\mu\text{m s}^{-1}$) exhibiting impinged domain-like morphology with lower grain boundary density obtained the highest average charge carrier mobility $\sim 1.1 \text{ cm}^2 \text{ V}^{-1} \text{ s}^{-1}$. [111] The power of a numerical analysis of the crystallization is demonstrated by the correlation between the electrical behavior of OFETs and the simulation's morphology prediction. For more detailed information, we refer to ref. [111, 142].

Finally, numerical simulations of the coating bead and the crystallization give an insight to understand the crystallization behavior of OSCs and explain the morphology formation mechanism and transitions between morphologies. Therefore, it is beneficial to use the concept based on the theoretical and experimental results to determine more systematic design rules for the future applications of MGC. In addition, numerical simulations of the crystallization discussed in **Figure 1.23** and **1.24** to predict the morphology were applied to a small molecule OSC, extension of the model to polymer based OSCs is still in need.

1.4 Motivation

OFET performance has been improved over decades from 10^{-3} to $20 \text{ cm}^2 \text{ V}^{-1} \text{ s}^{-1}$ [35], mainly owing to the synthesis of novel compounds [143], development of Ohmic contacts [95]

and control of OSC morphology[114]. Especially, control of OSC morphology using solution processing techniques has taken great attention.[37, 73, 116, 134]

MGC principally allows controlling the morphology from macroscopic domains[111] to unidirectionally aligned crystals[86], which is of particular interest to OFETs due to efficient in-plane unidirectional charge transport between source and drain electrodes. However, the mechanism affecting the morphology during film growth, the impact of fluid dynamics on OSC crystallization and the relation between the deposition parameters were not understood well. Particularly, to scale up MGC, combined experimental and computational models are required. So far, optimization of processing parameters in MGC and understanding of fluid dynamics behind OSC crystallization behavior for low molecular OSCs are still missing.

1.4.1 Optimal processing window by meniscus-guided coating

OSC deposition with MGC requires adjustment of several parameters, the most important being the casting speed and solution concentration. Thus far, pioneering studies have shown that the casting speed controls the film thickness[136] and superior morphology is obtained when it matches with the evaporation rate of the solvent[87]. On the other hand, the solution concentration increases the concentration gradient near the contact line, hence results fewer defects in thin film morphology.[139] However, there is no research investigating the coupling between casting speed and solution concentration as well as defining optimal processing conditions.

In chapter 2, I focus on MGC deposited C8-BTBT morphologies by varying the casting speed and solution concentration. Herein, the aim is to comprehend the impact of coupling

parameters (casting speed and solution concentration) on the molecular arrangement, surface morphology of low molecular weight OSC C8-BTBT, and charge transport behavior in OFETs.

1.4.2 Tuning crystallization of OSC via controlled meniscus shape

In MGC, the misalignment of OSC crystals was shown to originate from the time lagging of solute transport to nucleation sites and meniscus instability during crystallization.[37, 137] To ensure stability, a comprehensive understanding of the meniscus shape and defining an optimal height between the coating head and the substrate is essential. This height also defines the size of the actively evaporating front meniscus. So far, there is no guide describing an ideal coating height between the coating head and the substrate. In chapter 3, I investigate the role of the meniscus shape on fluid dynamics in the coating bead and the crystallization process of TIPS-pentacene during zone-casting.

1.4.3 Precise patterning OSC during meniscus-guided coating

The electronic applications of OFETs such as radio frequency identification devices (RFID), complementary logic circuits and sensor arrays require a precise patterning of OSCs in order to reduce the leakage current and crosstalk between neighboring devices.[144-146]

Patterning OSC on a channel area of a transistor was already realized using different methods. Most common strategies are mold-assisted OSC patterning[147, 148] and wettability guided crystallization of OSCs using patterned SAMs[149-151].

Especially, combining the MGC technique with wettability guided crystallization was not understood in terms of definition of coating parameters and their limits. On an unwettable SAM surface, MGC application results in no film formation. Oppositely, a wettable surface

allows the crystallization and formation of a solid film. However, when a surface includes both unwettable and wettable regions, application of MGC results in a simultaneously tilted contact angle, with a low contact angle on the wettable region and a high contact angle on the unwettable region. In chapter 4, the crystallization behaviour of TIPS-pentacene during MGC with wettability guidance is investigated.

References

1. Mayo, J.S., *The Role of Microelectronics in Communication*. Scientific American 1977. **237**(3): p. 192–209.
2. Chan, C.C., *An overview of electric vehicle technology*. Proceedings of the IEEE, 1993. **81**(9): p. 1202-1213.
3. Markowski, S., Jubb, C. D., *The Impact of Microelectronics on Scale in Manufacturing Industries*. Australian Journal of Management, 1989. **14**(2): p. 171–210.
4. Mocerino, C., *Digital revolution in efficient self-organization of buildings: towards intelligent robotics*. Energy and Sustainability for Small Developing Economies (ES2DE), 2018: p. 1-6.
5. D.R., L., *Dopant materials used in the microelectronics industry*. Occupational Medicine (Philadelphia, Pa.), 1986 **1**: p. 35-47.
6. Loreto, M.F., M. , *Review of energy harvesting techniques and applications for microelectronics*. VLSI Circuits and Systems II, 2005.
7. Bonnaud, O.F., L. , *Microelectronics at the heart of the digital society: technological and training challenges*. 34th Symposium on Microelectronics Technology and Devices (SBMicro), 2019 p. 1-4.
8. *Basic Research Needs for Microelectronics*. 2018. Report of Department of Energy Office of Science Workshop, October 23-25, 2018: Argonne National Laboratory.
9. Van Houten, H., *Physics, Materials Science, and Trends in Microelectronics*, in *Future Trends in Microelectronics*, S. Luryi, Xu, J., Zaslavsky, A. , Editor. 1996, Springer.
10. Vyas, P., *Analysis and Design of MOSFET Based Amplifier in Different Configurations*, in *2nd National conference in Intelligent Computing & Communication*. 2013.
11. Um, C.N.a.Y., *Switching MOSFET*, in *Multiband Dual-Function CMOS RFIC Filter-Switches 2020*, Springer, Cham.

12. Plett, C., Rogers, J., *Radio Frequency Integrated Circuit Design, Second Edition*. Artech, 2010.
13. Liang, J.X.L., S. K., *Audio Power Amplifier Design and Debugging*. Applied Mechanics and Materials, 2014: p. 651–653, , 2269–2272.
14. D. G. Elliott, M.S., W. M. Snelgrove, C. Cojocar and R. Mckenzie, *Computational RAM: implementing processors in memory*. IEEE Design & Test of Computers, 1999. **16**(1): p. 32-41.
15. Patterson, D.A.H., John L., *Computer Organization and Design MIPS Edition: The Hardware/Software Interface* Elsevier Inc. 2009.
16. Bardeen, J. and Brattain, W.H., *The Transistor, A Semi-Conductor Triode*. Physical Review, 1948. **74**(2): p. 230-231.
17. Hoddeson, L., *The Discovery of the Point-Contact Transistor* Historical Studies in the Physical Sciences, 1981. **12**(1): p. 41–76.
18. Shockley, W., *Circuit element utilizing semiconductive material*. 1948.
19. William Bradford Shockley, J.B.a.W.H.B., *Nobel Prize in Physics*. 1956.
20. J. J. Liou, A.O.-C., F. Garcia-Sanchez, *MOSFET physics and modeling*, in *Analysis and Design of Mosfets*. 1998.
21. Wanlass, F.M., *Low Stand-by Power Complementary Field-Effect Circuitry*. 1967: USA.
22. Abbas, K., *Handbook of Digital CMOS Technology, Circuits, and Systems*. 2020: Springer Cham.
23. H. Koezuka, A.T., T. Ando, *Field-effect transistor with polythiophene thin film*. Synthetic Metals, 1987. **18**(1-3): p. 699-704.
24. Tsumura, A., H. Koezuka, and T. Ando, *Macromolecular electronic device: Field-effect transistor with a polythiophene thin film*. Applied Physics Letters, 1986. **49**(18): p. 1210-1212.
25. Zhong, Y., et al., *A review on the GaN-on-Si power electronic devices*. Fundamental Research, 2022. **2**(3): p. 462-475.
26. Bronstein, H., et al., *The role of chemical design in the performance of organic semiconductors*. Nature Reviews Chemistry, 2020.
27. Wuttig, M., et al., *Revisiting the Nature of Chemical Bonding in Chalcogenides to Explain and Design their Properties*. Adv Mater, 2022: p. e2208485.

28. Tremel, W., *The Electronic Structure and Chemistry of Solids. Von P. A. Cox. Oxford University Press, Oxford 1987.259 s., Paperback, £ 12.50. — ISBN 0-19-855204-1.* *Angewandte Chemie*, 1988. **100**(5): p. 743-743.
29. Veaceslav Coropceanu, J.C., Demetrio A. da Silva Filho, Yoann Olivier, Robert Silbey, and and J.-L. Bredas, *Charge Transport in Organic Semiconductors.* *Chemical Reviews*, 2007. **107**: p. 926-952.
30. Mei, Y., et al., *Crossover from band-like to thermally activated charge transport in organic transistors due to strain-induced traps.* *Proceedings of the National Academy of Sciences of the United States of America*, 2017. **114**(33): p. E6739-E6748.
31. Someya, T., Z. Bao, and G.G. Malliaras, *The rise of plastic bioelectronics.* *Nature*, 2016. **540**(7633): p. 379-385.
32. Bao, Z. and X. Chen, *Flexible and Stretchable Devices.* *Advanced Materials*, 2016. **28**(22): p. 4177-9.
33. Liu, K., et al., *Advances in flexible organic field-effect transistors and their applications for flexible electronics.* *npj Flexible Electronics*, 2022. **6**(1).
34. Kang, B., W.H. Lee, and K. Cho, *Recent advances in organic transistor printing processes.* *ACS Applied Materials Interfaces*, 2013. **5**(7): p. 2302-15.
35. Paterson, A.F., et al., *Recent Progress in High-Mobility Organic Transistors: A Reality Check.* *Advanced Materials*, 2018: p. e1801079.
36. Ghamari, P., M.R. Niazi, and D.F. Perepichka, *Improving Environmental and Operational Stability of Polymer Field-Effect Transistors by Doping with Tetranitrofluorenone.* *ACS Applied Materials Interfaces*, 2023. **15**(15): p. 19290-19299.
37. Diao, Y., et al., *Solution coating of large-area organic semiconductor thin films with aligned single-crystalline domains.* *Nature Materials*, 2013. **12**(7): p. 665-71.
38. Chen, X., et al., *Balancing the film strain of organic semiconductors for ultrastable organic transistors with a five-year lifetime.* *Nature Communications*, 2022. **13**(1): p. 1480.
39. Dong, H., et al., *25th anniversary article: key points for high-mobility organic field-effect transistors.* *Advanced Materials*, 2013. **25**(43): p. 6158-83.
40. Sirringhaus, H., *25th anniversary article: organic field-effect transistors: the path beyond amorphous silicon.* *Advanced Materials*, 2014. **26**(9): p. 1319-35.

41. Lin, P. and F. Yan, *Organic thin-film transistors for chemical and biological sensing*. *Advanced Materials*, 2012. **24**(1): p. 34-51.
42. Blom, P.W.M., *Polymer Electronics: To Be or Not to Be?* *Advanced Materials Technologies*, 2020. **5**(6).
43. Esro, M., et al., *Structural and Electrical Characterization of SiO(2) Gate Dielectrics Deposited from Solutions at Moderate Temperatures in Air*. *ACS Applied Materials Interfaces*, 2017. **9**(1): p. 529-536.
44. Patil, B.B., et al., *Electrode and dielectric layer interface device engineering study using furan flanked diketopyrrolopyrrole-dithienothiophene polymer based organic transistors*. *Scientific Reports*, 2020. **10**(1): p. 19989.
45. Peng, J., et al., *Low-temperature solution-processed alumina as gate dielectric for reducing the operating-voltage of organic field-effect transistors*. *Applied Physics Letters*, 2013. **103**(6).
46. Małachowski, M. and J. Żmija, *Organic field-effect transistors*. *Opto-Electronics Review*, 2010. **18**(2).
47. V. R, R., et al., *Influence of Polymer Gate Dielectric on Organic Field-Effect Transistors: Interdependence of Molecular Weight, Solvent Polarity, and Surface Energy—A Case Study with PMMA and Pentacene*. *Macromolecular Materials and Engineering*, 2021. **307**(3).
48. Mark E. Roberts, N.Q., Stefan C. B. Mannsfeld, Benjamin N. Reinecke, and Z.B. Wolfgang Knoll, *Cross-Linked Polymer Gate Dielectric Films for Low-Voltage Organic Transistors*. *Chemistry of Materials*, 2009. **21**.
49. *IEEE Standard Definitions of Terms for Radio Wave Propagation*. IEEE Standards, 1997: p. 1-39.
50. Yim, K., et al., *Novel high- κ dielectrics for next-generation electronic devices screened by automated ab initio calculations*. *NPG Asia Materials*, 2015. **7**(6): p. e190-e190.
51. L. F. Chen, C.K.O., C. P. Neo, V. V. Varadan, V. K. Varadan, *Microwave Electronics: Measurement and Materials Characterization*. 2004: John Wiley & Sons, Ltd.
52. Burg, D. and J.H. Ausubel, *Moore's Law revisited through Intel chip density*. *PLoS One*, 2021. **16**(8): p. e0256245.
53. Wang, B., et al., *High- k Gate Dielectrics for Emerging Flexible and Stretchable Electronics*. *Chemical Reviews*, 2018. **118**(11): p. 5690-5754.

54. Robert H., Dennard, L., Fritz H., et al., *Design of Ion-Implanted MOSFET'S with Very Small Physical Dimensions*. IEEE Journal of Solid State Circuits, 1974.
55. Williams, R.K., et al., *The Trench Power MOSFET: Part I—History, Technology, and Prospects*. IEEE Transactions on Electron Devices, 2017. **64**(3): p. 674-691.
56. Tomita, K., et al., *Process Optimization of Trench Field Plate Power MOSFETs with Sequential Phosphorus-Doped Silicon*, in *2020 International Symposium on Semiconductor Manufacturing (ISSM)*. 2020. p. 1-4.
57. Chi T. Cao, L., Hakim, L., & Hsu, S.-H., *Boron Doping in Next-Generation Materials for Semiconductor Device*. 2022: IntechOpen.
58. Maitra, S., *Study of the Variation of the Threshold Voltage with the Doping Concentration and Channel Length* 2017, IEEE Xplore.
59. Haijiang, Y., et al., *Ion implanted AlGa_N-Ga_N HEMTs with nonalloyed Ohmic contacts*. IEEE Electron Device Letters, 2005. **26**(5): p. 283-285.
60. A. Akihiro, L.A.S., A. Mauro, A. Takuzo, A. Giuseppe, A.A. Christine, A. R. Harry, A. Geoffrey, A.S. Norman, A.M. Sahar, A.J. Allan, A. Patrick, A.C. Robert, A.C. Jett, Jr. and A.D.T. Edward, *Comprehensive Polymer Science and Supplements*. 1996: Elsevier Ltd. .
61. Mishra, A. and P. Bauerle, *Small molecule organic semiconductors on the move: promises for future solar energy technology*. Angewandte Chemie, 2012. **51**(9): p. 2020-67.
62. Hotta, S., et al., *Organic single-crystal light-emitting field-effect transistors*. Journal of Materials Chemistry C, 2014. **2**(6): p. 965-980.
63. Morab, S., M.M. Sundaram, and A. Pivrikas, *Review on Charge Carrier Transport in Inorganic and Organic Semiconductors*. Coatings, 2023. **13**(9).
64. Kano, M., T. Minari, and K. Tsukagoshi, *Improvement of subthreshold current transport by contact interface modification in p-type organic field-effect transistors*. Applied Physics Letters, 2009. **94**(14).
65. Hyun Kim, C., et al., *Modeling the low-voltage regime of organic diodes: Origin of the ideality factor*. Journal of Applied Physics, 2011. **110**(9).
66. Xu, Y., et al., *Development of high-performance printed organic field-effect transistors and integrated circuits*. Physical Chemistry Chemical Physics, 2015. **17**(40): p. 26553-74.

67. Scharfetter, D.L., *Minority Carrier Injection and Charge Storage in Epitaxial Schottky Barrier Diodes*, Solid-State Electronics Pergamon Press 1965. **8**: p. 299-311.
68. Tung, R.T., *The physics and chemistry of the Schottky barrier height*. Applied Physics Reviews, 2014. **1**(1).
69. Peng, B., et al., *Crystallized Monolayer Semiconductor for Ohmic Contact Resistance, High Intrinsic Gain, and High Current Density*. Advanced Materials, 2020. **32**(34): p. e2002281.
70. Minder, N.A., et al., *Band-like electron transport in organic transistors and implication of the molecular structure for performance optimization*. Advanced Materials, 2012. **24**(4): p. 503-8.
71. Liu, C., et al., *Solution-processable organic single crystals with bandlike transport in field-effect transistors*. Advanced Materials, 2011. **23**(4): p. 523-6.
72. Podzorov, V., et al., *Intrinsic charge transport on the surface of organic semiconductors*. Physical Review Letters, 2004. **93**(8): p. 086602.
73. Lim, J.A., et al., *Control of the Morphology and Structural Development of Solution-Processed Functionalized Acenes for High-Performance Organic Transistors*. Advanced Functional Materials, 2009. **19**(10): p. 1515-1525.
74. Asadi, K., et al., *Polaron hopping mediated by nuclear tunnelling in semiconducting polymers at high carrier density*. Nature Communications, 2013. **4**: p. 1710.
75. Yu, H., et al., *Efficient Intermolecular Charge Transport in pi-Stacked Pyridinium Dimers Using Cucurbit[8]uril Supramolecular Complexes*. Journal of American Chemical Society, 2022. **144**(7): p. 3162-3173.
76. Schweicher, G., et al., *Molecular Semiconductors for Logic Operations: Dead-End or Bright Future?* Advanced Materials, 2020. **32**(10): p. e1905909.
77. N. Boden, R.J.B., J. Clements, B. Movaghar, K. J. Donovan, T. Kreuzis, Physical Reviews B, 1995. **52**: p. 13274.
78. N.-E. Lee, J.-J.Z., L. A. Agapito, M. Bernardi, Physical Review B, 2018. **97**: p. 115203.
79. Ostroverkhova, O., *Organic Optoelectronic Materials: Mechanisms and Applications*. Chemical Reviews, 2016. **116**(22): p. 13279-13412.
80. Schweicher, G., et al., *What Currently Limits Charge Carrier Mobility in Crystals of Molecular Semiconductors?* Israel Journal of Chemistry, 2014. **54**(5-6): p. 595-620.
81. Fratini, S., et al., *A map of high-mobility molecular semiconductors*. Nature Materials, 2017. **16**(10): p. 998-1002.

82. Fratini, S., D. Mayou, and S. Ciuchi, *The Transient Localization Scenario for Charge Transport in Crystalline Organic Materials*. *Advanced Functional Materials*, 2016. **26**(14): p. 2292-2315.
83. Pfattner, R., C. Rovira, and M. Mas-Torrent, *Organic metal engineering for enhanced field-effect transistor performance*. *Physical Chemistry Chemical Physics*, 2015. **17**(40): p. 26545-52.
84. Beena Unni, A., et al., *Influence of Surface Roughness on the Dynamics and Crystallization of Vapor-Deposited Thin Films*. *Journal of Physical Chemistry B*, 2022. **126**(40): p. 8072-8079.
85. Zhang, F., et al., *Critical Role of Surface Energy in Guiding Crystallization of Solution-Coated Conjugated Polymer Thin Films*. *Langmuir*, 2018. **34**(3): p. 1109-1122.
86. Janneck, R., et al., *Influence of the Surface Treatment on the Solution Coating of Single-Crystalline Organic Thin-Films*. *Advanced Materials Interfaces*, 2018. **5**(12): p. 1-9.
87. Janneck, R., et al., *Predictive Model for the Meniscus-Guided Coating of High-Quality Organic Single-Crystalline Thin Films*. *Advanced Materials*, 2016. **28**(36): p. 8007-8013.
88. Luo, L. and Z. Liu, *Recent progress in organic field-effect transistor-based chem/bio-sensors*. *View*, 2022. **3**(1).
89. Gundlach, D.J., et al., *Contact-induced crystallinity for high-performance soluble acene-based transistors and circuits*. *Nature Materials*, 2008. **7**(3): p. 216-21.
90. Kim, C.H., Y. Bonnassieux, and G. Horowitz, *Fundamental Benefits of the Staggered Geometry for Organic Field-Effect Transistors*. *IEEE Electron Device Letters*, 2011. **32**(9): p. 1302-1304.
91. Matsui, H. (2021). Device Physics of Organic Field-effect Transistors. In *Organic Semiconductors for Optoelectronics*, H. Naito (Ed.). <https://doi.org/10.1002/9781119146131.ch10>
92. Horowitz, G., et al., *The Concept of "Threshold Voltage" in Organic Field-Effect Transistors*. *Advanced Materials*, 1998. **10**(12): p. 923-927.
93. Misra, V. and M.C. Öztürk, *3 - Field Effect Transistors*, in *The Electrical Engineering Handbook*, W.-K. Chen, Editor. 2005, Academic Press: Burlington. p. 109-126.
94. Liu, C., Y. Xu, and Y.-Y. Noh, *Contact engineering in organic field-effect transistors*. *Materials Today*, 2015. **18**(2): p. 79-96.

95. Waldrip, M., et al., *Contact Resistance in Organic Field-Effect Transistors: Conquering the Barrier*. *Advanced Functional Materials*, 2019. **1904576**: p. 1-31.
96. Xu, Y., et al., *Precise Extraction of Charge Carrier Mobility for Organic Transistors*. *Advanced Functional Materials*, 2019. **30**(20).
97. Minari, T., et al., *Highly enhanced charge injection in thienoacene-based organic field-effect transistors with chemically doped contact*. *Applied Physics Letters*, 2012. **100**(9).
98. Boyu Peng, H.Y.L., Ming Chen, and Paddy K. L. Chan, *Realization of Ohmic-contact and velocity saturation in organic field-effect transistors by crystallized monolayer*
99. Casalini, S., et al., *Self-assembled monolayers in organic electronics*. *Chemical Society Reviews*, 2017. **46**(1): p. 40-71.
100. Hutchins, D.O., et al., *Effects of self-assembled monolayer structural order, surface homogeneity and surface energy on pentacene morphology and thin film transistor device performance*. *Journal of Materials Chemistry C*, 2013. **1**(1): p. 101-113.
101. Borchert, J.W., et al., *Small contact resistance and high-frequency operation of flexible low-voltage inverted coplanar organic transistors*. *Nature Communications*, 2019. **10**(1): p. 1119.
102. Kawasaki, M., et al., *Reduction of Contact Resistance between Organic Semiconductor and Electrodes with Thiol-Based Self-Assembled Monolayer in Low-Density and Lying-Down Phase*. *Japanese Journal of Applied Physics*, 2008. **47**(8): p. 6247-6250.
103. Chen, M., et al., *Anthracene-based semiconductors for organic field-effect transistors*. *Journal of Materials Chemistry C*, 2018. **6**(28): p. 7416-7444.
104. Giannini, S., et al., *Transiently delocalized states enhance hole mobility in organic molecular semiconductors*. *Nature Materials*, 2023. **22**(11): p. 1361-1369.
105. J. L. Bre das, J.P.C., D. A. da Silva Filho, and J. Cornil, *Organic semiconductors: A theoretical characterization of the basic parameters governing charge transport*. *Proceedings of the National Academy of Sciences of the United States of America*, 2002. **99**.
106. Mas-Torrent, M. and C. Rovira, *Role of molecular order and solid-state structure in organic field-effect transistors*. *Chemical Reviews*, 2011. **111**(8): p. 4833-56.
107. Ji, L.-F., et al., *Theoretical Study on the Electronic Structures and Charge Transport Properties of a Series of Rubrene Derivatives*. *The Journal of Physical Chemistry C*, 2018. **122**(37): p. 21226-21238.

108. Rivnay, J., et al., *Quantitative determination of organic semiconductor microstructure from the molecular to device scale*. Chemical Reviews, 2012. **112**(10): p. 5488-5519.
109. Ellis, M., et al., *Impact of Nanoscale Morphology on Charge Carrier Delocalization and Mobility in an Organic Semiconductor*. Advanced Materials, 2021. **33**(45): p. e2104852.
110. Palomares, E., L. Billon, and A. Viterisi, *Crystallinity and Molecular Packing of Small Molecules in Bulk-Heterojunction Organic Solar Cells*. Applied Sciences, 2022. **12**(11).
111. Zhang, K., et al., *Relation between Spherulitic Growth, Molecular Organization, and Charge Carrier Transport in Meniscus-Guided Coated Organic Semiconducting Films*. Advanced Electronic Materials, 2021.
112. Hakan Usta, A.F., *Large Area and Flexible Electronics*. Wiley-VCH, 2015.
113. Kwon, S., et al., *Organic Single-Crystal Semiconductor Films on a Millimeter Domain Scale*. Advanced Materials, 2015. **27**(43): p. 6870-6877.
114. Diao, Y., et al., *Morphology control strategies for solution-processed organic semiconductor thin films*. Energy and Environmental Science, 2014. **7**(7): p. 2145-2159.
115. D. Dimitrakopoulos, P.R.L.M.e., *Organic Thin Film Transistors for Large Area Electronics*. Advanced Materials, 2002.
116. Giri, G., et al., *Tuning charge transport in solution-sheared organic semiconductors using lattice strain*. Nature, 2011. **480**(7378): p. 504-508.
117. Li, Y., et al., *Quick Fabrication of Large-area Organic Semiconductor Single Crystal Arrays with a Rapid Annealing Self-Solution-Shearing Method*. Scientific Reports, 2015. **5**: p. 13195.
118. Loo, C.S.K.S.L.E.D.G.J.E.A.Y.-L., *Solvent-dependent electrical characteristics and stability of organic thin-film transistors with drop cast bis(triisopropylsilylethynyl) pentacene* Applied Physics Letters, 2008. **93**.
119. Li, H., et al., *High-mobility field-effect transistors from large-area solution-grown aligned C60 single crystals*. Journal of American Chemical Society, 2012. **134**(5): p. 2760-5.
120. Minari, T., et al., *Controlled self-assembly of organic semiconductors for solution-based fabrication of organic field-effect transistors*. Advanced Materials, 2012. **24**(2): p. 299-306.
121. Minemawari, H., et al., *Inkjet printing of single-crystal films*. Nature, 2011. **475**(7356): p. 364-7.

122. L.E., S., *Physics and Applications of DIP Coating and Spin Coating*. MRS Online Proceedings Library, 1998. **121**: p. 717–729.
123. Hanaor, D.A.H., G. Triani, and C.C. Sorrell, *Morphology and photocatalytic activity of highly oriented mixed phase titanium dioxide thin films*. Surface and Coatings Technology, 2011. **205**(12): p. 3658-3664.
124. Wei Chou, K., et al., *Late stage crystallization and healing during spin-coating enhance carrier transport in small-molecule organic semiconductors*. Journal of Materials Chemistry C, 2014. **2**(28): p. 5681-5689.
125. Yuan, Y., et al., *Ultra-high mobility transparent organic thin film transistors grown by an off-centre spin-coating method*. Nature Communications, 2014. **5**: p. 3005.
126. Zhang, K., et al., *Crystallization Control of Organic Semiconductors during Meniscus-Guided Coating by Blending with Polymer Binder*. Advanced Functional Materials, 2018. **28**(50).
127. Park, B., et al., *Organic thin-film transistors fabricated using a slot-die-coating process and related sensing applications*. RSC Advances, 2016. **6**(103): p. 101613-101621.
128. Zhang, Z., et al., *Marangoni-Effect-Assisted Bar-Coating Method for High-Quality Organic Crystals with Compressive and Tensile Strains*. Advanced Functional Materials, 2017. **27**(37): p. 1-9.
129. Su, Y., et al., *Uniaxial alignment of triisopropylsilylethynyl pentacene via zone-casting technique*. Physical Chemistry Chemical Physics, 2013. **15**(34): p. 14396-404.
130. E., B.A., *Method of coating strip material*, in EASTMAN KODAK CO. 1954: USA.
131. Janneck, R., et al., *Influence of Solute Concentration on Meniscus-Guided Coating of Highly Crystalline Organic Thin Films*. Advanced Materials Interfaces, 2019. **6**(19): p. 1-11.
132. Lee, J.-C., et al., *Meniscus-Guided Control of Supersaturation for the Crystallization of High Quality Metal Organic Framework Thin Films*. Chemistry of Materials, 2019. **31**(18): p. 7377-7385.
133. Zhang, K., et al., *Key role of the meniscus shape in crystallization of organic semiconductors during meniscus-guided coating*. Materials Horizons, 2020. **7**(6): p. 1631-1640.
134. Chen, M., et al., *Understanding the Meniscus-Guided Coating Parameters in Organic Field-Effect-Transistor Fabrications*. Advanced Functional Materials, 2019. **30**(1).

135. Gu, X., et al., *The meniscus-guided deposition of semiconducting polymers*. Nature Communications, 2018. **9**(1).
136. Le Berre, M., Y. Chen, and D. Baigl, *From convective assembly to landau - Levich deposition of multilayered phospholipid films of controlled thickness*. Langmuir, 2009. **25**(5): p. 2554-2557.
137. Lee, J.C., et al., *Numerical Simulations and In Situ Optical Microscopy Connecting Flow Pattern, Crystallization, and Thin-Film Properties for Organic Transistors with Superior Device-to-Device Uniformity*. Advanced Materials, 2020. **32**(48): p. e2004864.
138. Provatas, N.E., K., *Phase-Field Methods in Materials Science and Engineering*. 2010, Wiley.
139. Janneck, R., et al., *Influence of Solute Concentration on Meniscus-Guided Coating of Highly Crystalline Organic Thin Films*. Advanced Materials Interfaces, 2019. **6**(19).
140. Galdi, G.P., *An Introduction to the Mathematical Theory of the Navier-Stokes Equations*. 2011, Springer.
141. Fick, A., V. *On liquid diffusion*. The London, Edinburgh, and Dublin Philosophical Magazine and Journal of Science, 1855. **10**(63): p. 30-39.
142. Michels, J.J., et al., *Predictive modelling of structure formation in semiconductor films produced by meniscus-guided coating*. Nature Materials, 2020.
143. Huang, Y., et al., *Organic Semiconductors at the University of Washington: Advancements in Materials Design and Synthesis and toward Industrial Scale Production*. Advanced Materials, 2019: p. e1904239.
144. Zhang, X., et al., *Precise Patterning of Organic Semiconductor Crystals for Integrated Device Applications*. Small, 2019. **15**(27): p. e1900332.
145. Sirringhaus, H., *25th anniversary article: Organic field-effect transistors: The path beyond amorphous silicon*. Advanced Materials, 2014. **26**(9): p. 1319-1335.
146. Zhang, X., et al., *Alignment and Patterning of Ordered Small-Molecule Organic Semiconductor Micro-/Nanocrystals for Device Applications*. Advanced Materials, 2016. **28**(13): p. 2475-503.
147. Cavallini, M., et al., *Ambipolar multi-stripe organic field-effect transistors*. Advanced Materials, 2011. **23**(43): p. 5091-7.

148. Jo, P.S., et al., *Scalable fabrication of strongly textured organic semiconductor micropatterns by capillary force lithography*. *Advanced Materials*, 2012. **24**(24): p. 3269-74.
149. Bao, R.R., et al., *Self-assembly and hierarchical patterning of aligned organic nanowire arrays by solvent evaporation on substrates with patterned wettability*. *ACS Applied Materials Interfaces*, 2013. **5**(12): p. 5757-62.
150. Giri, G., et al., *High-mobility, aligned crystalline domains of TIPS-pentacene with metastable polymorphs through lateral confinement of crystal growth*. *Advanced Materials*, 2014. **26**(3): p. 487-93.
151. Park, S., et al., *Large-area formation of self-aligned crystalline domains of organic semiconductors on transistor channels using CONNECT*. *Proceedings of the National Academy of Sciences of the United States of America*, 2015. **112**(18): p. 5561-6.

Chapter 2 Optimized charge transport in molecular semiconductors by control of fluid dynamics and crystallization in meniscus-guided coating

2.1 Introduction

Despite the plethora of available strategies for the deposition of functional films by MGC, current understanding on the relation between processing, thin film morphology and electrical behavior does not suffice to either substantiate the claim of scalability, or allow for the definition of an optimal processing window (OPW). For crystallizing OSCs, one generally achieves maximal control at a relatively low casting speed, in the evaporative regime (ER, **Figure 2.1a**), where crystallization occurs relatively close to the contact line[1-3]. In this regime, mass transport and structure formation are largely controlled by solvent evaporation. The height of the deposited film scales with the casting speed as: $h \sim v^{-1}$, since the volumetric deposition rate is constant. In the ER, under optimal processing conditions, the unidirectionality of the casting process is expressed in the crystalline morphology. On the other hand, if casting is too fast, a liquid film entrains before significant evaporation occurs and unidirectional control is lost.[4, 5] In this so-called “Landau-Levich regime” (LLR, **Figure 2.1b**) the entrainment hydrodynamics determines the film thickness, which scales with the casting speed as: $h \sim v^{2/3}$. [6, 7] In terms of the OPW, the LLR in effect sets an absolute upper limit for the casting speed. It has been argued that a principle lower limit is given by the retraction velocity of a meniscus of the pure evaporating solvent,[8, 9] since below this speed an oversupply of solute may lead to crystal nucleation and growth prior to deposition and hence loss of directionality. [10-13]

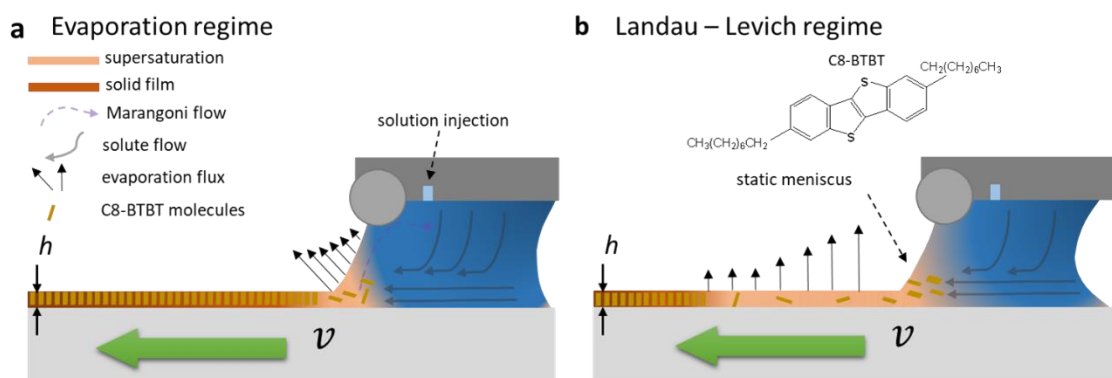


Figure 2.1 Schematic representation of the film deposition in (a) the evaporative and (b) the Landau-Levich regime, including the molecular structure of C8-BTBT.

In this combined experimental and modeling study, we demonstrate how the control parameters casting speed and solution concentration affect the definition of the OPW for FET devices based on zone-cast semiconductor films. For the sake of familiarity, we base our investigation on the benchmark molecular semiconductor 2,7-dioctyl[1]benzothieno[3,2-b][1]benzothiophene (C8-BTBT), but expect the generality of our results to carry over to less familiar and novel systems. With increasing casting speed, we identify three morphological subregimes; I) an isotropic domain-like structure, II) a band-like structure following the coating direction and III) a corrugated morphology lacking directionality. We interpret our experiments using numerical simulations of the steady state fluid dynamics in the bead and the morphology formation in the deposited film, focusing on the onset of the appearance of unidirectionality. The structure formation simulations explain why the bulk solute concentration modulates the onset speed of the aligned subregime, rather than affecting the morphology itself. The second morphological subregime allows for optimized OFET performance. We reveal a direct correlation between the trap density in the OSC film and the casting speed and show how this allows us to achieve an improved saturation and effective charge carrier mobility, with a high reliability factor.

2.2 Results and discussion

2.2.1 C8-BTBT morphology

Where in our previous work we focused on the combined effect of the casting speed and the evaporation rate [14], here we investigate how the speed influences the crystalline morphology of C8-BTBT as a function of the solute concentration. Hereto, zone-casting experiments were performed for v ranging from $40 \mu\text{m s}^{-1}$ to $5000 \mu\text{m s}^{-1}$ for a constant solution concentration of $c_0 = 1 \text{ mg ml}^{-1}$ C8-BTBT (molecular structure in **Figure 2.1b**) in THF. Phenethyl(trichloro)silane (PETS)-modified SiO_2 was used as substrate. It has been argued that an optimum processing temperature T is given for $1 < T_b/T < 1.5$, with T_b the boiling temperature of the solvent ($T_b^{\text{THF}} = 66 \text{ }^\circ\text{C}$). [8] We used $T = 45 \text{ }^\circ\text{C}$, both for substrate and solution, so that $T_b/T = 1.4$. To elucidate the influence of the concentration, experiments were performed at a constant speed of $440 \mu\text{m s}^{-1}$ for $0.25 < c_0 < 8 \text{ mg ml}^{-1}$.

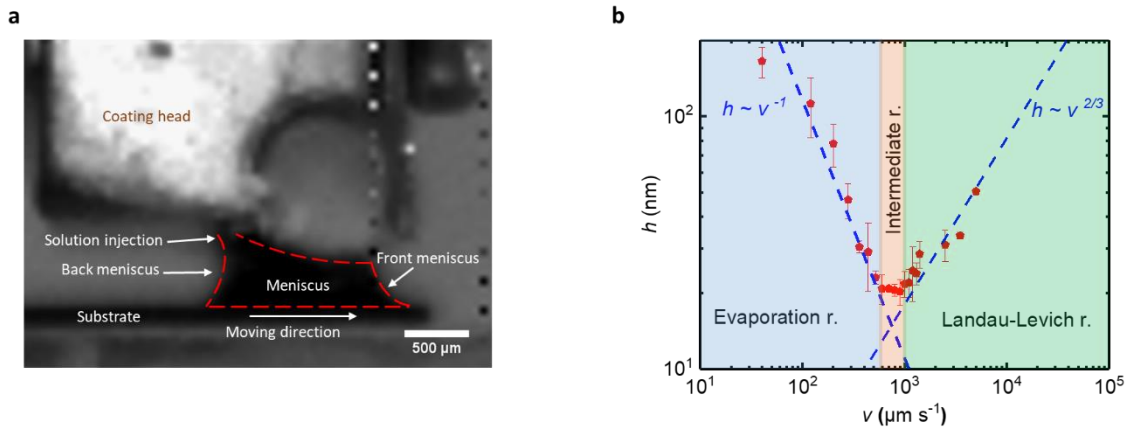


Figure 2.2 a) Real time image of the zone casting setup and coating bead. Dashed – red line shows the meniscus. b) Zone cast C8-BTBT film thickness h plotted as a function of the casting speed v . The red dots in (b) represent the experimental data and the dashed blue lines indicate the theoretical scaling extremes for the evaporative ($h \sim v^{-1}$) and Landau-Levich ($h \sim v^{2/3}$) regimes. [14]

A real-time image of zone casting is shown in **Figure 2.2a**, including the coating head, the substrate and the liquid meniscus. **Figure 2.2b** shows the dry film thickness as a function of speed for $c_0 = 1.0 \text{ mg ml}^{-1}$. The dashed lines, indicating the scaling in the ER and LLR, show that our data complies well with the theoretical prediction. Only at very low speed, *i.e.* $40 \text{ } \mu\text{m s}^{-1}$, the experimental thickness of the entrained film is lower than the prediction. In the intermediate regime (I.R.), the film thickness does not depend on v . The resulting films were studied with POM and AFM to characterize the morphology at different length scales (see **Figures 2.3** and **2.4**). **Figure 2.3** displays films obtained at a constant concentration but varying speed, whereas **Figure 2.4** presents the films cast at different concentration but constant speed.

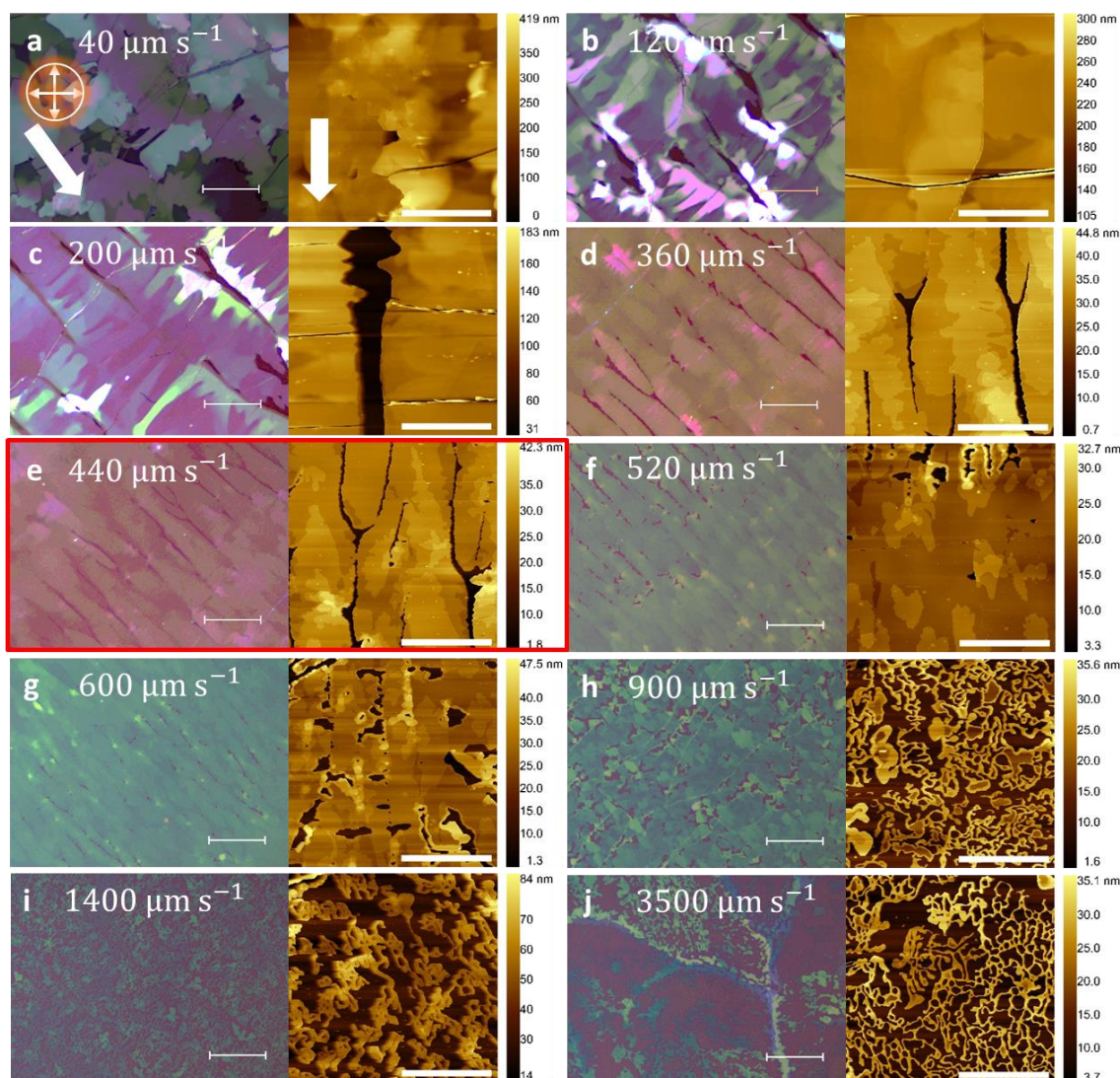


Figure 2.3 Microscopic analysis (left image: POM (reflection mode), right image: AFM) of zone-cast C8-BTBT films obtained for increasing coating speed (indicated in the panels) at a solute concentration of 1.0 mg ml^{-1} . The scale bars in the POM and AFM images represent $50 \text{ }\mu\text{m}$ and $20 \text{ }\mu\text{m}$, respectively. The white arrows in (a) and (b) indicate the coating direction. Changes in the film obtained for $v = 440 \text{ }\mu\text{m s}^{-1}$ (marked by the red box) as a function of the solute concentration, are presented in **Figure 2.4**.

Irrespective of the concentration, three types of morphologies are observed with the increasing coating speed: I) an isotropic domain-like morphology (**Figures 2.3a,b** and **2.4e,f**),

II) a “woven” pattern of near-unidirectional crystalline stripes (**Figure 2.3c-g** and **2.3a-d**), and III) a corrugated dendritic structure (**Figures 2.3h-j**). Only morphology II bears a structural directionality matching the coating direction. From an application point of view, morphology II is intuitively compatible with unidirectional in-plane charge transport. The loss in directionality by *increasing* the coating speed, *i.e.* the transition II \rightarrow III, is expected based on the transition from the I.R. to the LLR. In contrast, the loss of directionality by *lowering* the speed, *i.e.* the transition II \rightarrow I, is somewhat less intuitive but has been observed previously [1, 15, 16] and ascribed to nucleation and growth occurring in the coating bead, prior to entrainment of the dry film.[1, 17]

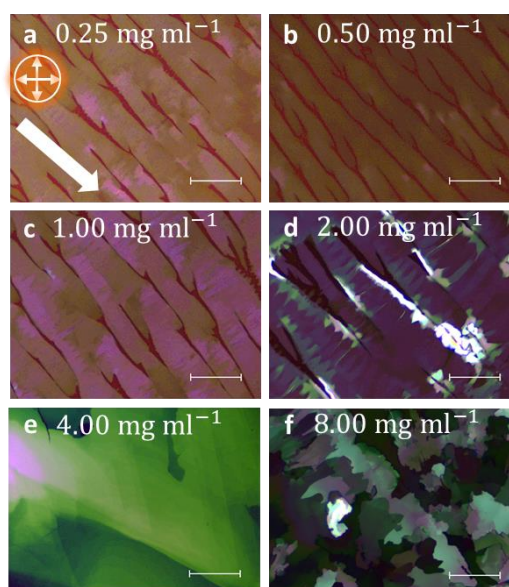


Figure 2.4. POM images of zone-cast C8-BTBT films obtained at different solute concentrations. All depositions were performed at a constant casting speed $v = 440 \mu\text{m s}^{-1}$. The white arrows indicate the casting direction. The scale bars are $50 \mu\text{m}$.

It is interesting to note that a change in the solute concentration does not seem to affect the morphology itself, but merely the velocities at which the morphological transitions occur.

This becomes apparent when comparing **Figures 2.3a, b** and **c** with **Figures 2.4f, e** and **d**: the $I \leftrightarrow II$ transition occurs at a higher speed if the solute concentration is increased. Since such a shift directly affects the eventual processing window, we studied the possible cause of the $I \leftrightarrow II$ transition in more detail. Janneck *et al.* hypothesized that morphology I results from nucleation in the bead, once the casting speed becomes lower than the retraction velocity of the pure solvent meniscus.[1, 15] They reasoned that at such low speeds an oversupply of the solute occurs, as the substrate translation is too slow to absorb sufficient material.[15] Upon exceeding supersaturation, random nucleation occurs, giving a non-directional domain structure.

2.2.2 Numerical analysis in coating bead and crystallization

Although a rise in concentration in the bead at low v serves as an explanation for the appearance of morphology I, ascribing its occurrence to a reduced solute absorption by the substrate is unsatisfactory. First, the substrate does not necessarily “absorb” the solute. Instead, the solute rather precipitates or nucleates directly on it. Second, since the outflux of solute is small compared to the evaporative flux, a change in its magnitude is not expected to significantly impact the concentration in the bead. Third, the relation $h \sim v^{-1}$ implies that in the ER the solute outflux is independent of the casting speed. To verify the third point, we perform 2D isothermal Navier-Stokes (NS) and mass transport simulations in the low speed regime[3, 9, 18]. The shape of the simulation box (**Figure 2.5a**) has been physically predetermined and fixed to match the shape of the actual coating bead (**Figure 2.2a**). Different from previous simulations [3, 9], we cut a small region (see inset **Figure 2.5a**) at the tip of the front meniscus to explicitly allow for the solution to exit the simulation domain (outlet region) upon entrainment.[18-20]

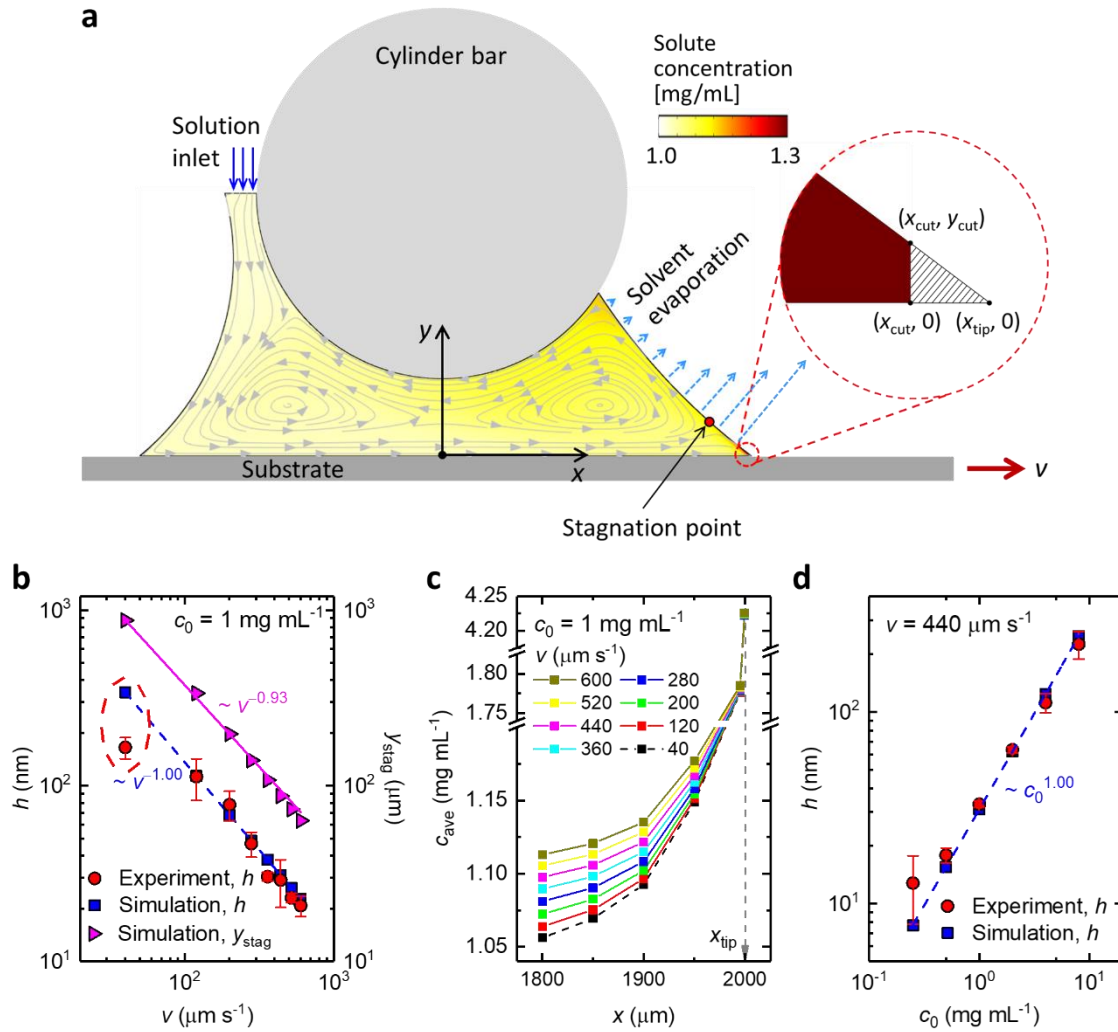


Figure 2.5 Finite element simulations of the flow and concentration fields in the meniscus during zone-casting of C8-BTBT. *a*) Illustration of the simulation domain, boundary conditions, and coordinate systems. The shown flow and concentration fields correspond to $y_{gap} = 500 \mu\text{m}$, $c_0 = 1 \text{ mg mL}^{-1}$, and $v = 440 \mu\text{m s}^{-1}$. *b*) Film thickness h and the y coordinate of the stagnation point as a function of the substrate speed. The red dashed ellipse shows the discrepancy between the calculation and the experiment at low speed. *c*) Average solute concentration c_{ave} (averaged in the y direction) near the outlet region (inset of **Figure 2.5a**) as a function of x . *d*) Film thickness as a function of the inlet solute concentration.

Figure 2.5a shows that two vortices appear, resulting from entrainment and backflow of the solution.[9] The vertical coordinate of the stagnation point at the front meniscus decreases as $y_{\text{stag}} \sim v^{-0.93}$ (**Figure 2.5b**), *i.e.* close to the speed-dependence of the simulated film thickness, which agrees excellently with the experimental one for $v > 100 \mu\text{m s}^{-1}$. Indeed, since in the ER the material deposition rate is speed-independent, the relation $h \sim v^{-1}$ can be derived simply by equating the outgoing fluxes of solvent and solute due to evaporation and deposition to the influx of the native solution.[21, 22] As a consequence, as long as the ER scaling applies, the concentration far away from the tip remains virtually independent of the casting speed and close to c_0 [21], as indeed shown by **Figures 2.5c**. Only in the region near the tip the solute concentration rises drastically due to the diverging evaporation rate,[23] which is independent of v . The linear scaling of the deposited film thickness with the solute concentration $h \sim c_0$ (see **Figure 2.5d**) is consistent with the same mass conservation argument.

For $v < 100 \mu\text{m s}^{-1}$, *i.e.* roughly where the II \rightarrow I morphology transition occurs for $c_0 = 1.0 \text{ mg ml}^{-1}$, the simulation overestimates the thickness in comparison to the experimental value (red ellipse in **Figure 2.5b**). Such a deviation at very low speed has, for instance, also been observed for MGC of metal-organic frameworks[24] and phospholipids 30a[21]. At the same time, a rise in the simulated concentration in the bead remains absent. This suggests that fixed-domain/fixed meniscus fluid dynamics simulations, such as the present one and used before[15], become inadequate at low v . A possible reason is that a constant volume is trivially not part of the steady state prerequisite. Although a fixed fluid domain is convenient and valid at an intermediate casting speed sufficiently far away from the LLR, we suspect that it breaks down if v approaches the retraction velocity of the fluid meniscus. Accurate simulation in this regime ideally requires a free liquid / air interface, together with an explicit description of the

coexisting phases. However, this makes the calculation highly non-trivial and outside the scope of this study.

Instead, we define a simplified analytical model that captures some essential features of the coating process in an approximate way. We write the mass balances of solute and solvent across the front section of the bead (**Figure 2.6a**) as a function of an entrainment flux J_{in} , a reverse flux J_r , an evaporative flux J_{ev} and a deposition rate J_L (all in $\text{m}^3 \text{s}^{-1}$):

$$\bar{\phi} \frac{dV}{dt} + V \frac{d\bar{\phi}}{dt} = J_{\text{in}}\phi_{\text{in}} - J_r\bar{\phi} - J_L\phi_L \quad (1)$$

$$(1 - \bar{\phi}) \frac{dV}{dt} - V \frac{d\bar{\phi}}{dt} = -J_{\text{ev}}(\bar{\phi}) + J_{\text{in}}(1 - \phi_{\text{in}}) - J_r(1 - \bar{\phi}) - J_L(1 - \phi_L) \quad (2)$$

, with $\bar{\phi}$ the mean volume fraction, V the volume of the domain, $\phi_{\text{in}} < \bar{\phi}$ the ingoing concentration and $\phi_L > \bar{\phi}$ the concentration in the deposited film. We neglect a dependence of ϕ_{in} on the casting speed. More importantly, we couple the evaporative flux to the mean bead concentration according to: $J_{\text{ev}}(\bar{\phi}) \approx k_s A(1 - \bar{\phi})$, *i.e.* assuming ideal solution conditions. A is the (effective) cross section area of the bead and k_s the retraction velocity of the pure solvent. We furthermore assume a linear relation between J_{in} and v . The deposition rate J_L is constant in the ER and may be estimated from the experiment. The height of the dry deposited film is: $h = \phi_L J_L / v$.

Solving Equations (1)-(2) for the steady state condition $\frac{dV}{dt} = \frac{d\bar{\phi}}{dt} = 0$ and eliminating J_r as dependent variable, we arrive at an expression for the mean volume fraction:

$$\bar{\phi} = \frac{k_S A - J_{in} + J_L + \sqrt{(k_S A - J_{in} + J_L)^2 - 4k_S A (J_L \phi_L - J_{in} \phi_{in})}}{2k_S A} \quad (3)$$

Next, we define a characteristic casting speed $v^* = 2k_S/G$, for which the entrainment flux equals the evaporative flux of the pure solvent: $J_{in}^* = k_S A$. The prefactor G is a geometric constant. Substitution gives:

$$\bar{\phi}^* = \frac{J_L + \sqrt{J_L^2 + 4k_S^2 A^2 \phi_0 - 4k_S A J_L \phi_L}}{2k_S A} \quad (4)$$

Since the height of the deposited film is much smaller than the height of the bead, J_L can be ignored, demonstrating the insignificance of solute deposition in determining $\bar{\phi}$. Doing so, we obtain $\bar{\phi}^* \approx \sqrt{\phi_{in}}$.

Figure 2.6b plots the various fluxes and the mean concentration as a function of the normalized casting speed. Although, due its simplifications, we do not expect the model to produce the exact functional dependence of the fluxes, the trend is consistent with the experimental observations. For $v/v^* > 1$ (high speed), the mean concentration remains close to c_{in} , which is in agreement with the numerical simulations. At the same time, the evaporative flux J_{ev} reaches a near constant value. For $v/v^* < 1$ (low speed) the concentration indeed rises, though not due to a reduced solute absorption by the substrate but rather a decrease in J_r and a longer retention of the solution in the considered volume. The rise in concentration suppresses the solvent activity and hence J_{ev} . This reduction principally prevents (significant) retraction of the meniscus, but the fact that in the experiment the film thickness for $v = 40 \mu\text{m s}^{-1}$ is

consistently lower than expected (see **Figure 2.5b** and note the error bar), testifies a slow retraction, resulting in an effectively higher substrate speed and hence a lower h . Finally, the increase of the transition speed for morphology I \rightarrow II with c_0 may be explained by a substantial rise in concentration away from the meniscus, as earlier simulations[15] have demonstrated.

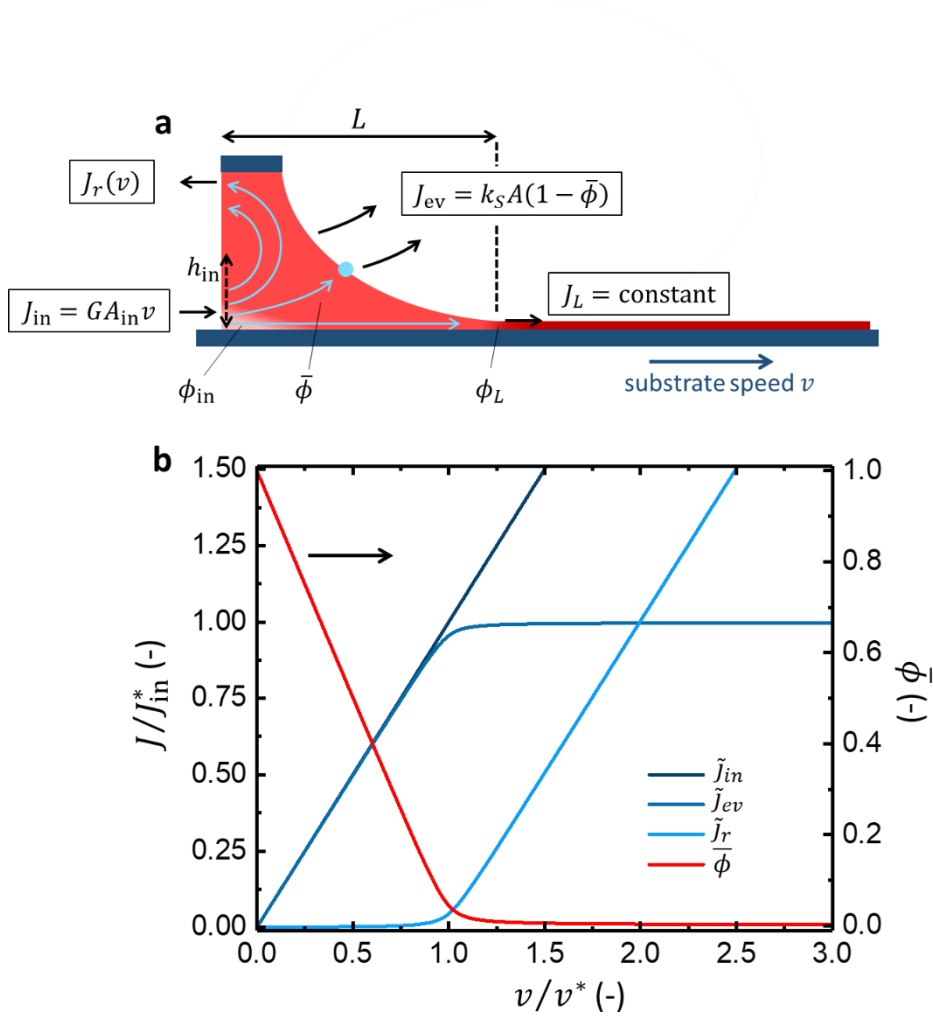


Figure 2.6 a) Schematic representation of the front part of the coating bead, as assumed by the analytical model for the ER. b) Dimensionless fluxes and mean bead concentration calculated as a function of dimensionless substrate speed, for $c_{in} = 2 \text{ mg ml}^{-1}$ ($\phi_{in} = 0.002$). Tildes in the legend denote dimensionless quantities.

We find further support for a significantly elevated concentration in the bead at low v using our recently proposed MGC model.[14] We recall that this model captures the effect of the speed dependence of the concentration gradient in the tip by interpolating an initial concentration between a high extreme ϕ_{ev} at a low speed and the native concentration ϕ_0 at infinite speed. While in our previous study we fixed ϕ_{ev} below supersaturation, we now consider ϕ_{ev} exceeding it and vary ϕ_0 as in the experiment. Since we only aim for a trend-based comparison, we use a dimensionless speed [14] and refrain from matching ϕ_0 with the experimental concentrations. **Figure 2.7** shows that the trend predicted by the model agrees very well with the experiments: a transition from an aligned to a domain-like structure occurs upon lowering the speed. Furthermore, the transition shifts to higher v upon increasing ϕ_0 .

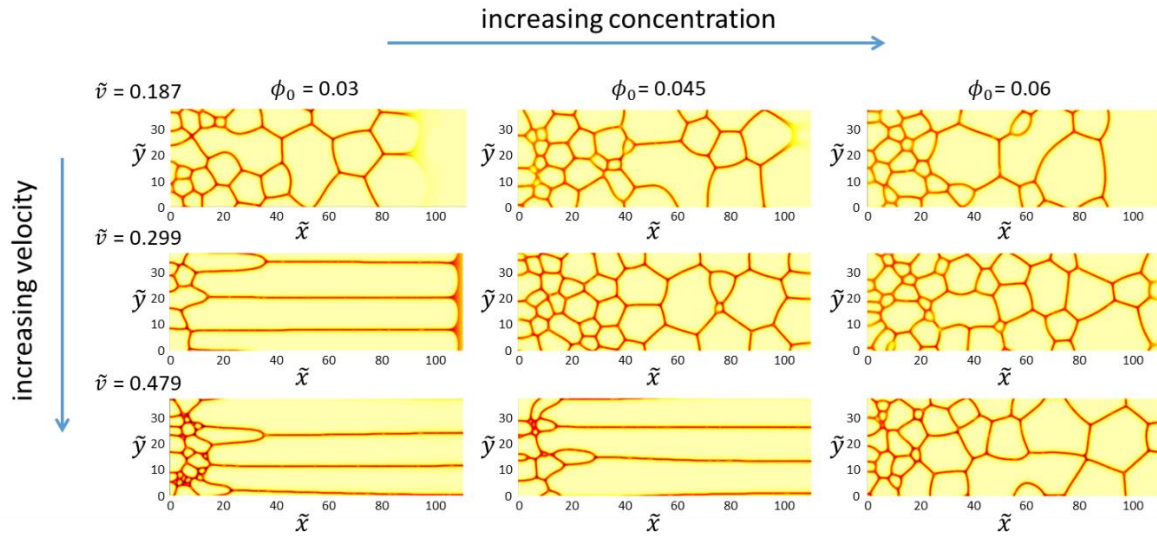


Figure 2.7 Numerically simulated coated morphologies (crystallinity order parameter, see Ref.[14]), plotted as a function of dimensionless space (\tilde{x}, \tilde{y}) for varying native solute volume fraction (ϕ_0) and dimensionless coating velocity \tilde{v} . For the non-dimensionalization of time and space in these calculations, we refer to ref.[14].

The speed marking the transition to morphology II is just high enough to prevent supersaturation in the bead, resulting in unidirectional growth parallel to the casting direction (**Figures 2.3c-g**).^[14] Indeed, close inspection in **Figure 2.8** reveals a terrace-like structure with a step height of 2.9 nm, exactly matching the lattice spacing. The unidirectional crystal growth and the low RMS roughness makes morphology II a suitable candidate for implementation in OFET devices. Morphology II is mostly dense owing to mutual impingement, but also exhibits voids and hence a decreased surface film coverage (**Figure 2.9a**). Such voids in MGC films of C8-BTBT have been shown to occur periodically or continuously, depending on the casting speed.^[1, 3] A periodicity either reflects a subregime where fluctuating concentration-driven surface tension gradients give rise to long wavelength height undulations^[25] or a stick-slip mechanism due to pinning and depinning of the contact line at the deposit.^[26] **Figure 2.9a** shows that the RMS roughness of the crystal domains of morphology II decreases with casting speed, with the smoothest films obtained for $v \approx 600 \mu\text{m s}^{-1}$. At the speed range of morphology II, the roughness is in the range of 3.0 - 6.5 nm, matching the spacing corresponding to one to two interlayers in the C8-BTBT crystal lattice.^[27, 28]

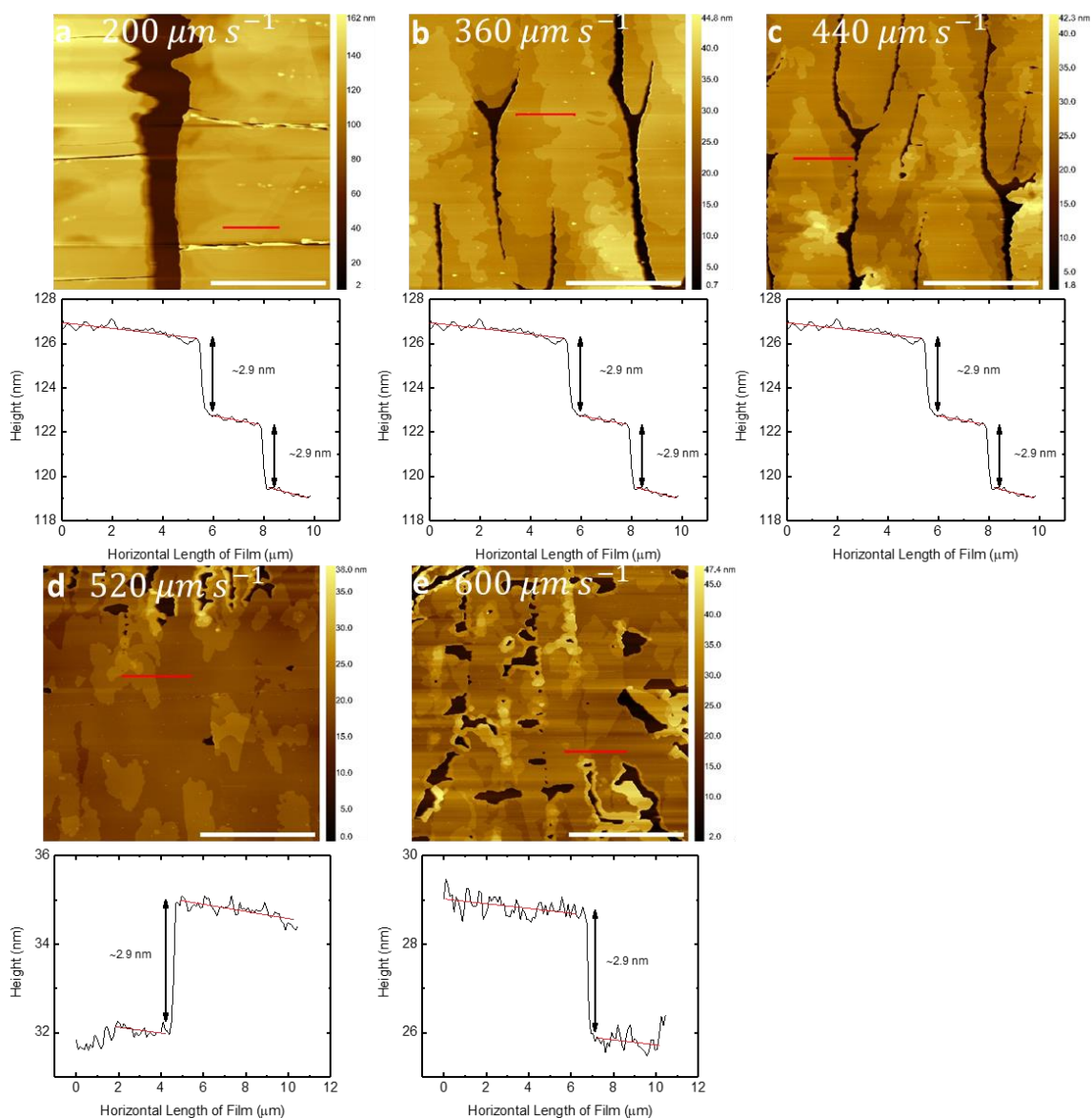


Figure 2.8 AFM images and corresponding height profiles of zone-cast C8-BTBT films obtained at different v . In the range of 200 to 600 $\mu\text{m s}^{-1}$, the terrace – like morphology is obtained. The step height corresponds well to an interlayer distance of 2.9 nm of C8-BTBT. All scale bars are 20 μm .

Figure 2.9b reveals a near linear decrease in the mean width \bar{w} of the stretched domains with increasing coating velocity. A possible cause for the decrease in \bar{w} with increasing

substrate velocity (**Figures 2.3b-g**) is a decrease in the time available for Ostwald ripening. During this process large (sub)domains grow at the expense of small ones on account of a concentration gradient arising from a difference in curvature. Since during ripening the mean domain size increases with time as $\sim t^{1/3}$, the ER should yield an approximate dependence of $\bar{w} \sim v^{-1/3}$. However, the fact that the speed dependence of \bar{w} is steeper (**Figure 2.9b**) indicates the presence of a contributing mechanism. To understand this, we note that small domains principally testify a high nucleation density, providing an “early stage argument” based on the notion that a continuous solvent quench occurs in the foot of the meniscus where the viscous forces roughly balance the surface tension. As in the ER the height of the film entrained from the gradient in the tip of the meniscus decreases with increasing speed, an increase in the latter results in a deeper quench and hence an increased nucleation density.[14]

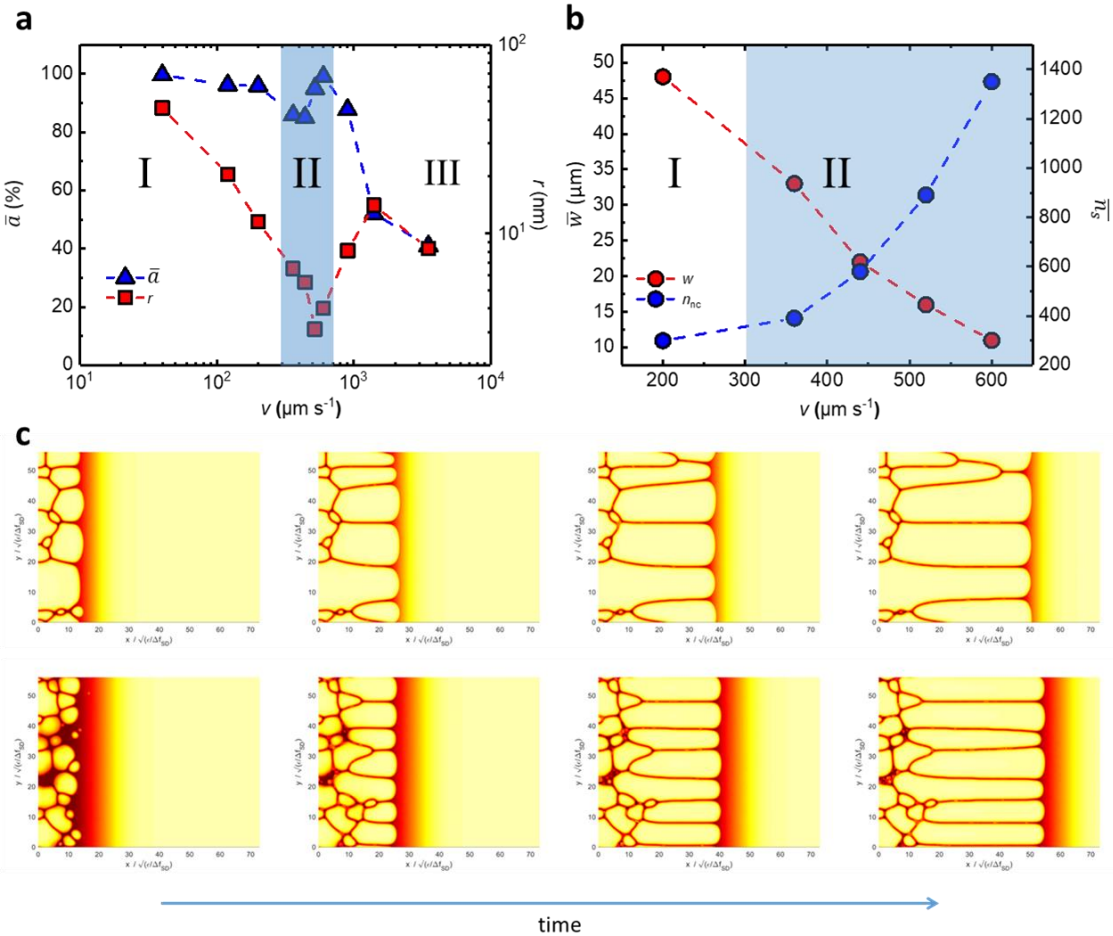


Figure 2.9 Quantitative analysis of the films displayed in **Figure 2.3**. a) Film coverage (\bar{a}) and RMS roughness (r) of the C8-BTBT films plotted as a function of casting speed v . The morphological subregimes are indicated with roman numbers. b) Mean crystal domain width (\bar{w}) and mean number of stripes (\bar{n}_s) encountered in morphology II perpendicular to the coating direction. \bar{n}_s has been obtained using the relation: $\bar{n}_s = \bar{w}\bar{a}/W$, with W the width of the meniscus. Dashed-lines in (a) and (b) are eye guides. c) Numerical simulation of aligned crystallization (morphology II) during MGC. Substrate translation occurs from right to left. The images show the crystallinity, as well as the normalized height (see ref. [14] for details) as a function of dimensionless space (\tilde{x}, \tilde{y}) for two different dimensionless casting speeds (see figure) and $\phi_0 = 0.03$. For the non – dimensionalization of time and space in these calculations, we refer to ref. [14].

We demonstrate this by numerical simulation (**Figure 2.9c**) of a section of the film in which evaporation induces the formation of new nuclei on the left side of the domain during slow (top panels) and faster coating (bottom panels). Successful nucleation is clearly more frequent if substrate translation is fast, resulting in narrower domains as also experimentally observed. For $c_0 = 1.0 \text{ mg ml}^{-1}$, this form of nucleation and growth persists up to $\sim 600 \text{ } \mu\text{m s}^{-1}$. Beyond this speed, a second morphological transition occurs (II \rightarrow III) towards a corrugated structure, characterized by dendritic features, wherein the unidirectionality is lost for reasons explained above. The film coverage decreases abruptly, whereas the roughness follows the opposite trend (**Figure 2.9a**). This dendritic, rather than spherulitic structure of C8-BTBT has previously been observed for dip-coating at a high pulling speed.[18]

2.2.3 Molecular organization

To gain further structural information on the deposited C8-BTBT thin films including the π - π stacking and interlayer distances, long-range crystalline order, grain size and molecule's orientation relative to the substrate, grazing incidence wide-angle X-ray scattering (GIWAXS) was employed. It is generally believed that any variation in the molecular arrangement concerning unit cell dimension[29], long range order and “edge-on” or “face-on” packing motif significantly influence on the charge carrier transport. The analysis of the GIWAXS data is presented in **Figure 2.11**. **Figure 2.11a** presents 1-dimensional out-of-plane integration profiles of GIWAXS patterns in **Figure 2.10** obtained for zone-cast C8-BTBT at varying speed. The interlayer distance of 2.91 nm for all samples is determined from the main reflection observed at $q_z = 0.216 \text{ \AA}^{-1}$ and $q_{xy} = 0 \text{ \AA}^{-1}$ (**Figure 2.11a**) Higher order reflections (up to 3rd) imply long-range organization of the molecules in the out-of-plane direction of the film. This interlayer distance is in agreement with the length of a molecule, as presented in the literature [30] and suggests that the long axis of the C8-BTBT molecule is arranged perpendicular to the substrate surface.

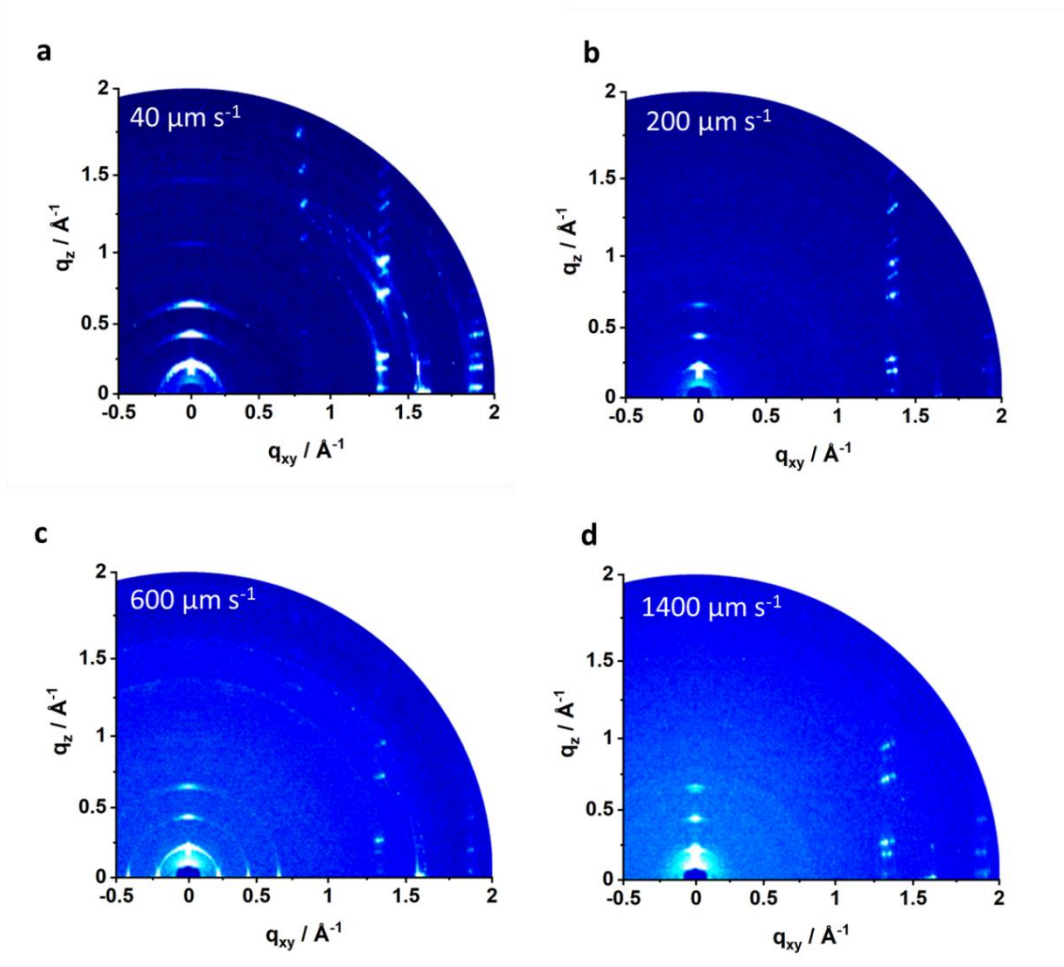


Figure 2.10 GIWAXS patterns of zone-cast C8-BTBT films obtained at (a) $40 \mu\text{m s}^{-1}$, (b) $200 \mu\text{m s}^{-1}$, (c) $600 \mu\text{m s}^{-1}$, and (d) $1400 \mu\text{m s}^{-1}$. The measurements were done in parallel to the casting direction.

In this edge-on organization, π -stacking direction is arranged parallel to the surface which is beneficial for in-plane charge transport. The crystal lattice of the molecules in thin films is in agreement with single crystal data.[12, 13] Detailed analysis of the reflection assigned to the interlayer distance shows that for $40 \mu\text{m s}^{-1}$ substrate speed an additional a 001* reflection appears at $q_z = 0.210 \text{ \AA}^{-1}$, corresponding to a d-spacing of 2.71 nm (**Figure 2.11a**). This is due to a different molecular tilting on the substrate induced by the PETS self-assembled

monolayer (SAM), as well as the vertical temperature gradient across the film. A longer crystallization time and interactions between the alkyl side chains can enhance molecular packing of C8-BTBT molecules in the out-of-plane direction.[31] Comparable results, *i.e.* a decrease in the interlayer distance, has been observed for C8-BTBT blended with poly(4-styrene sulfonic acid) (PSS).[30]

The role of the substrate speed on the molecular order (tilting angle) can be firstly observed by variation in the orientation and domain size in the out-of-plane direction. As evident from **Figure 2.11b**, the coherence length C_{L001} , calculated on the basis of FWHM value of the 001 peak, increases with higher v in the ER. The highest C_{L001} is observed for $600 \mu\text{m s}^{-1}$ which corresponds to a h of 20 nm, suggesting a homogenous molecular organization throughout the height of the layer. The lower C_{L001} values at lower speeds in the ER and in the entire LLR (morphologies I and III indicated in **Figure 2.11b**) suggest a higher disorder of the C8-BTBT molecules. This is confirmed by the domain misalignment presented by the angular intensity distribution of the 001 reflection in the GIWAXS patterns. For samples deposited at $v < 360 \mu\text{m s}^{-1}$ (morphology I) and $v > 900 \mu\text{m s}^{-1}$ (morphology III) the FWHM is found equal to 9.5° . An almost twice lower value is observed for the speed range of $360 \mu\text{m s}^{-1} < v < 900 \mu\text{m s}^{-1}$, confirming the highest degree of molecular order of the thin film cast at $600 \mu\text{m s}^{-1}$.

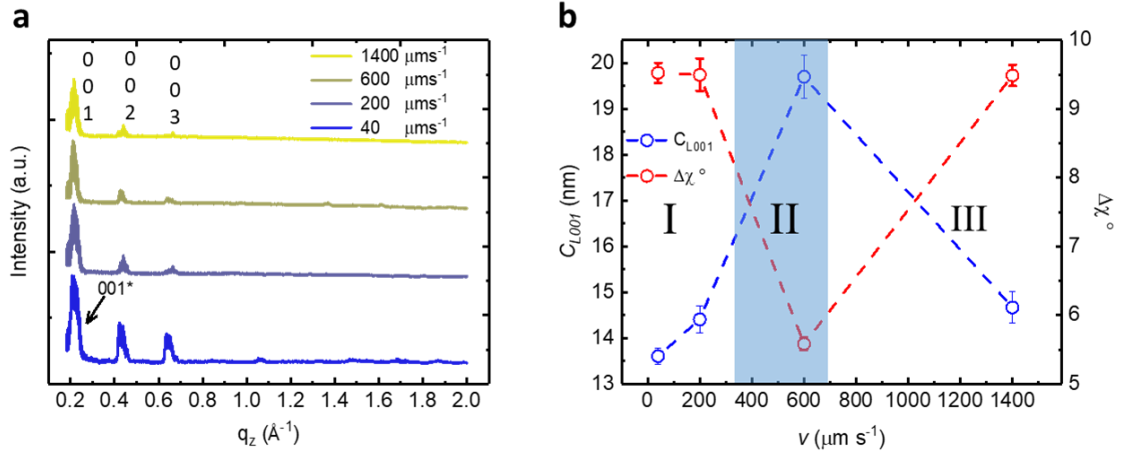


Figure 2.11 a) Out-of-plane profiles of GIWAXS patterns for C8-BTBT films zone-cast at different coating speeds. b) Coherence length of the 001 reflection in interlayer direction and $\Delta\chi$ as a function of casting speed. The three morphological regimes are indicated in the graph. Dashed lines are eye guides.

Finally, we consider the influence of the casting speed on the π -stacking distance (020 reflection). For a relatively low casting speed of 200 $\mu\text{m s}^{-1}$, at which the shearing forces induce unidirectional molecular ordering, the π -stacking distance is 3.35 \AA . By applying a higher casting speed of 600 $\mu\text{m s}^{-1}$, the π -stacking distance is reduced to 3.25 \AA . This is probably connected with a compressively strained molecular lattice of the C8-BTBT, previously proven for solution sheared TIPS-pentacene[29] and C8-BTBT:PSS blend[30]. For the casting speeds of 40 $\mu\text{m s}^{-1}$ and 1400 $\mu\text{m s}^{-1}$, we observed two peaks which can be assigned to π -stacking distance of 3.25 \AA and 3.33 \AA . Due to the low intensity of π -stacking reflection (020), we were not able to determine the in – plane coherence length.

2.2.4 OFETs

The charge carrier transport in the zone-cast films is investigated in field-effect transistors with a bottom – gate, top – contact (BGTC) configuration. A MoO₃ / Ag bilayer was used as top contact to reduce the charge injection barrier between the work function of the metal and the HOMO level of the semiconductor.[32, 33] The analyzes were done over 15 devices for each case.

The isotropic domain-like morphology I (obtained for $v = 40 \mu\text{m s}^{-1}$) leads to poor charge carrier transport, as evidenced by a low saturation mobility μ_{sat} of $\sim 10^{-3} \text{ cm}^2 \text{ V}^{-1} \text{ s}^{-1}$, both parallel (\parallel) and perpendicular (\perp) to the casting direction (**Figure 2.12a**). Such a low charge carrier mobility is explained by a high density of grain boundaries, as confirmed by the AFM images presented in **Figure 2.3a,b**. This type of morphology results in the highest average threshold voltage of $V_{th} = -10 \pm 2 \text{ V}$ (**Figure 2.12b**). The polycrystalline domains are stretched for $v = 120 \mu\text{m s}^{-1}$ that induces a one order of magnitude increase in the charge carrier mobility to $\sim 10^{-2} \text{ cm}^2 \text{ V}^{-1} \text{ s}^{-1}$. The value remains still low due to the formation of morphology I. A significant mobility increase by two orders of magnitude to $\mu_{sat,\parallel} = 0.30 \text{ cm}^2 \text{ V}^{-1} \text{ s}^{-1}$ is observed at the morphology I \rightarrow II transition for $v = 200 \mu\text{m s}^{-1}$ (**Figure 2.12a**). **Figure 2.12b** shows that at the I \rightarrow II transition the overall device performance improves with a threshold voltage decreasing by a factor of three and the I_{on}/I_{off} ratio increasing by two orders of magnitude. The morphology I \rightarrow II transition provides an improved electrical performance not only due to the lower density of the grain boundaries but also due to the change in the contact resistance R_{con} at the electrode/semiconductor interface and the bulk resistance R_{bul} in the semiconductor. The resistance profile of the BGTC device configuration is shown in **Figure 2.13a**. We calculated $R_{con} + R_{bul}$ by using transfer – length method (TLM)[34] for $v = 200 \mu\text{m s}^{-1}$ (**Figure 2.13b**) and $520 \mu\text{m s}^{-1}$ (**Figure 2.13c**). The $R_{con} + R_{bul}$ was found $1.10 \times 10^5 \Omega \text{ cm}$ for $200 \mu\text{m}$

s^{-1} and $0.10 \times 10^5 \Omega \text{ cm}$ for $520 \mu\text{m s}^{-1}$. The calculated difference originates from the film thickness where thicker film increases R_{bul} .

For $v > 900 \mu\text{m s}^{-1}$, with the drop of the molecular alignment at the morphological transition II \rightarrow III, the charge carrier mobility decreases to $\mu_{sat,\parallel} = 0.30$ and $\mu_{sat,\perp} = 0.18 \text{ cm}^2 \text{ V}^{-1} \text{ s}^{-1}$. A more drastic decrease in the charge carrier mobility down to the order $\sim 10^{-2} \text{ cm}^2 \text{ V}^{-1} \text{ s}^{-1}$ is seen for higher coating speeds of $1400 \mu\text{m s}^{-1}$ and $3500 \mu\text{m s}^{-1}$ which is attributable to the higher disorder, as evidenced by a low coherence length and misalignment of molecules (**Figure 2.11b**). The threshold voltage and I_{on}/I_{off} ratio for morphology III are comparable to those of morphology I (**Figure 2.12b**), showing that the speed range associated with morphology II provides the optimal processing window for the charge carrier transport in OFETs. Since the film coverage is variable in respect to casting speed (**Figure 2.9a**), we calculated true $\mu_{sat,\parallel}$ by multiplying the film coverage with the channel width. However, the obtained trend remained the same as it was shown in **Figure 2.12a**.

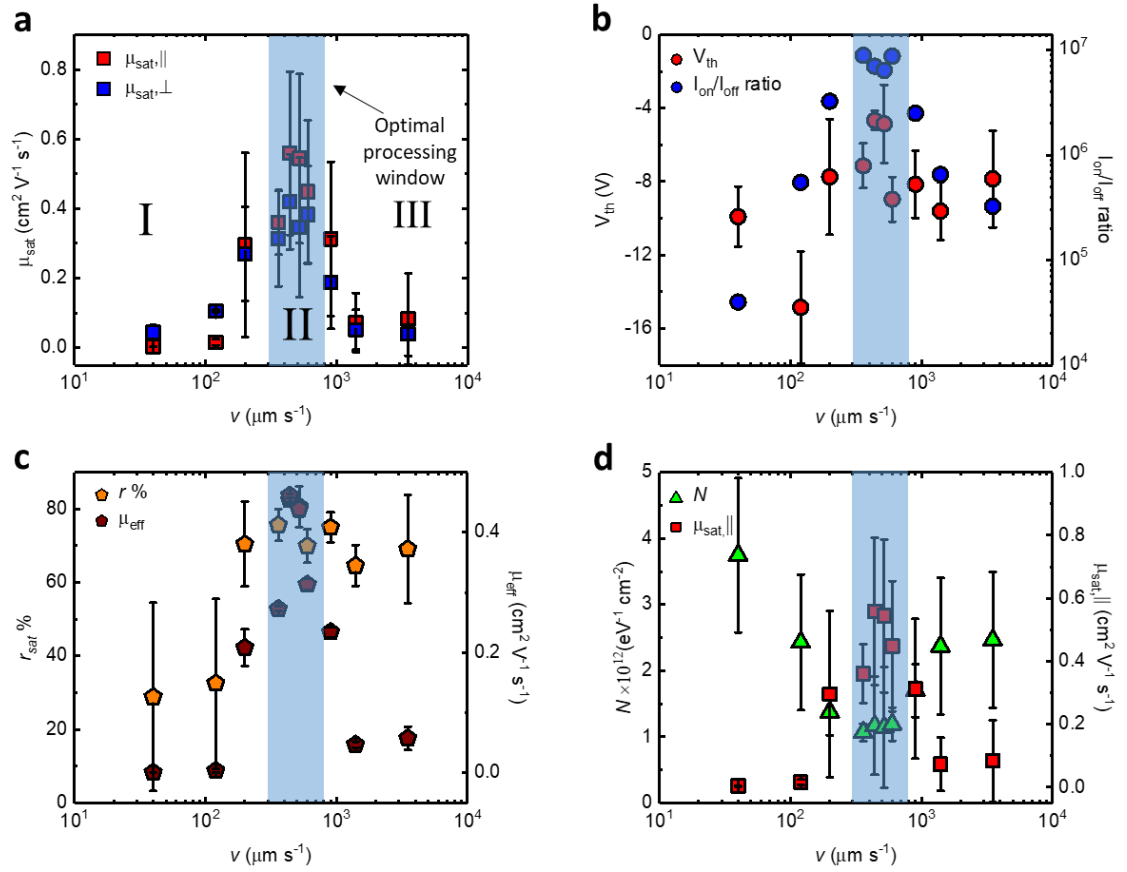


Figure 2.12 OFET performance as a function of v with a) saturation charge carrier mobility μ_{sat} , b) threshold voltage V_{th} and I_{on}/I_{off} ratio, c) reliability factor r_{sat} and effective mobility μ_{eff} and d) trap density N and μ_{eff} . Morphology regimes I, II and III are indicated in the graph (a) together with the optimal processing window.

C8-BTBT does not exhibit any charge carrier transport anisotropy due to its molecular arrangement in the crystal lattice.[35] We ascribe the difference between the values measured parallel and perpendicular to the casting direction to the voids in the film, as well as the reduction in the crystal width, as shown in **Figure 2.9b**. In **Figure 2.12a**, this speed range of morphology II also showed the highest average charge carrier mobility of $0.36 \leq \mu_{sat,||} \leq 0.56 \text{ cm}^2 \text{ V}^{-1} \text{ s}^{-1}$ and $0.31 \leq \mu_{sat,\perp} \leq 0.42 \text{ cm}^2 \text{ V}^{-1} \text{ s}^{-1}$. The crystalline stripes in morphology II likely

exhibit long-range molecular order, which explains its favorability for in-plane charge carrier transport. Admittedly, μ_{sat} is found relatively moderate for the zone-cast C8-BTBT films in comparison to previously published reports.[1, 36] On the other hand, the devices morphology II with show a high reliability factor (r_{sat}) of $\geq 65\%$ and effective mobility (μ_{eff}) (**Figure 2.12c**). A more detailed explanation is given in ref.[37]

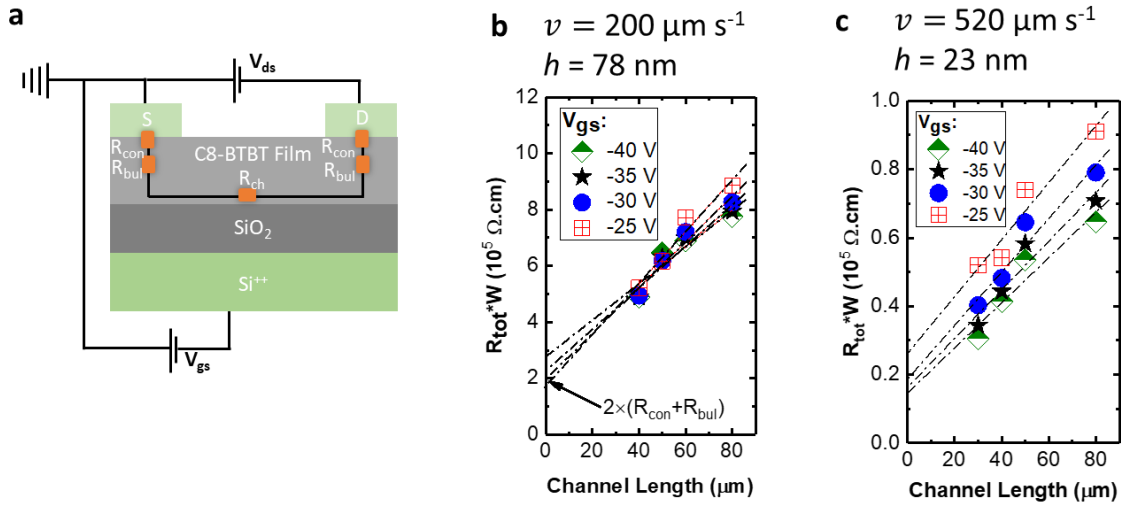


Figure 2.13 (a) The resistance profile of bottom-gate top-contact (BGTC) device configuration. Transfer – length method (TLM) was applied for (b) $v = 200 \mu m s^{-1}$ and (c) $v = 520 \mu m s^{-1}$. $R_{con} + R_{bul}$ is at channel length = 0 as it is shown in (b).

We establish an additional link between charge carrier transport and morphology by calculating the density of interfacial and bulk deep traps using the subthreshold swing SS , defined as[38]:

$$SS = \frac{k_B T \ln 10}{q} \left[1 + \frac{q^2}{C_i} N \right] \quad (5)$$

, with k_B the Boltzmann constant, T the absolute temperature, q the elementary charge, N the trap density and C_i the insulator capacitance. As shown in **Figure 2.12d**, N gradually decreases in the ER and levels off at a minimum plateau in the optimal processing window (OPW) of $\sim 1 \times 10^{12} \text{ eV}^{-1} \text{ cm}^{-2}$ for the speed range of $360 \leq v \leq 600 \text{ } \mu\text{m s}^{-1}$, *i.e.* for morphology II. As expected, N increases again to $\sim 2.5 \times 10^{12} \text{ eV}^{-1} \text{ cm}^{-2}$ between 600 and $3500 \text{ } \mu\text{m s}^{-1}$, *i.e.* for morphology III. Similarly, trap density of single – crystal pentacene was found equal to $1 \times 10^{12} \text{ eV}^{-1} \text{ cm}^{-2}$. [38] The defined window is consistent with the morphology analyses in which morphology II ($360 \text{ } \mu\text{m s}^{-1} \leq v \leq 600 \text{ } \mu\text{m s}^{-1}$) represents the OPW. In summary, r_{sat} reaches the highest values for morphology II due to linear $I_{ds}^{1/2}$ (ideal) transfer curves, V_{th} closer to 0 V as well as reduced value of N . For this reason, we do not only evaluate μ_{sat} but also r_{sat} and N to understand the non-ideality of transfer curves. We agree with the procedure proposed in literature in ref. [39] which r_{sat} and μ_{eff} should be compared in order to understand and compare non-ideal / ideal behavior of organic transistors.

2.3 Conclusion

In conclusion, the morphology of zone-cast thin films of the molecular semiconductor C8-BTBT can be categorized into three subregimes, featuring crystalline domains that are I) isotropic, II) unidirectional crystal stripes, and III) corrugated and dendritic. Whereas I) and II) are typically found in the evaporative coating regime, III) is primarily produced in the Landau-Levich regime. Increasing the solution concentration does not directly affect the morphology, but merely increases the critical casting speeds that mark the transitions between the morphology subregimes. Numerical simulation of the fluid dynamics in the coating bead and crystallization in the deposited film, explains the occurrence of morphology I by premature random nucleation resulting from a significantly elevated local solute concentration at low

speed. The band-like structure, low roughness and, as shown by GIWAXS, significant molecular order obtained in subregime II, provides for optimal electrical performance in organic field-effect transistors. We expect the insight gained in this work, in particular the proposition of an optimal processing window, to be valuable for ensuring reproducible device manufacture by meniscus-guided coating techniques.

The content of this chapter has been published in *Advanced Functional Materials*.

Reprinted with permission from (*Adv. Func. Mater.* 2022, 32, 2107976)

Copyright © 2022, “John Wiley and Sons” publishing group.

References

1. Janneck, R., et al., *Predictive Model for the Meniscus-Guided Coating of High-Quality Organic Single-Crystalline Thin Films*. *Advanced Materials*, 2016. **28**(36): p. 8007-8013.
2. Giri, G., et al., *Tuning charge transport in solution-sheared organic semiconductors using lattice strain*. *Nature*, 2011. **480**(7378): p. 504-508.
3. Zhang, Z., et al., *Marangoni-Effect-Assisted Bar-Coating Method for High-Quality Organic Crystals with Compressive and Tensile Strains*. *Advanced Functional Materials*, 2017. **27**(37): p. 1-9.
4. Chai, Z., S.A. Abbasi, and A.A. Busnaina, *Scalable Directed Assembly of Highly Crystalline 2,7-Dioctyl[1]benzothieno[3,2- b][1]benzothiophene (C8-BTBT) Films*. *ACS Applied Materials Interfaces*, 2018. **10**(21): p. 18123-18130.
5. Riera-Galindo, S., A. Tamayo, and M. Mas-Torrent, *Role of Polymorphism and Thin-Film Morphology in Organic Semiconductors Processed by Solution Shearing*. *ACS Omega*, 2018. **3**(2): p. 2329-2339.
6. Derjaguin, B., *Thickness of liquid layer adhering to walls of vessels on their emptying and the theory of photo-and motion-picture film coating*. *Proceedings of the USSR Academy of Sciences*, 1943. **39**: p. 13–16.
7. Levich, L.L.a.B., *Dragging of a Liquid By a Moving Plate*. *Acta Physicochimica*, 1942. **17**: p. 141-153.
8. Janneck, R., et al., *Predictive Model for the Meniscus-Guided Coating of High-Quality Organic Single-Crystalline Thin Films*. *Advanced Materials*, 2016. **28**(36): p. 8007-8013.
9. Janneck, R., et al., *Influence of Solute Concentration on Meniscus-Guided Coating of Highly Crystalline Organic Thin Films*. *Advanced Materials Interfaces*, 2019. **6**(19): p. 1-11.
10. Chai, Z., S.A. Abbasi, and A.A. Busnaina, *Scalable Directed Assembly of Highly Crystalline 2,7-Dioctyl[1]benzothieno[3,2-b][1]benzothiophene (C8-BTBT) Films*. *ACS Applied Materials and Interfaces*, 2018. **10**(21): p. 18123-18130.
11. Kwon, S., et al., *Organic Single-Crystal Semiconductor Films on a Millimeter Domain Scale*. *Advanced Materials*, 2015. **27**(43): p. 6870-6877.

12. Izawa, T., E. Miyazaki, and K. Takimiya, *Molecular Ordering of High-Performance Soluble Molecular Semiconductors and Re-evaluation of Their Field-Effect Transistor Characteristics*. *Advanced Materials*, 2008. **20**(18): p. 3388-3392.
13. Hideaki Ebata, T.I., Eigo Miyazaki, Kazuo Takimiya, Masaaki Ikeda, Hirokazu Kuwabara, and Tatsuto Yui, *Highly Soluble [1]Benzo[thien][3,2-b]benzothiophene (BTBT) Derivatives for High-Performance, Solution-Processed Organic Field-Effect Transistors*. *Journal of American Chemical Society*, 2007. **129**: p. 15732-15733.
14. Michels, J.J., et al., *Predictive modelling of structure formation in semiconductor films produced by meniscus-guided coating*. *Nature Materials*, 2020.
15. Janneck, R., et al., *Influence of Solute Concentration on Meniscus-Guided Coating of Highly Crystalline Organic Thin Films*. *Advanced Materials Interfaces*, 2019. **6**(19).
16. Peng, B., Z. Wang, and P.K.L. Chan, *A simulation-assisted solution-processing method for a large-area, high-performance C10-DNTT organic semiconductor crystal*. *Journal of Materials Chemistry C*, 2016. **4**(37): p. 8628-8633.
17. Chen, M., et al., *Understanding the Meniscus-Guided Coating Parameters in Organic Field-Effect-Transistor Fabrications*. *Advanced Functional Materials*, 2020. **30**(1): p. 1-8.
18. Zhang, K., et al., *Key role of the meniscus shape in crystallization of organic semiconductors during meniscus-guided coating*. *Materials Horizons*, 2020. **7**(6): p. 1631-1640.
19. Hsueh, C., *Drying of complex fluids near the contact line: experimental and numerical studies*. Université Pierre et Marie Curie - Paris VI, 2012.
20. Zhang, K., et al., *Crystallization Control of Organic Semiconductors during Meniscus-Guided Coating by Blending with Polymer Binder*. *Advanced Functional Materials*, 2018. **28**(50).
21. Le Berre, M., Y. Chen, and D. Baigl, *From convective assembly to landau - Levich deposition of multilayered phospholipid films of controlled thickness*. *Langmuir*, 2009. **25**(5): p. 2554-2557.
22. Doumenc, F., J.B. Salmon, and B. Guerrier, *Modeling Flow Coating of Colloidal Dispersions in the Evaporative Regime: Prediction of Deposit Thickness*. *Langmuir*, 2016. **32**(51): p. 13657-13668.
23. Jing, G., et al., *Drying of colloidal suspensions and polymer solutions near the contact line: deposit thickness at low capillary number*. *Langmuir*, 2010. **26**(4): p. 2288-93.

24. Lee, J.-C., et al., *Meniscus-Guided Control of Supersaturation for the Crystallization of High Quality Metal Organic Framework Thin Films*. Chemistry of Materials, 2019. **31**(18): p. 7377-7385.
25. Doumenc, F. and B. Guerrier, *Self-patterning induced by a solutal Marangoni effect in a receding drying meniscus*. Europhysics Letters, 2013. **103**(1).
26. Bodiguel, H., F. Doumenc, and B. Guerrier, *Stick-slip patterning at low capillary numbers for an evaporating colloidal suspension*. Langmuir, 2010. **26**(13): p. 10758-63.
27. Perez-Rodriguez, A., et al., *Decoding the Vertical Phase Separation and Its Impact on C8-BTBT/PS Transistor Properties*. ACS Applied Materials and Interfaces, 2018. **10**(8): p. 7296-7303.
28. Chai, Z., S.A. Abbasi, and A.A. Busnaina, *Scalable Directed Assembly of Highly Crystalline 2,7-Dioctyl[1]benzothieno[3,2- b][1]benzothiophene (C8-BTBT) Films*. ACS Applied Materials and Interfaces, 2018. **10**(21): p. 18123-18130.
29. Giri, G., et al., *Tuning charge transport in solution-sheared organic semiconductors using lattice strain*. Nature, 2011. **480**(7378): p. 504-8.
30. Kwon, S., et al., *Organic Single-Crystal Semiconductor Films on a Millimeter Domain Scale*. Advanced Materials, 2015. **27**(43): p. 6870-7.
31. Lee, J.H., et al., *Effect of Crystallization Modes in TIPS-pentacene/Insulating Polymer Blends on the Gas Sensing Properties of Organic Field-Effect Transistors*. Scientific Reports, 2019. **9**(1): p. 21.
32. Zhang, K., et al., *Interlayers for Improved Hole Injection in Organic Field-Effect Transistors*. Advanced Electronic Materials, 2020. **6**(6).
33. Ablat, A., et al., *Role of Oxide/Metal Bilayer Electrodes in Solution Processed Organic Field Effect Transistors*. Scientific Reports, 2019. **9**(1): p. 1-8.
34. Waldrip, M., et al., *Contact Resistance in Organic Field-Effect Transistors: Conquering the Barrier*. Advanced Functional Materials, 2019. **1904576**: p. 1-31.
35. Shen, T., et al., *Wettability Control of Interfaces for High-Performance Organic Thin-Film Transistors by Soluble Insulating Polymer Films*. ACS Omega, 2020. **5**(19): p. 10891-10899.
36. Janneck, R., et al., *Influence of the Surface Treatment on the Solution Coating of Single-Crystalline Organic Thin-Films*. Advanced Materials Interfaces, 2018. **5**(12): p. 1-9.

37. Choi, H.H., et al., *Critical assessment of charge mobility extraction in FETs*. Nature Materials, 2017. **17**(1): p. 2-7.
38. Kalb, W.L. and B. Batlogg, *Calculating the trap density of states in organic field-effect transistors from experiment: A comparison of different methods*. Physical Review B, 2010. **81**(3).
39. Choi, H.H., et al., *Critical assessment of charge mobility extraction in FETs*. Nature Materials, 2017. **17**(1): p. 2-7.

Chapter 3 Role of meniscus shape on crystallization of molecular semiconductors and fluid dynamics during meniscus-guided coating

3.1 Introduction

To control the thin film morphology during MGC, the individual process parameters and their coupling have been studied.[1] Particularly, the evaporation-induced concentration gradient at the meniscus contact line as seen in **Figure 3.1** is crucial for the formation of the thin film morphology. For instance, the film roughness of MGC films greatly varies, depending on the relation between the boiling temperature of the solvent T_b and the deposition temperature T . As T increases and approaches T_b , the concentration gradient increases, resulting in a smoother surface film morphology.[2] Secondly, an optimized solute concentration (c_s) of 0.4 wt % TIPS-pentacene in hexane after MGC results in few structural defects and therefore in improved charge carrier mobility and lowered contact resistance at the metal electrode / OSC interface of the OFET device.[3] Our previous work has shown that c_s should also be optimized towards the coating velocity v because of morphological transitions at different v . [4] Such morphological transitions occur at critical coating velocity that depends on the solute concentration. The critical coating velocity increases with solute concentration.[4] Moreover, limited mass transport at the contact line results in misaligned OSC crystals with respect to coating direction. One solution to this problem is to design a coating head which allows for an enhanced mass transport towards the contact line, thereby influencing the crystallization of OSC solute. As a result, enhanced fluid flow provides a better crystal alignment and low device-to-device variation in OFET performance.[5, 6]

Another way to exert control is by tuning the gap distance d between the coating head and the substrate, as it influences the shape of the meniscus, as we will show below. The number of studies in present literature that include the gap distance as an optimization parameter for

MGC is small. This is perhaps surprising, as, in particular for advanced methods such as zone casting and slot-die coating, the gap distance seems to be a readily accessible feature for exerting control. Born et al. studied the influence of the gap distance of the meniscus on the film formation of polystyrene microparticles from solution during MGC. At 160 μm a stable meniscus was obtained, whereas a larger gap distance resulted in an increase in the depinning length (a maximum displacement) of the contact line, resulting in an inhomogeneous distribution of the microparticles and a strongly deformed film.[7] In another example, the meniscus shape was controlled by dip-coating C8-BTBT by tilting the substrate at different angles with respect to the surface of the liquid.[8] As shown by numerical simulations, the concentration gradient at the contact line becomes steeper with a decreasing tilt angle, which leads to an enhanced coverage and crystallinity of the film. The effect of the meniscus shape, as determined by the gap distance, on the fluid dynamics in the coating bead remains poorly understood and has so far not been systematically studied in case of a crystallizing small molecular solute. For that reason, at present no guidelines exist for attaining further process control through optimizing the gap distance.

In this work, we account for this and investigate the role of the meniscus shape by systematically varying the gap distance during zone-casting of TIPS-pentacene as a highly crystalline model semiconductor. We study how the gap distance affects the fluid dynamics in the bead, as well as the thin film morphology. At a given coating velocity in the evaporative coating regime, upon decreasing the gap distance we identify a transition from a ‘stick-slip’ type structure (Morphology I) towards a favorable unidirectionally aligned morphology (Morphology II). Upon entering the hydrodynamic coating regime at a high coating velocity, we observe an isotropic spherulitic morphology for a large gap distance (Morphology III), which transforms in a more directional, branched structure (Morphology IV) when the gap distance is increased. Numerical simulation of the steady state fluid flow pattern in the bead

provides information about the impact of the meniscus shape on the concentration and temperature gradients in the coating bead. Finally, we show that the favorable directionality and considerable grain size in the aligned morphology II leads to a low trap density, giving optimal OFET performance with respect to saturation and effective mobility.

3.2 Results and Discussion

3.2.1 TIPS-pentacene morphology

Figure 3.1 gives a schematic representation of the zone casting process, including the deposition head geometry, the gap distance d , and the concentration field.[4] As the substrate moves at a constant velocity v , the solvent evaporates dominantly at the front meniscus and the solute accumulates towards the contact line of the front meniscus. During deposition, a continuous solution supply is provided via the inlet to maintain a stable deposition head with a constant volume. As shown by numerical simulations in previous work[4], the flow pattern in our set-up typically comprises two vortices, resulting from the inlet solution supply, substrate entrainment, and solvent evaporation. At low coating velocities (i.e., in the evaporative regime), the deposited film crystallizes immediately after the contact line; at substantially higher coating velocities (i.e., in the Landau-Levich regime), the film crystallization generally occurs further downstream from the contact line.[1, 9, 10]

In this study, we chose TIPS-pentacene as a model compound for the zone-casting experiments. TIPS-pentacene is known to exhibit a high crystallinity and the ability to form unidirectionally aligned crystals, owing to its brick-wall packing and long-range molecular arrangements.[5, 11-13] The compound was dissolved in THF at a concentration of 1.00 mg ml⁻¹. Five different gap distances in the range $0.05 \leq d \leq 2.00$ mm were set to control the meniscus shape at four different coating velocities in the range $0.1 \leq v \leq 0.6$ mm s⁻¹. The coating

velocities were selected within the “optimized window”, as described in chapter 2[4] and represent the evaporative regime, with the upper limit extending into the transition towards the Landau-Levich regime. In this velocity window, we observed unidirectionality and homogeneous alignment in thin films of the semiconductor C8-BTBT, which behaves similar to TIPS-pentacene when applied by MGC.[11, 14] The morphology of the deposited films was characterized by POM and AFM.

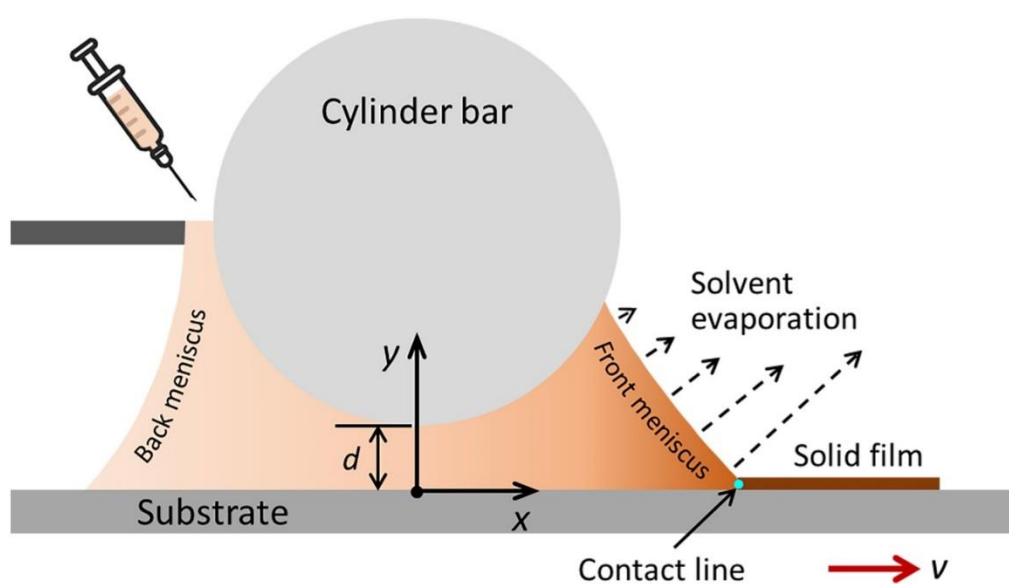


Figure 3.1 A schematic illustration of the meniscus during zone casting with the solute concentration field. The deposition head is formed between a cylinder bar and a substrate, which are separated by a gap distance of d . The front meniscus shows predominant solvent evaporation as the substrate moves at a coating speed of v .

The POM images in **Figure 3.2** reveal four types of crystalline morphologies resulting from the interplay between the gap distance d and the coating velocity v . In general terms we observe: I) ‘interrupted unidirectional bands’ for a high d and a low v , II) ‘uninterrupted

unidirectional bands' for a low d and a low v , III) spherulites for a high d and a high v , and IV) a 'directional branched' structure for a low d and a high v . The directionality in morphologies I, II and IV aligns with the coating direction (white arrow), expressing principle control over crystal growth in the evaporative and transition regimes.[4, 15] Close inspection of Morphology I reveals that the 'interruptions' are in fact ridges that extend perpendicular to the coating direction, comprising small needle-like crystals that, in contrast to the bands in the intermittent regions, do not seem to have a particular directionality. The periodicity of the irregularity exhibits a qualitative reciprocal relation with the gap distance and disappears at the transition I→II. Below we propose an origin for the ridges in Morphology I with the aid of numerical simulations of the fluid dynamics in the coating bead, taking into account the non-uniform temperature distribution.

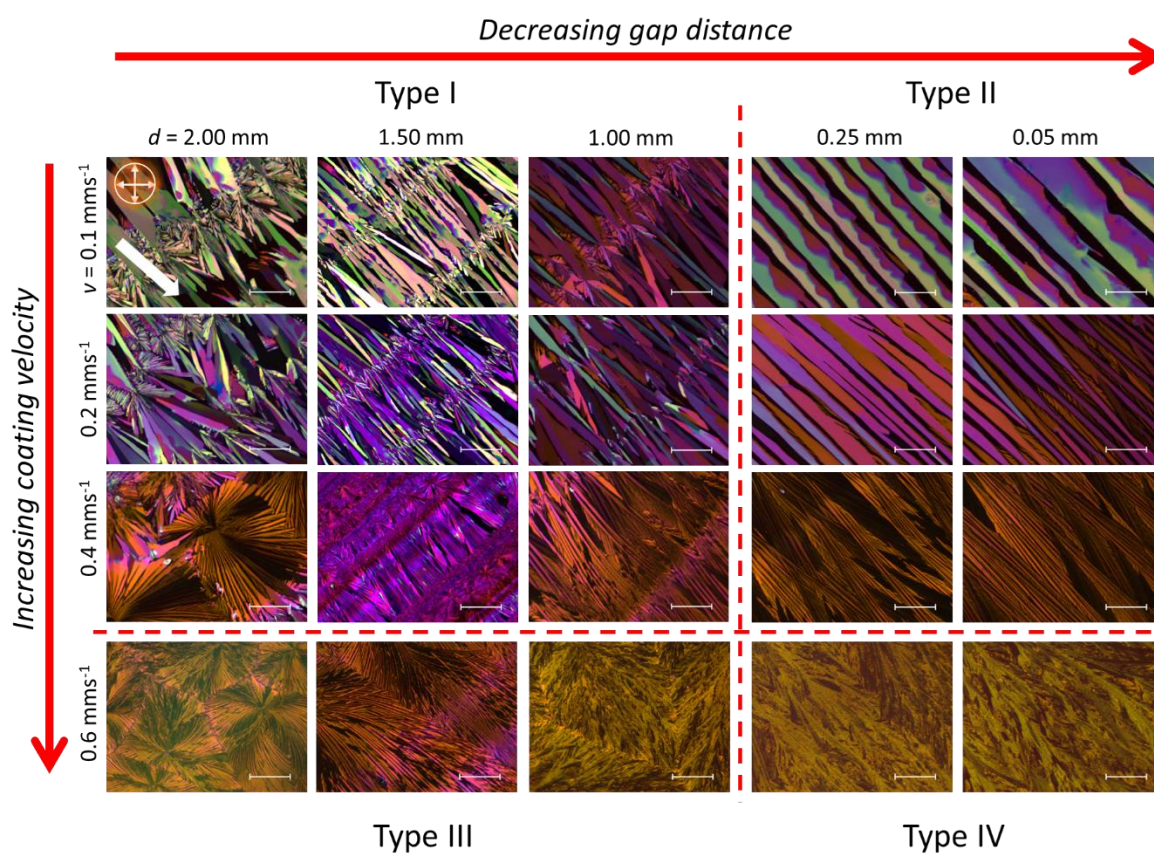


Figure 3.2. POM images of zone-cast TIPS-pentacene films deposited at the gap distances $d =$

2.00, 1.50, 1.00, 0.25 and 0.05 mm and coating velocities $v = 0.1, 0.2, 0.4$ and 0.6 mm s^{-1} . The white arrow and the crossed arrows in the first image indicate the coating direction and the position of two polarizers, respectively. Three morphological subregimes separated with red dashed lines are indicated. All scale bars are $50 \mu\text{m}$.

Both morphology types I and II reveal a gradually decreasing crystal band width from $\sim 30 \mu\text{m}$ to $\sim 3 \mu\text{m}$ when v is increased from 0.1 to 0.4 mm s^{-1} (**Figure 3.2**). We observed the same effect for zone-cast C8-BTBT.[4] In principle, each crystal stripe represents a nucleation center and a higher v increases the nucleation density due to the enhanced concentration gradient near to the contact line, giving rise to narrower bands.[4] When v is increased to 0.6 mm s^{-1} , a spherulitic morphology or directional branched structure emerge (types III and IV). For a gap distance of $d < 0.25 \text{ mm}$, the structure in the type IV morphology still follow the coating direction. This is an important observation from an application point-of-view, as cast effective production requires control at a maximum coating velocity. However, at a higher gap distance the orientation is lost and the domains become isotropic (Morphology III). Besides POM analysis, AFM was performed to evaluate the surface roughness and average grain size of the deposited thin films. At $d = 0.05 \text{ mm}$, the lowest RMS were obtained of $\sim 15 \text{ nm}$ at 0.1 mm s^{-1} and $\sim 7 \text{ nm}$ at 0.6 mm s^{-1} (**Figure 3.3g**). Increasing the gap distance to 1.00 mm and 2.00 mm caused a gradual increase in the RMS roughness of the thin films for type I and II morphologies. As also shown in **Figure 3.3g**, the largest grains ($\sim 260 \mu\text{m}^2$) were produced for at $d = 0.05 \text{ mm}$ and $v = 0.1 \text{ mm s}^{-1}$ and decreases to $\sim 33 \mu\text{m}^2$ at $d = 2.00 \text{ mm}$. On the other hand, the average grain size at $v = 0.6 \text{ mm s}^{-1}$ remains almost constant with respect to the gap distance for type III morphology.

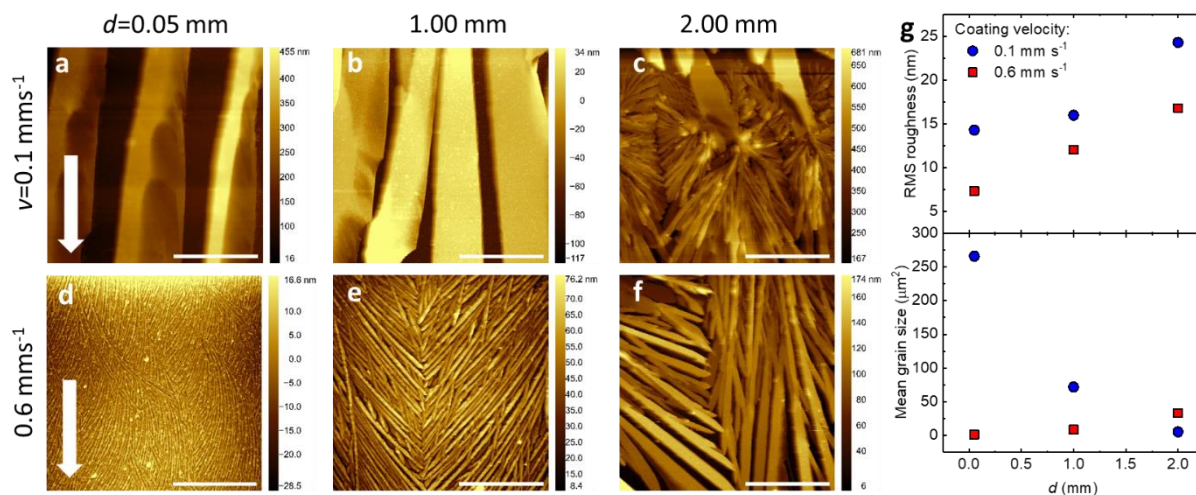


Figure 3.3 (a-f) AFM images of zone-cast TIPS-pentacene films at three gap distances ($d = 0.05$, 1.00 and 2.00 mm) and two coating velocity ($v = 0.1$ mm s⁻¹ and 0.6 mm s⁻¹). The white arrows indicate the casting direction. All scale bars are 30 μm. (g) RMS roughness and mean grain size analysis of the AFM images in (a-f).

Next, we focus on the origin of the perpendicular ridges that appear in Morphology I. The fact that the needle like crystals in these ridges (see **Figure 3.2**) grow isotropically suggests that the contact line is temporarily, but periodically, stationary relative to the substrate. In other words, it temporarily moves along with the substrate rather than sliding across it, implying that unidirectional control is lost for a small time interval. This mechanism is consistent with the phenomenon that under the influence of Marangoni stress the meniscus may exhibit a hydrodynamic instability which causes it to periodically bulge into the coating direction.[15, 16] This instability stems from the surface tension gradients along the coating direction, which may be induced by local variation in composition and/or temperature. Since in the evaporative coating regime the solute concentration remains very low in the bead, except at the contact line, we deem temperature gradients to be the primary origin for the Marangoni flow. To evaluate the significance of the solutal Marangoni effect, we conducted surface tension measurements

on TIPS-pentacene / THF solutions with concentrations of $c_0 = 1.56 \text{ mol m}^{-3}$ and $c_1 = 15.6 \text{ mol m}^{-3}$ (see **Figure 3.4**). The similar surface tensions of both solutions corroborate our choice of neglecting the solutal Marangoni effect and focusing only on the thermal Marangoni effect.

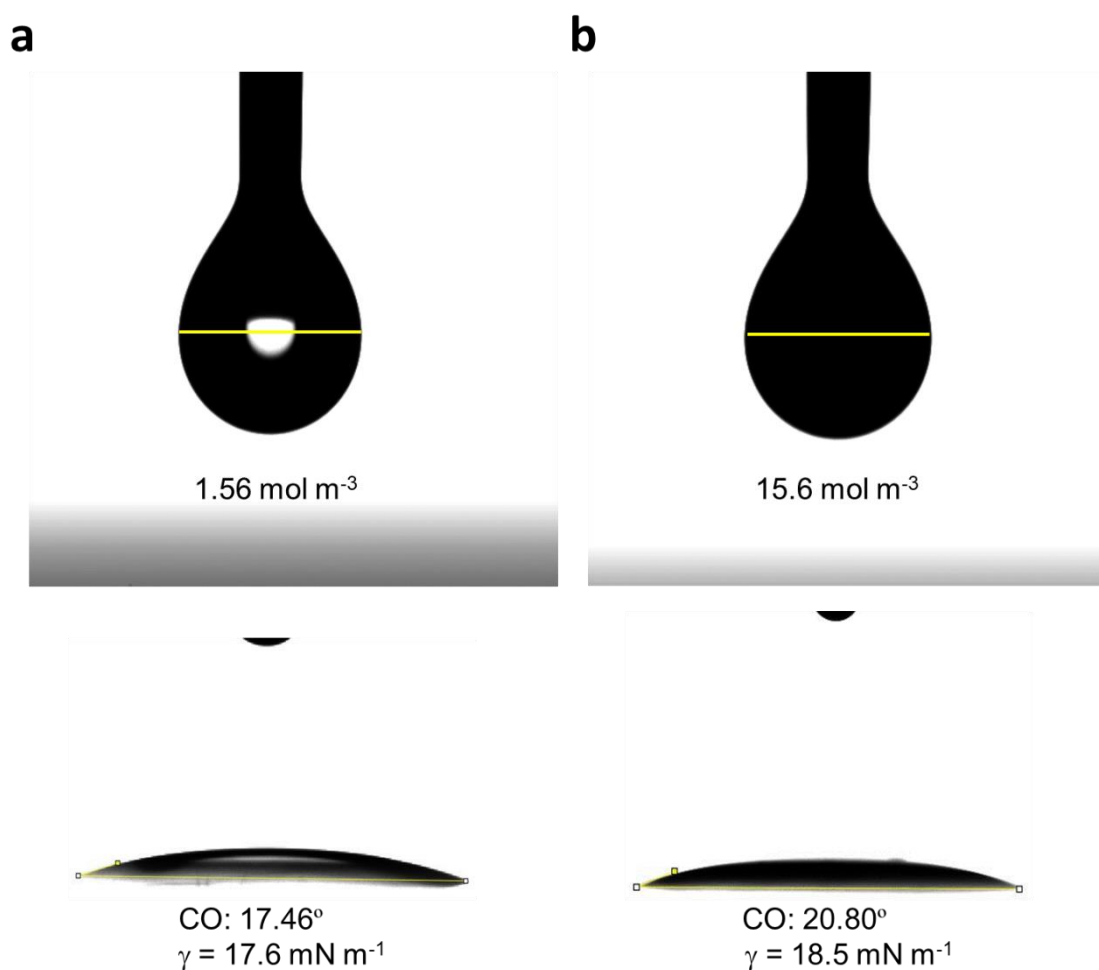


Figure 3.4 The pendant drop measurements of TIPS-pentacene / THF solution with two different concentrations (a) 1.56 mol m^{-3} (1.0 mg ml^{-1}) and (b) 15.6 mol m^{-3} (10.0 mg ml^{-1}) are shown in the graph. The corresponding contact angle (CO) and surface tension (γ) results are at the bottom line.

3.2.2 Numerical analysis in coating bead

To support this hypothesis, we performed two-dimensional (2D), steady-state numerical simulations of the fluid flow, temperature, and concentration fields in the coating bead in the low speed regime [4, 17, 18] at varying gap distances ($d = 0.05, 1.00, \text{ and } 2.00 \text{ mm}$) and coating velocities ($v = 0.1 \sim 0.6 \text{ mm s}^{-1}$). We solved the Navier-Stokes (NS) equations, in conjunction with the convection-diffusion equations for heat and concentration and accounting for the thermal Marangoni effect. The considered material system is a solution of TIPS-pentacene (solute) in THF (solvent) with a concentration of $c_0 = 1.56 \text{ mol m}^{-3}$ at the inlet. Considering the low solute concentration in the coating bead (except for the region near the contact line), we adopted the THF properties as the solution properties (including the density [19], viscosity [20], heat capacity [21], thermal conductivity [22], surface tension [23], and enthalpy of vaporization [24, 25]), and took the temperature dependencies of the properties into account. The shape of the simulation box was physically pre-determined and fixed to match the shape of the actual coating bead. [4] As was done in chapter 2 [3, 4, 26], we cut a small region near the contact line of the front meniscus to explicitly allow the solution to exit the simulation domain upon entrainment. In agreement with the experiments, the solute concentration at the inlet was fixed at $c_0 = 1.56 \text{ mol m}^{-3}$, and the temperatures of the substrate, cylinder bar, and inlet solution were set to be constant at $45 \text{ }^\circ\text{C}$. The boundary condition at the outlet was set to be “outflow”. At the substrate no-slip conditions were assumed. Solvent evaporation was assumed to occur primarily at the front meniscus and negligible at the back meniscus. The evaporation rate j was assumed to be $j(x) = A/[(x_{\text{tip}} - x + B)/1[\mu\text{m}]]^{1.5}$, which ensures an escalation in the evaporation rate towards the contact line of the front meniscus, characteristic to coating in the ER. Similar to 2D simulation of fluid flow in chapter 2 [4], we chose $B = 1 \mu\text{m}$ and iteratively determined $A = 7.6555 \times 10^{-3} \text{ m s}^{-1}$ by imposing mass conservation of the solvent

in the cut region. The deposited film thickness was obtained by equating the solute mass flux at the inlet and outlet via $h = v^{-1} \int_0^{y_{\text{cut}}} u(y)\phi(y)dy$, where $u(y)$ and $\phi(y)$ are the substrate velocity and solute volume fraction at the position of the cut.[4]

Figure 3.5a illustrates the simulation domain, boundary conditions, coordinate system, and exemplary flow and temperature fields at $d = 0.05$ mm and $v = 0.6$ mm/s. The combined effects of the inlet solution supply, substrate entrainment, solvent evaporation, and thermal Marangoni flow lead to unique streamline distributions that feature four vortices in the simulation domain and one stagnation point on the front meniscus. At the stagnation point the local fluid velocity is zero, effectively separating flow patterns with opposite flow directions. The zoomed-in image (**a1**) in **Figure 3.5a** shows a local low-temperature region due to the strongly enhanced solvent evaporation near the contact line, whereas the zoomed-in image (**a2**) depicts the aforementioned cut region that allows the solute to leave the simulation box.

Figures 3.5b-d show the solute concentration fields together with the corresponding flow streamlines at $d = 0.05$, 1.00, and 2.00 mm, respectively. As d increases from 0.05 to 1.00 mm, the number of vortices decreases from four to three; as d further increases to 2.00 mm, the relative sizes of the three vortices change. In all cases, the solute concentration considerably increases towards the contact line, with the size of the high-solute-concentration region decreasing with the gap distance. Nevertheless, the present simulations do not take solutal-Marangoni flow into account, as we confirmed with separate measurements that the surface tension of the solution does not change appreciably with concentration. In contrast to ref.[26], where the temperature gradient-induced thermal Marangoni flow hinders the delivery of solution to the contact line at the front meniscus, the thermal Marangoni effect in the present study promotes the solution delivery to the contact line, as indicated by the direction of the streamlines in the vortex near the contact line.

For each of the three gap distances, we varied v from 0.1 to 0.6 mm s⁻¹ and studied the film thickness h . As evident from **Figure 3.5e**, similar thickness values are obtained for gap distances of 0.05 mm and 1.00 mm. At a larger d of 2.00 mm, h increases due to enhanced solvent evaporation in the front meniscus. A similar trend for the dependence of the film thickness on the meniscus gap was observed previously for phospholipids deposited by MGC.[9] At constant v , h increases with d (**Figure 3.5e**) suggesting that the film thickness is closely affected by the fluid flow in the front meniscus due to d . At constant d , h decreases with increasing v , following a trend consistent with the $h \sim v^{-1}$ relation, characteristic for the evaporative regime. It has been shown in literature that the relation $h \sim v^{-1}$ can be obtained by simply equating the outgoing fluxes of the solvent (evaporation) and solute (solidification) to the influx of the native solution.[3, 4, 8, 26] The theoretical thicknesses calculated by the numerical simulations are in excellent agreement with the experimental data at all three gap distances (**Figure 3.5e**).

As long as the scaling for the evaporative regime applies, the concentration far away from the contact line remains virtually independent on v and close to the inlet concentration c_0 . Only in the region near the contact line, the solute concentration drastically rises due to the diverging evaporation rate.[3, 4, 8] As the stagnation point (y_{stag}) at the front meniscus, which defines a point where the upstream back flow and downstream flow split (**Figure 3.5a**), is an important feature of the flow field, we have studied its dependence on the gap distance and coating velocity. As shown in **Figure 3.5f**, y_{stag} increases linearly with v at a constant d and shows a prominent jump as d is increased from 0.05 to above 1.00 mm. The downstream flow transports the solute to the contact line. Therefore, y_{stag} (or the size of the downstream region below the stagnation point) seems crucial for the crystallization process.[4, 8, 17] Interestingly, the smaller y_{stag} values at $d = 0.05$ mm (**Figure 3.5f**) correspond to the smaller film thicknesses

(**Figure 3.5e**), as compared to the situations at $d = 1.00$ and 2.00 mm. In **Figure 3.5g**, we show the temperature gradients along the front meniscus as a function of x for three gap distances at $v = 0.6 \text{ mm s}^{-1}$ (the v -dependence of the temperature gradients were found to be negligible). Surprisingly, the temperature gradient distributions are nearly identical at the three gap distances, suggesting a weak dependence of the thermal Marangoni effect on the gap distance. The temperature distribution as represented by the variable color in **Figure 3.5a** indicates significant temperature changes mainly close to the contact line at the front meniscus. This is due to the predominant solvent evaporation causing cooling (blue color) at the front meniscus. Therefore, the numerical simulations provide a quantification of the influences of the gap distance and coating velocity on the film thickness and the flow (e.g., vortices, stagnation point), temperature (e.g., temperature, temperature gradient), and solute concentration fields in the bead.

Next, we outline how our simulations provide for a possible explanation for the periodic “ridges” normal to the coating direction, as seen in the POM images of films obtained at high gap distances and low coating velocities (**Figure 3.2**). According to **Figure 3.5g**, the thermal Marangoni effect is comparable for all three gap distances. However, since a higher gap distance means a larger vertical distance from the substrate to the front meniscus, for example, below the stagnation point, **Figure 3.5f** and a lower coating velocity means a smaller velocity gradient from the substrate up to the free surface of the front meniscus, both a high gap distance and a low coating velocity reduces the shear rate in the front of the meniscus or, in other words, weakens the viscous entrainment by the substrate. Whereas the viscous entrainment effect stabilizes the coating bead, the thermal Marangoni effect counteracts. When the former dominates over the latter (i.e. at small d 's and/or large v 's), uniform solid films are formed; otherwise, “ridges” normal to the coating direction start to appear, possibly originating from a

hydrodynamic instability similar to the one described by Doumenc et al.[16], here driven by thermal Marangoni stress. Therefore, the finite element simulations accounting for the thermal Marangoni effect at varying gap distances and coating velocities allow us to provide an explanation for the “Type I \rightarrow Type II” morphology transition.

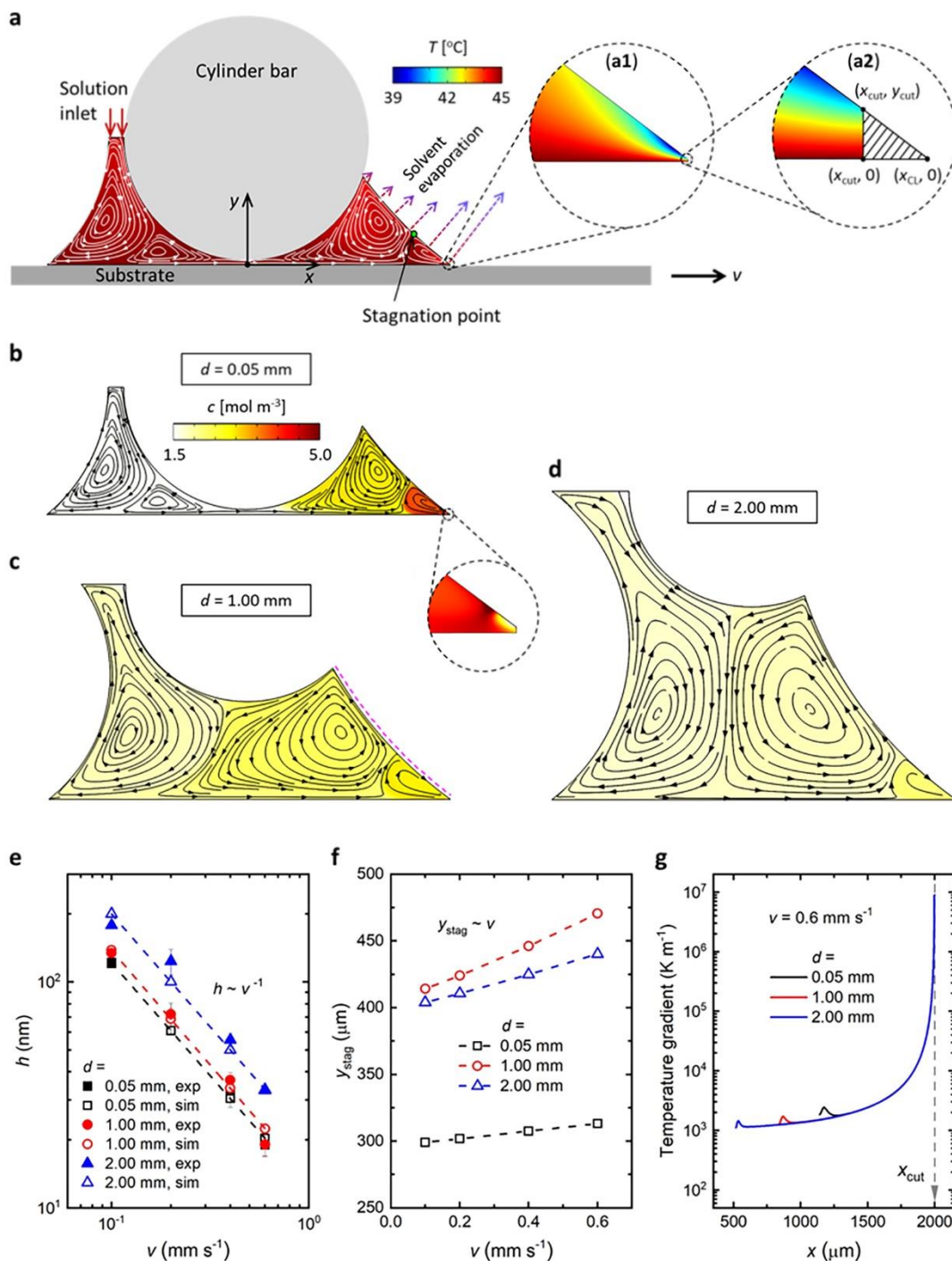


Figure 3.5 Finite element simulations of the flow, temperature, and concentration fields in the meniscus during zone-casting of TIPS-Pentacene. a) Illustration of the simulation domain, boundary conditions, and coordinate system. The strong solvent evaporation near the contact line results in a local low temperature region [zoomed-in image (a1)]. A small region near the contact line is cut to allow the solute to leave the simulation domain [zoomed-in image (a2)].

Flow and concentration fields for (b) $d = 0.05$ mm, (c) $d = 1.00$ mm, and (d) $d = 2.00$ mm. The results in a)-d) correspond to $c_0 = 1.56$ mol m^{-3} and $v = 0.6$ mm s^{-1} . e) Experimental and calculated film thicknesses h as a function of the casting speed v at three gap distances. f) y coordinate of the stagnation point (see (a)) as a function of the casting speed v at three gap distances. g) Temperature gradient along the front meniscus [see the magenta dashed curve in (c)] as a function of the x coordinate for three gap distances. The casting speed dependence of the temperature gradient is negligible.

3.2.3 Molecular organization

Besides the changes in the film morphology of TIPS-pentacene, we further evaluate the UV-vis absorption. To make a comparison between the thin films, we examine the absorption peak ~ 365 nm (~ 3.4 eV) which corresponds to LUMO level of TIPS-pentacene.[27] The absorption peak ~ 365 nm (3.4 eV) is blue shifted by ~ 7.0 nm for the gap distance of 2.00 mm in comparison to 0.05 mm at both of coating velocity of 0.1 mm s^{-1} (**Figure 3.7a**) and 0.6 mm s^{-1} (**Figure 3.7b**). The spectral change is a sign for differences in the crystal packing of TIPS-pentacene and indicates that the required energy to excite the valence electrons shifts ~ 0.07 eV in respect to the morphological transition. Similarly, spectral changes were observed for C8-BTBT films obtained by off-center and on-center spin-coating.[28] The spectral shift to lower wavelengths implies lower film crystallinity, as in the case for the gap distance of 2.00 mm. This observation is in agreement with the higher crystallinity for films deposited at lower gap distance.

To investigate the dependence of the fluid flow on the molecular organization, grazing incidence wide-angle X-ray scattering (GIWAXS) measurements were performed. Six different morphologies were analyzed obtained at gap distances of 0.05, 1.00 and 2.00 mm and coating

velocity of 0.1 and 0.6 mm s⁻¹ (**Figure 3.2**). The GIWAXS patterns are presented in **Figure 3.6** and display the diffraction peaks of the TIPS-pentacene ordering in out-of-plane and in-plane directions. The thicker films result in higher scattering intensities in the GIWAXS patterns as it is the case for coating velocity of 0.1 mm s⁻¹ (**Figure 3.6a-c**).

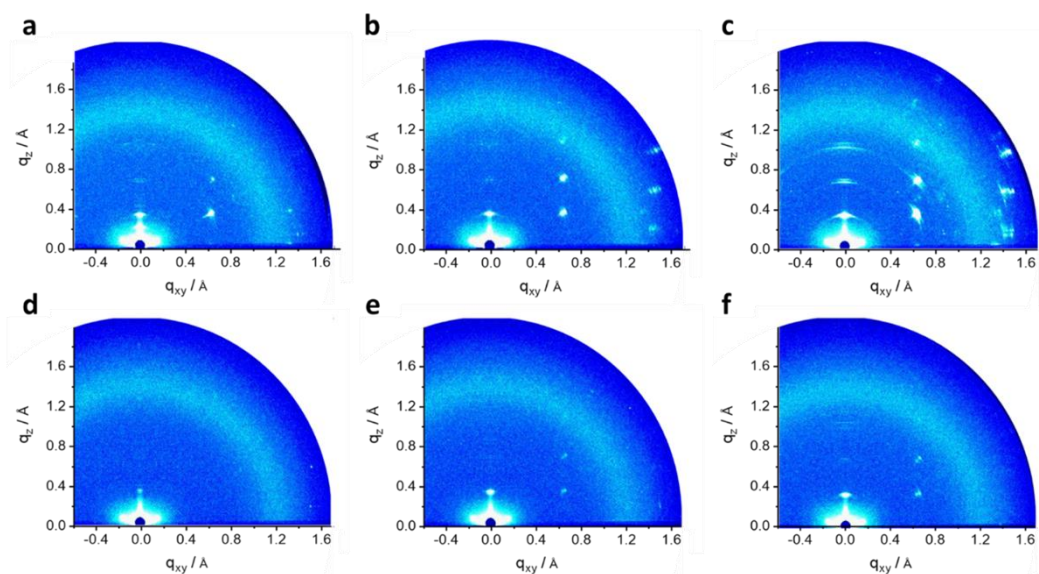


Figure 3.6 GIWAXS patterns for a) 0.05 mm, b) 1.00 mm, c) 2.00 mm at the coating velocity of 0.1 mm s⁻¹ and d) 0.05 mm, e) 1.00 mm, f) 2.00 mm at the coating velocity of 0.6 mm s⁻¹. The measurements were done parallel to the casting direction.

As previously reported,[11] TIPS-pentacene forms brick-wall packing as shown in **Figure 3.7c**. The Miller indices 001 and 100 are attributed to the out-of-plane and in-plane directions as also indicated by the arrows in **Figure 3.7c**. The highest peak intensity is related to the interlayer distance 001 in all cases. The relation between the interlayer distance and the gap distance at two different coating velocities is given in **Figure 3.7d**. At processing conditions of $d = 0.05$ mm and $v = 0.1$ mm s⁻¹ an interlayer distance of 16.1 Å is determined from the 001

peak in **Figure 3.6**. This distance slightly increases to 16.3 Å for 1.00 and 2.00 mm at the same coating speed. Upon increasing the speed to 0.6 mm s⁻¹, the interlayer distance in the main crystal phase decreases to 15.8 Å for $d = 0.05$ mm. For the two gap distances of 1.00 and 2.00 mm at 0.6 mm s⁻¹, the two 001 and 001* peaks are also observed, and the peak variation increased to the range of ~2 Å. The molecular arrangement in out-of-plane direction was found to be dependent on meniscus shape and coating velocity, hence the fluid flow. The type II morphology cast at the gap distance of 0.05 mm reveals a homogenous molecular ordering in the out-of-plane direction as proven by a single 001 diffraction peak.

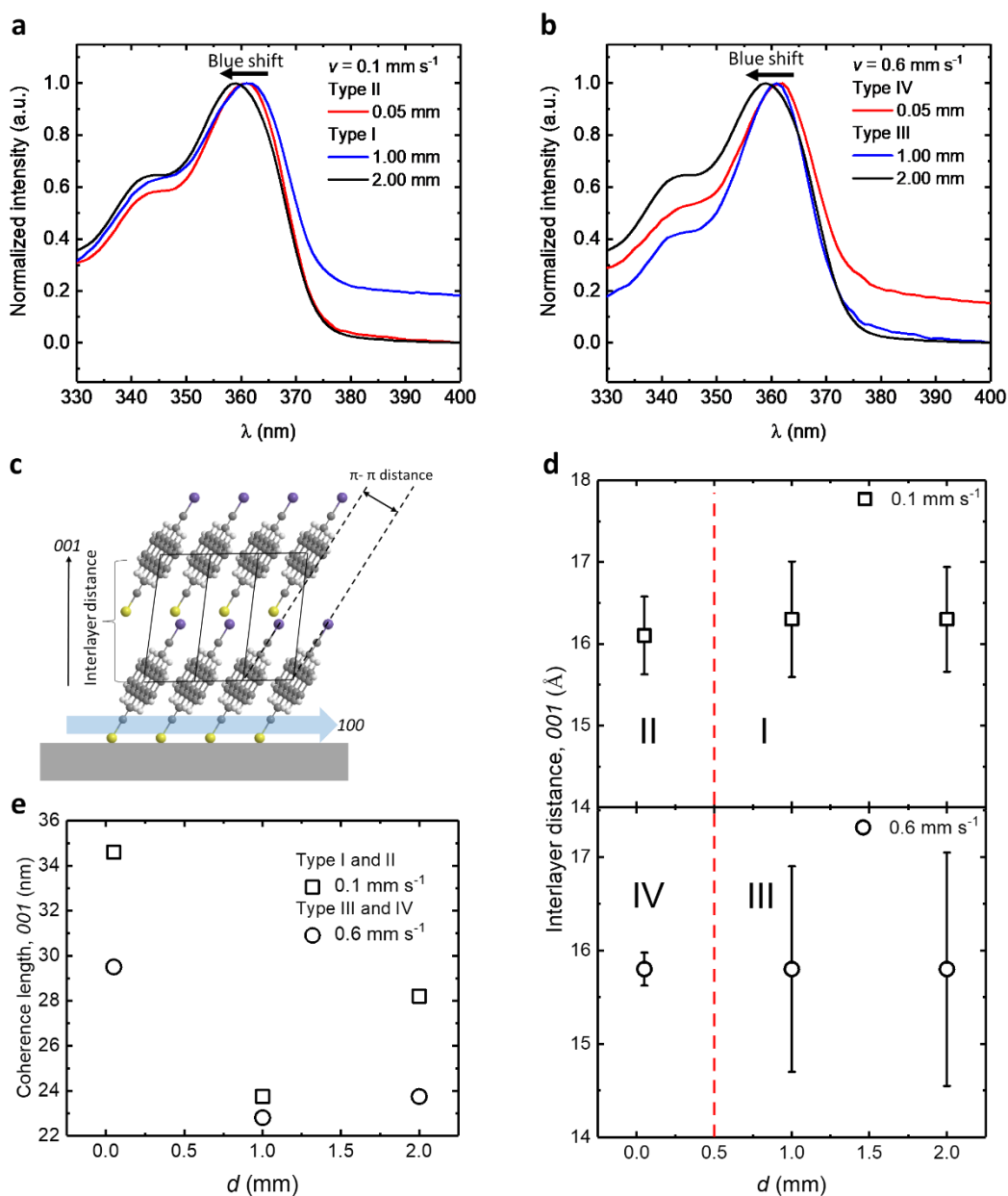


Figure 3.7 UV-Vis absorption of zone-cast TIPS-pentacene films for a) $v = 0.1 \text{ mm s}^{-1}$ with morphology type II ($d = 0.05 \text{ mm}$) and type I (1.00 mm and 2.00 mm) and b) $v = 0.6 \text{ mm s}^{-1}$ with the morphology type III (1.00 mm and 2.00 mm) and type IV (0.05 mm). c) Side view of the molecular packing of zone-cast TIPS-pentacene. 001 represents the out-of-plane direction and 100 represents the in-plane direction. Blue-arrow indicates the casting direction. The interlayer distance (d) and the coherence length of 001 peak (e) are shown as a function of gap distance for the coating velocities of 0.1 mm s^{-1} and 0.6 mm s^{-1} .

To better understand the role of zone-casting conditions on the crystallinity of TIPS-pentacene, we evaluated the coherence length (or crystallite size) by using Scherrer equation.[29] In general, higher coherence length is attributed to a structure that owns low density of grain boundaries. Furthermore, a high coherence length typically is related to lower charge trapping density in the thin films showing improved in-plane charge transport.[4, 11] However, coherence length in the out-of-plane direction similarly affects charge transport. This is mainly because charge carriers are injected from the metal electrode into the OSC and are transported through the bulk film to the OSC/dielectric interface. As shown in **Figure 3.7e**, the coherence length of 001 is ~34.6 nm for films cast at the speed of 0.1 mm s⁻¹ and the gap distance of 0.05 mm. The value drops to ~23.7 nm for 1.00 mm and ~28.2 nm for 2.00 mm. The similar trend for the coherence length is observed for 0.6 mm s⁻¹, whereby lower coherence lengths were calculated in comparison to the speed of 0.1 mm s⁻¹. The coherence length calculations indicate that a higher molecular order and larger crystallite size for the type II morphology achieved at an optimized meniscus (**Figure 3.2**).

3.2.4 OFETs

The charge carrier transport of the zone-cast films is evaluated in field-effect transistors with a BG / TC device configuration. As top contact electrode, 50 nm thick Au was used. The transistor analyzes were completed for over 15 devices for each processing condition. More details regarding transistor characterization can be found in the experimental appendix in chapter 6. The transfer curves are compared in **Figure 3.8a** and **3.8b** for variable gap distances and coating velocities representing the morphologies type II) at 0.05 mm and I) at 1.00 mm and 2.00 mm for 0.1 mm s⁻¹; and III) at 1.00 mm and 2.00 mm and IV) at 0.05 mm for 0.6 mm s⁻¹. The comparison discloses the highest drain-source I_{ds} current in the saturation region for type

II morphology. The saturation mobility μ_{sat} for both coating speeds decrease with increasing d (**Figure 3.8c**). At $v = 0.1 \text{ mm s}^{-1}$, the mobility declines from $0.51 \text{ cm}^2 \text{ V}^{-1} \text{ s}^{-1}$ for $d = 0.05 \text{ mm}$ to $0.15 \text{ cm}^2 \text{ V}^{-1} \text{ s}^{-1}$ for $d = 2.00 \text{ mm}$. This reduction in the charge carrier mobility is explained by the irregularities in the morphology type I (**Figure 3.2**) due to the stick-slip motion of the meniscus and a high density of grain boundaries (**Figure 3.7e**). Upon increasing the speed to 0.6 mm s^{-1} , the charge carrier mobility drops 2 times from $0.22 \text{ cm}^2 \text{ V}^{-1} \text{ s}^{-1}$ to $0.08 \text{ cm}^2 \text{ V}^{-1}$ by lowering d from 0.05 mm to 2.00 mm (**Figure 3.8c**). Although the crystallite size (**Figure 3.7e**) is in a similar range for the speeds 0.1 mm s^{-1} and 0.6 mm s^{-1} , the charge carrier mobility is decreased for type III and IV morphologies due to misalignment of the unidirectional crystals at high speed (**Figure 3.2**).

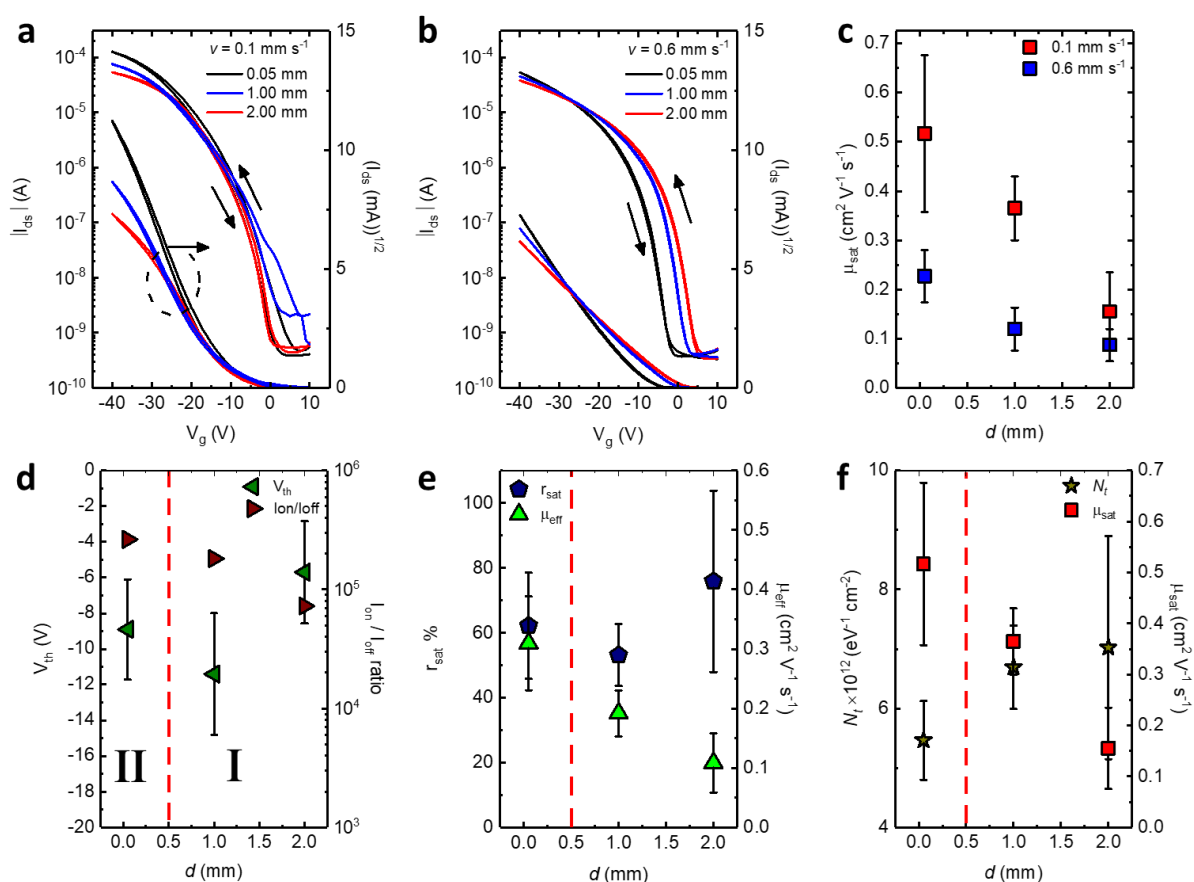


Figure 3.8 The transfer curves are shown for 0.1 mm s^{-1} (a) and 0.6 mm s^{-1} (b) at the gap

distances d of 0.05 mm, 1.00 mm and 2.00 mm. OFET performance as a function of d for $v = 0.1 \text{ mm s}^{-1}$ with c) saturation mobility μ_{sat} (together with 0.6 mm s^{-1}), d) threshold voltage V_{th} and I_{on}/I_{off} ratio, e) reliability factor r_{sat} and effective mobility μ_{eff} and f) trap density N_t . All the measurements were performed at $V_{ds} = -40.0 \text{ V}$ for (a) and (b). The red-dashed line in **Figure 3.8d-f** indicates the morphology transition from type II \rightarrow I.

Figure 3.8d-f exhibits the device analysis for the coating speed of 0.1 mm s^{-1} and different gap distances. The threshold voltage V_{th} in **Figure 3.8d** is comparable for morphology types I and II. On the other hand, the I_{on}/I_{off} ratio slightly decreases from $\sim 2.6 \times 10^5$ to $\sim 7.2 \times 10^4$ similar to the charge carrier mobility. The highest and the average charge carrier mobilities μ_{sat} are determined as $0.80 \text{ cm}^2 \text{ V}^{-1} \text{ s}^{-1}$ and $0.51 \text{ cm}^2 \text{ V}^{-1} \text{ s}^{-1}$ for morphology type II (**Figure 3.8c**).

In comparison to previous literature,[3, 11] the saturation mobility of the zone-cast TIPS-pentacene films in our work is comparable. Nevertheless, the non-ideal transfer curves may generally result in an overestimation of the calculated mobility. For this reason, we also determined the reliability factor r_{sat} and effective mobility μ_{eff} as a function of d presented in **Figure 3.8e**. [30] The morphology type II shows a good reliability factor of $r_{sat} = 62\%$. Furthermore, the trap density N_t is calculated from the subthreshold swing SS based on the following equation[31];

$$SS = \frac{k_B T \ln 10}{q} \left[1 + \frac{q^2}{C_i} N_t \right] \quad (3)$$

, with k_B the Boltzmann constant, T the absolute temperature, q the elementary charge, N_t the trap density and C_i the insulator capacitance. As obvious from **Figure 3.8f**, N_t gradually decreases from morphology type I to II. Morphology type II exhibits the lowest trap density

with $N_t = 5 \times 10^{12} \text{ eV}^{-1} \text{ cm}^{-2}$. Hence, morphology type II results in an improved electrical behavior in OFETs, as evidenced by the enhanced film morphology and coherence length.

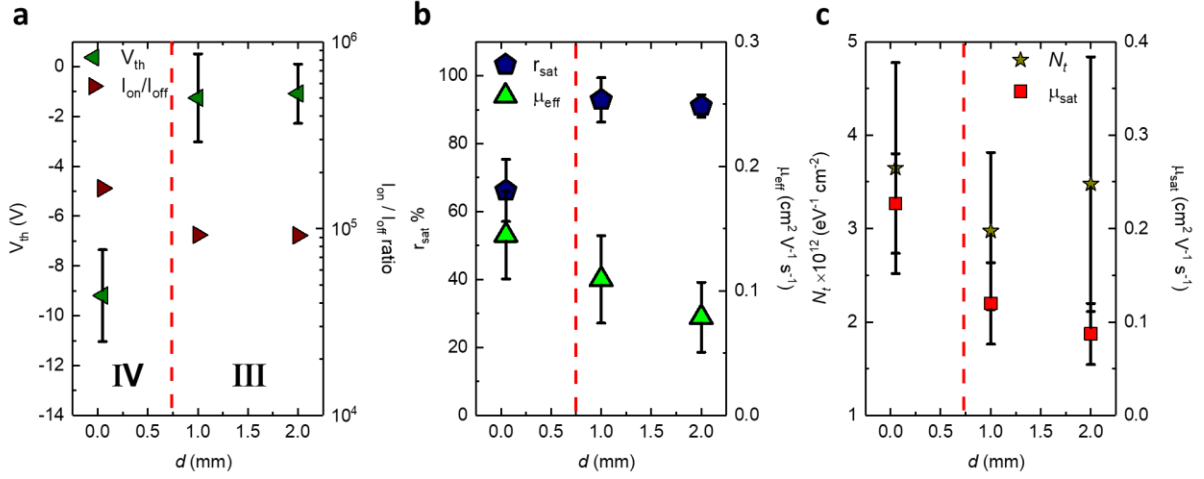


Figure 3.9 OFET performance for type III and IV morphologies as a function of d for $v = 0.6 \text{ mm s}^{-1}$ with a) threshold voltage V_{th} and I_{on}/I_{off} ratio, b) reliability factor r_{sat} and effective mobility μ_{eff} and c) trap density N_t and μ_{sat} .

The comparison between morphology III and IV is shown in **Figure 3.9** with respect to the following parameters: V_{th} , I_{on}/I_{off} ratio, r_{sat} , μ_{eff} , N_t and μ_{sat} . In **Figure 3.9a**, the V_{th} for morphology IV ($d = 0.05 \text{ mm}$) is higher $\sim -9.1 \text{ V}$, then followed by the morphology IV ($d = 1.0 \text{ mm}$ and 2.00 mm) less than $\sim -2.0 \text{ V}$. Furthermore, the I_{on}/I_{off} ratio is slightly lower for 0.05 mm with the value of $\sim 3 \times 10^4$, and goes higher for 1.00 mm and 2.00 mm to a value close to 4×10^5 . In addition, as shown in **Figure 3.9b**, while the r_{sat} is above 60% for the three cases, the calculated μ_{eff} does not exhibit a significant difference and only 0.05 mm exhibiting a slightly higher value close to $0.15 \text{ cm}^2 \text{ V}^{-1} \text{ s}^{-1}$. At last, **Figure 3.9c** presents the comparison for the trap density N_t where 0.05 mm gap distance obtained a value slightly higher $\sim 3.6 \times 10^{12} \text{ eV}^{-1} \text{ cm}^{-2}$.

1 cm^{-2} , which is in agreement with V_{th} . This is because the V_{th} is the voltage required to fill the charge traps to turn the transistor electrically on. However, the morphology III and IV did not present a significant difference with respect to the gap distance which could be due to that at higher speed (0.6 mm s^{-1}), the crystal misalignment increased regarding the casting direction as shown by the AFM images in **Figure 3.3** and by the POM images in **Figure 3.2**. This variation in the crystal misalignment makes it difficult to evaluate the effect of the gap distance at 0.6 mm s^{-1} .

3.3 Conclusions

In conclusion, we investigated the role of meniscus shape, controlled by the gap distance between coating head and substrate, as well as by the coating velocity, on the morphology formation of zone-cast TIPS-pentacene. Three morphological subregimes are found and explained by fluid dynamics in the meniscus: I) stick-slip morphology, II) unidirectionally aligned crystals, III) spherulitic morphology and IV) directional branched structure. Type II morphology provides improved crystallite size, saturation and effective mobilities as well as reduced trap density in the thin films. Numerical simulation of the fluid dynamics provides insights about the concentration and temperature gradients responsible for the morphology transitions. The enhanced concentration gradient and minimum temperature difference in the front meniscus explain the formation of morphology type II and trigger a higher crystal alignment and structure homogeneity. Finally, this work provides fundamental understanding of the role of the meniscus shape on film morphology during zone-casting, which is important for scaling-up any MGC technique for deposition of functional layers for practical applications especially in electronics.

The content of this chapter has been published in Advanced Functional Materials.

Reprinted with permission from (Adv. Func. Mater. 2024, 2314131)

Copyright © 2024, “John Wiley and Sons” publishing group.

References

1. Gu, X., et al., *The meniscus-guided deposition of semiconducting polymers*. Nature Communications, 2018. **9**(1).
2. Chen, M., et al., *Understanding the Meniscus-Guided Coating Parameters in Organic Field-Effect-Transistor Fabrications*. Advanced Functional Materials, 2019. **30**(1).
3. Janneck, R., et al., *Influence of Solute Concentration on Meniscus-Guided Coating of Highly Crystalline Organic Thin Films*. Advanced Materials Interfaces, 2019. **6**(19).
4. Yildiz, O., et al., *Optimized Charge Transport in Molecular Semiconductors by Control of Fluid Dynamics and Crystallization in Meniscus-Guided Coating*. Advanced Functional Materials, 2021.
5. Diao, Y., et al., *Solution coating of large-area organic semiconductor thin films with aligned single-crystalline domains*. Nature Materials, 2013. **12**(7): p. 665-71.
6. Lee, J.C., et al., *Numerical Simulations and In Situ Optical Microscopy Connecting Flow Pattern, Crystallization, and Thin-Film Properties for Organic Transistors with Superior Device-to-Device Uniformity*. Advanced Materials, 2020. **32**(48): p. e2004864.
7. Born, P., et al., *Role of the meniscus shape in large-area convective particle assembly*. Langmuir, 2011. **27**(14): p. 8621-33.
8. Zhang, K., et al., *Key role of the meniscus shape in crystallization of organic semiconductors during meniscus-guided coating*. Materials Horizons, 2020. **7**(6): p. 1631-1640.
9. Le Berre, M., Y. Chen, and D. Baigl, *From convective assembly to landau - Levich deposition of multilayered phospholipid films of controlled thickness*. Langmuir, 2009. **25**(5): p. 2554-2557.
10. Janneck, R., et al., *Predictive Model for the Meniscus-Guided Coating of High-Quality Organic Single-Crystalline Thin Films*. Advanced Materials, 2016. **28**(36): p. 8007-8013.
11. Giri, G., et al., *Tuning charge transport in solution-sheared organic semiconductors using lattice strain*. Nature, 2011. **480**(7378): p. 504-508.
12. Izawa, T., E. Miyazaki, and K. Takimiya, *Molecular Ordering of High-Performance Soluble Molecular Semiconductors and Re-evaluation of Their Field-Effect Transistor Characteristics*. Advanced Materials, 2008. **20**(18): p. 3388-3392.

13. Lee, J.H., et al., *Effect of Crystallization Modes in TIPS-pentacene/Insulating Polymer Blends on the Gas Sensing Properties of Organic Field-Effect Transistors*. Scientific Reports, 2019. **9**(1): p. 21.
14. Kwon, S., et al., *Organic Single-Crystal Semiconductor Films on a Millimeter Domain Scale*. Advanced Materials, 2015. **27**(43): p. 6870-7.
15. Yu, W.Z.a.G., *Clean and Sustainable Society*. Vol. 3. 2017. 1-7.
16. Doumenc, F. and B. Guerrier, *Self-patterning induced by a solutal Marangoni effect in a receding drying meniscus*. Europhysics Letters, 2013. **103**(1).
17. Zhang, K., et al., *Crystallization Control of Organic Semiconductors during Meniscus-Guided Coating by Blending with Polymer Binder*. Advanced Functional Materials, 2018. **28**(50).
18. Janneck, R., et al., *Influence of Solute Concentration on Meniscus-Guided Coating of Highly Crystalline Organic Thin Films*. Advanced Materials Interfaces, 2019. **6**(19): p. 1-11.
19. http://www.ddbst.com/en/EED/PCP/DEN_C159.php, *Density of Tetrahydrofuran*. Dortmund Data Bank.
20. http://www.ddbst.com/en/EED/PCP/VIS_C159.php, *Dynamic Viscosity of Tetrahydrofuran*. Dortmund Data Bank.
21. B. V. Lebedev, I.B.R., V. I. Milov, and V. Y. Lityagov, *Thermodynamic properties of tetrahydrofuran from 8 to 322 K*. The Journal of Chemical Thermodynamics, 1978. **10**(4): p. 321-329
22. Q. F. Lei, R.S.L., D. Y. Ni, and Y. C. Hou, *Thermal Conductivities of some Organic Solvents and their Binary Mixtures*. Journal of Chemical & Engineering Data, 1997. **42**: p. 971-974.
23. http://www.ddbst.com/en/EED/PCP/SFT_C159.php, *Surface Tension of Tetrahydrofuran*. Dortmund Data Bank.
24. I.A., H., *Vapor heat capacities and enthalpies of vaporization of six organic compounds*. Journal of Chemical Thermodynamics, 1981. **13**: p. 405-414.
25. Majer, V.S., V., *Enthalpies of Vaporization of Organic Compounds: A Critical Review and Data Compilation*. Vol. 300. 1985, Blackwell Scientific Publications: Oxford.
26. Zhang, Z., et al., *Marangoni-Effect-Assisted Bar-Coating Method for High-Quality Organic Crystals with Compressive and Tensile Strains*. Advanced Functional Materials, 2017. **27**(37): p. 1-9.

27. Ramanan, C., et al., *Competition between singlet fission and charge separation in solution-processed blend films of 6,13-bis(triisopropylsilylethynyl)pentacene with sterically-encumbered perylene-3,4:9,10-bis(dicarboximide)s*. Journal of American Chemical Society, 2012. **134**(1): p. 386-97.
28. Yuan, Y., et al., *Ultra-high mobility transparent organic thin film transistors grown by an off-centre spin-coating method*. Nature Communications, 2014. **5**: p. 3005.
29. Stock, B.D.C.a.S.R., *Elements of X-ray Diffraction*. 3rd ed. 2001: Prentice-Hall Inc. 96-102.
30. Choi, H.H., et al., *Critical assessment of charge mobility extraction in FETs*. Nature Materials, 2017. **17**(1): p. 2-7.
31. Kalb, W.L. and B. Batlogg, *Calculating the trap density of states in organic field-effect transistors from experiment: A comparison of different methods*. Physical Review B, 2010. **81**(3).

4. Meniscus wettability-guided crystallization of molecular semiconductors

4.1 Introduction

Over three decades, researchers in the field of organic electronics have been striving to create stable, reproducible, and high-performance organic transistors. To date, not only the limitations imposed by the nature of organic semiconductors (OSCs) have been understood but also the chemical design of OSCs.[1-3] Several articles reported mobilities beyond $10 \text{ cm}^2 \text{ V}^{-1} \text{ s}^{-1}$, allowing organic transistors to be a part of matrix displays, logic circuits and sensor arrays.[4] Before being upscaled to industrial production these electronic applications must match a few requirements. Three critical factors are the operational lifetime[5], stability[6], and reproducibility of the transistors[7]. To address the reproducibility and stability issues the device-to-device uniformity, minimized crosstalk between neighboring transistors and a negligible leakage current should be ensured.[8] Inorganic FETs in industrial processes reduce the crosstalk by electrically isolating each transistor or chip in their operational area.[9] This is usually achieved by a photolithography process, which involves exposing semiconductors to strong ultraviolet (UV) light, high temperature annealing and lift-off processes. In contrast, OSCs are too fragile to survive these photolithographic processes. An alternative could be to precisely allocate OSCs directly during deposition on the active channel area of OFETs.[10, 11] To do so, evaporating OSCs through a patterned mask has already been recognized as a fast and easy method.[12] However, patterning OSCs using a solution process technique can be achieved either by using a pre-etched substrate that only allows the solution to contact the target area[13] or by controlling the evaporation of the solvent via hydrophilic / hydrophobic SAMs[14]. The latter was based on mitigating the contact angle of a solution to induce a selective crystallization of the OSC within the OFET channel. This wettability control strategy

has been applied to various solution process techniques such as drop-casting[14], spin-coating[15], inkjet printing[16] and meniscus-guided coating (MGC)[17]. In particular, the wettability control strategy with MGC deposition has previously been studied in terms of area-dependent crystallization, where the crystallite texture was shown to become less oriented upon reducing the width of the pattern from 400 to 100 μm . [18] In chapters 2 and 3, I have discussed in detail the effect of the casting speed, solution concentration and gap distance. [19, 20] I discuss in this chapter the patterning of OSCs on the channel area of OFETs during MGC. Unlike other solution processing techniques, the use of a patterned substrate during MGC modulates the contact angle of the meniscus by spontaneously inducing crystallization on the wettable area and banning the crystallization on the unwettable area. Therefore, achieving an optimal morphology in this case is more complex than simply patterning the OSC. To the best of our knowledge, understanding of the crystallization behavior of molecular semiconductors on a patterned substrate during MGC deposition is still missing. Particularly, the control of mass transport in MGC as shown in chapter 2 and chapter 3 significantly influences the morphology of the thin films. [20] Thus, a dedicated research is needed to understand the relation between the selective crystallization via wettability control and MGC deposition.

In this work, the selective crystallization behavior of TIPS-pentacene is systematically investigated during MGC deposition with respect to different casting speeds and solution concentrations by using a patterned substrate. With increasing casting speed and concentration, four types of distinct morphologies are identified: I) ‘unidirectional bands’, II) a ‘directional branched’, III) spherulite and IV) ‘interrupted unidirectional bands’. The evaluation of TIPS-pentacene patterned morphologies in OFETs showed that type I exhibits the highest saturation mobility. Furthermore, the crosstalk suppression provided by the patterned OSC reduces the leakage current by three orders of magnitude compared to a thin film deposited by the standard MGC deposition.

4.2 Results and Discussion

4.2.1 Patterning strategy

Fabricating locally OSCs as the channel area of OFETs by the MGC method requires multiple steps, which are illustrated in **Figure 4.1**. In the initial step $a \rightarrow b$, a $\text{SiO}_2/\text{Si}^{++}$ substrate was exposed to ultraviolet (UV) light for 3 min then followed by baking of the substrates with HMDS solution for ~1 hour in a vacuum oven. The oven pressure and temperature were set to ~10.0 mbar and 140°C, respectively. The aim of the preliminary UV light exposure is to eliminate the contaminants and enhance the density of hydroxyl groups on the SiO_2 surface. Considering that hydroxyl groups form the chemical bond with HMDS molecules, achieving a surface with a higher and uniformly distributed HMDS density is crucial and depends on the density of surface hydroxyl groups. In the next step $b \rightarrow c$, UV light was exposed to the HMDS modified substrate through a pre-designed mask for ~1 min. The pre-designed mask enables the UV-light to only reach the specific area intended for the OFET construction. This process results in a more wettable surface by removing the HMDS SAMs, creating a bare SiO_2 surface on the target area. As illustrated in the fourth sketch, d , in **Figure 4.1**, a patterned substrate with regions with and without HMDS on SiO_2 is generated. Subsequently, zone-casting of the OSC solution was performed in step e . Lastly, sketch f presents the patterned substrate with the OSC, where the OSCs have crystallized exclusively on the bare SiO_2 regions.

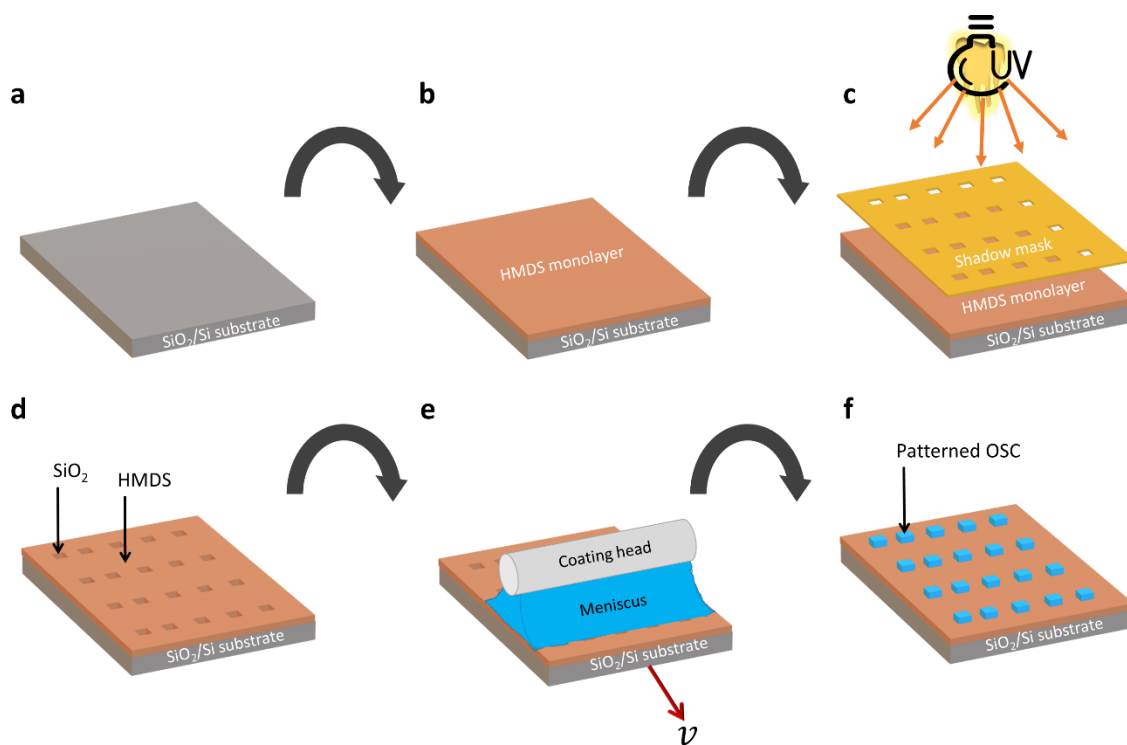


Figure 4.1 Representative sketches of the wettability-guided patterned crystallization steps. The $a \rightarrow b$ indicates that a HMDS SAM is vapor deposited on a SiO_2/Si substrate. Then, $b \rightarrow c$ shows UV-light exposure to the substrate through a shadow mask. As shown in sketch d , the modified substrate consists of SiO_2 and HMDS created as a result of steps a , b and c . From $d \rightarrow e$, MGC coating of the OSC solution on the patterned surface. Lastly, sketch f reveals OSC crystal formation only occurring on the wettable SiO_2 during MGC.

To understand the influence of the HMDS modification of the Si / SiO_2 surface on wettability, illustrated in the sketch of **Figure 4.2a**, contact angle goniometer measurements were performed. Upon dropping $\sim 5.0 \mu\text{l}$ distilled water on the HMDS and SiO_2 surface, a 56.3° contact angle for SiO_2 (**Figure 4.2b**) and 89° for HMDS (**Figure 4.2c**) were determined, respectively. The comparison between the HMDS and SiO_2 surface reveals that the HMDS SAM significantly modifies the surface and makes it hydrophobic (unwettable) while SiO_2 remains hydrophilic (wetable). **Figure 4.2d** exhibits a top view of the zone-cast transistor

substrate where the OSC solution preferentially attaches on the bare SiO₂ due to its wettability. When the substrate-liquid contact angle is higher, as in the case of the HMDS / OSC solution, the solvent evaporation becomes slower. Particularly, in MGC methods where the substrate moves with a constant speed, it is likely not possible that crystallization would start on a hydrophobic surface (HMDS in our case) due to the very low evaporation speed of the solvent. **Figures 4.2e** and **4.2f** present the real-time recorded zone-casting and a POM image of the thin film, in which the crystallization of TIPS-pentacene only takes place on the bare SiO₂ area.

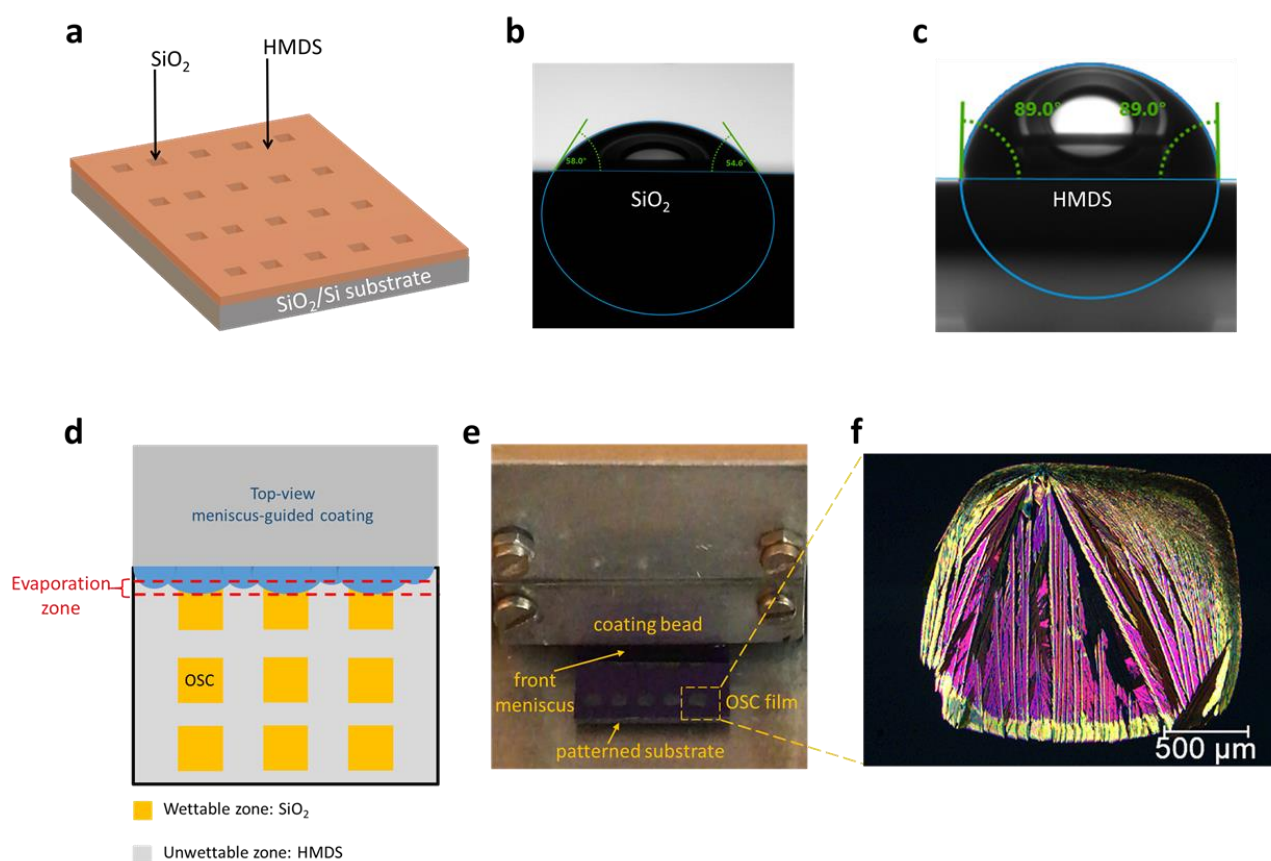


Figure 4.2 The patterned substrate is shown in (a). The corresponding water contact angle with SiO₂ (b) and HMDS (c) are 56° and 89°. d) A sketch of top-view MGC reveals that the contact angle of the OSC solution is spread over the wettable SiO₂ and is bead-shaped on the

unwetttable HMDS. e) Real time image of zone casting TIPS-pentacene. f) POM image of TIPS-pentacene deposited at a speed of 0.1 mm s^{-1} with a concentration of 1 mg ml^{-1} .

4.2.2 Morphology mapping

To understand the selective crystallization of TIPS-pentacene during MGC, I varied two main parameters of MGC that are the casting speed and the solution concentration. While the substrate and solution temperature were set to 45°C , the deposition was performed using the zone-casting setup. The OSC solution was prepared by dissolving TIPS-pentacene in THF with variable concentrations. The dry solid film morphologies are shown in **Figure 4.3** corresponding to the following casting speeds and concentrations: 0.1 mm s^{-1} , 0.2 mm s^{-1} , 0.4 mm s^{-1} and 0.6 mm s^{-1} ; and 1.0 mg ml^{-1} , 1.5 mg ml^{-1} , 2.0 mg ml^{-1} , 3.0 mg ml^{-1} and 8.0 mg ml^{-1} . As discussed in **Figures 4.1** and **4.2**, TIPS-pentacene during MGC formed a solid film only inside the SiO_2 region, but a few cases exhibited an extend beyond this specific region.

Varying the casting speed and concentration results in four different morphologies: I) ‘unidirectional bands’, II) a ‘directional branched’, III) spherulite and IV) ‘interrupted unidirectional bands’. Type I, II, and IV allow controlling the growth direction of crystals regarding casting direction. Among them, type I is observed at 0.1 mm s^{-1} and 0.2 mm s^{-1} for concentrations in the range $1.0 \text{ mg ml}^{-1} < c_0 < 3.0 \text{ mg ml}^{-1}$. During MGC of the type I morphology, no solvent evaporation takes place until the meniscus contacts the SiO_2 region where an immediate crystallization starts. Specifically, these crystallization initiation points are clearly visible for the type I shown by POM images in **Figure 4.2** (start of the crystallization in the casting direction). However, the growth direction of the crystals from these starting points and onwards exhibit misalignment with respect to the casting direction. The reason for such crystal misalignment could be attributed to insufficient mass transport. Firstly, more mass

transport is required at low casting speed because of the higher film thickness. Secondly, the solvent does not have enough time to switch the angle and starts evaporating. Therefore, the start of crystallization with respect to the casting direction only exhibits a few nucleation starting points where later more nucleation centers (higher number of unidirectional crystals) are formed. As an example of the cause of the crystal alignment problem, a previous study showed that insufficient mass transport leads to a time-lag in the continuity of crystallization, resulting in crystal misalignment.[21]

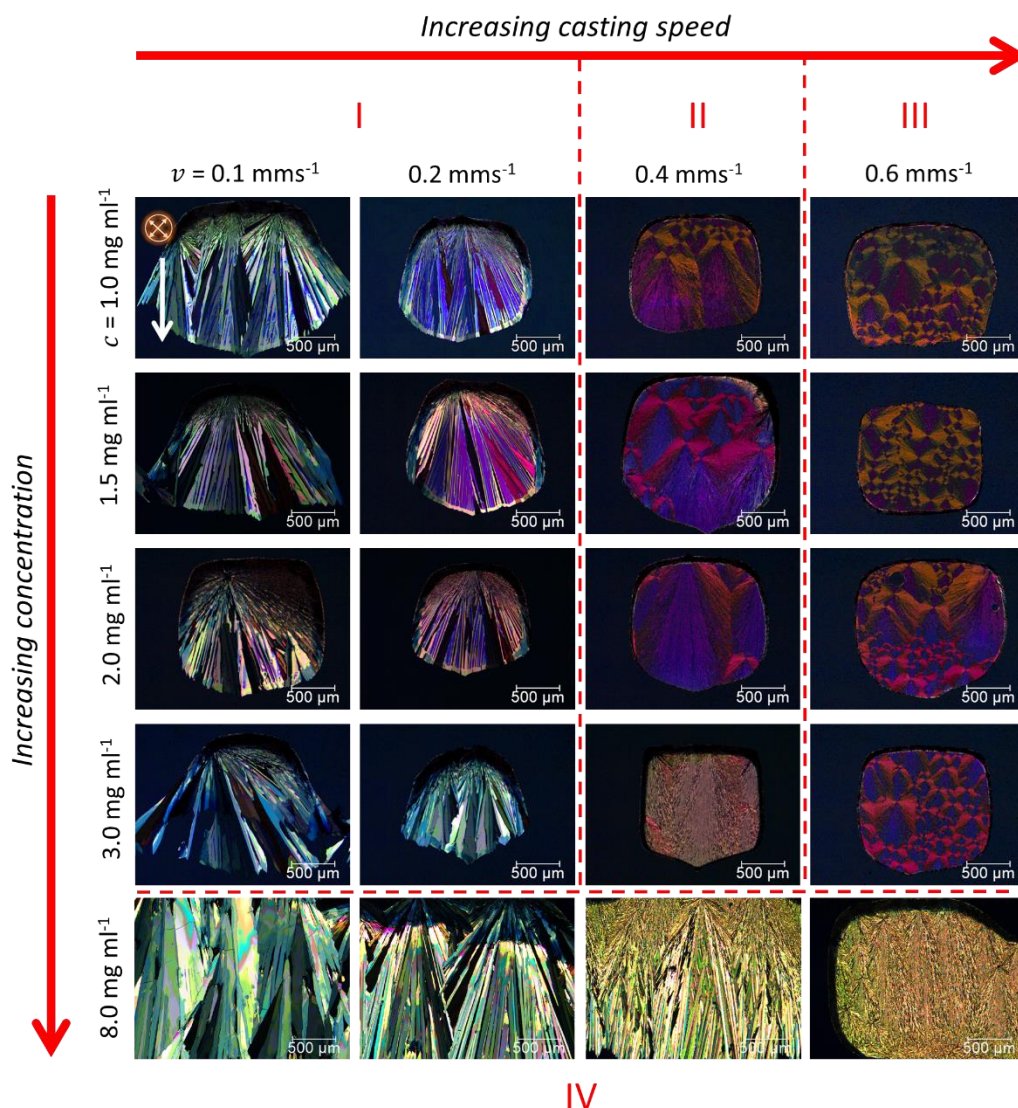


Figure 4.3 Morphology of zone-cast TIPS-pentacene as a function of casting speed and concentration. In the first image, the white and crossed arrows indicate the coating direction and the position of polarizers. The red-dashed lines split four types of morphologies regarding the casting speed and concentration.

Upon increasing the speed to 0.4 mm s^{-1} , the type II morphology appears, i.e. ‘directional branched’. A greater number of unidirectional crystals are formed due to the increase in the concentration gradient next to the contact line. Similarly, the effect of casting

speed in the evaporation regime has been discussed in chapter 2.[20] The 2D-simulation in the coating bead showed that the higher concentration gradient is found when the speed is increased, giving a higher density of nucleation centers (details in chapter 2, section 2.2.2).[20]

The type III morphology emerges at 0.6 mm s^{-1} , where a spherulite structure is observed. This morphology indicates that the casting direction does not have an influence on the crystal growth direction, which is the case when the speed is in the transition regime between the evaporation and Landau-Levich regimes[22]. Previously, zone-cast TIPS-pentacene at a speed in the transition regime showed spherulitic morphology as discussed in chapter 3 and section 3.2.1.[19] Furthermore, the type IV morphology, namely ‘interrupted unidirectional bands’, appears at a concentration of 8 mg ml^{-1} in the speed range $0.1 \text{ mm s}^{-1} < v < 0.6 \text{ mm s}^{-1}$. The latter exhibits a film formation extending beyond the region of SiO_2 . This observation identifies that the nucleation barrier can be exceeded even on the unwettable region with a high solute concentration. The contact angle of the meniscus does not play a significant role in patterning the OSC at high concentration.

4.2.3 OFETs

To evaluate the electrical performance of different TIPS-pentacene morphologies, a TG / BG OFET configuration was used. A 50.0 nm thick Au was deposited on the top of the OSC as the source and drain electrodes. The transfer curves are presented in **Figure 4.4a** for 0.1 mm s^{-1} and 0.2 mm s^{-1} (type I), 0.4 mm s^{-1} (type II) and 0.6 mm s^{-1} (type III) with a concentration of 1.0 mg ml^{-1} . The switch-on voltage for all cases is nearly 0 V as found from $I_{ds}^{1/2}$ vs V_g in **Figure 4.4a**. The corresponding saturation mobility μ_{sat} of the transfer curves are presented in **Figure 4.4b**. Accordingly, the average μ_{sat} was the highest for the type I morphology with a value of $0.14 \text{ cm}^2 \text{ V}^{-1} \text{ s}^{-1}$ (0.1 mm s^{-1}), then followed by the thin film deposited at 0.2 mm s^{-1} that obtained

a value of $0.10 \text{ cm}^2 \text{ V}^{-1} \text{ s}^{-1}$. The standard deviation for the thin film at 0.1 mm s^{-1} is slightly higher due to the misaligned crystals. Furthermore, both the type II and III morphologies obtained an average μ_{sat} of nearly $\sim 0.05 \text{ cm}^2 \text{ V}^{-1} \text{ s}^{-1}$. The values of μ_{sat} in **Figure 4.4b** are relatively moderate compared to the study reported in chapter 3 based on zone-cast TIPS-pentacene[19], because the OFET channel's distance to the first place where the crystallization starts is very short. Therefore, there is not enough time for a better crystal alignment with respect to the casting direction. Although outside the scope of this study, further study is required to understand the ideal time and distance for optimal crystal alignment during MGC. In addition, the threshold voltage V_{th} and the I_{on}/I_{off} ratio, extracted from the transfer curves in **Figure 4.4a** are shown in **Figure 4.4c**. The average V_{th} is between -3.0 V and -6.0 V , with the lowest average $V_{th} = -3.0 \text{ V}$ found for the speed 0.1 mm s^{-1} . The average I_{on}/I_{off} ratio for all morphology types is in the range of 10^4 , with the highest being $\sim 4 \times 10^4$ for type I.

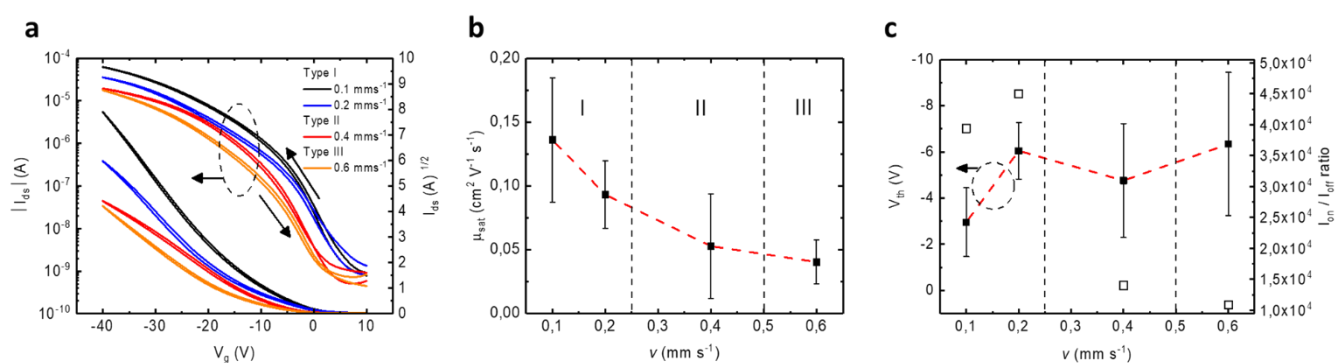


Figure 4.4 a) Transfer curves of TIPS-pentacene films deposited at the speeds: 0.1 mm s^{-1} and 0.2 mm s^{-1} (type I), 0.4 mm s^{-1} (type II) and 0.6 mm s^{-1} (type III) and the concentration of 1.0 mg ml^{-1} . All the measurements were done for a constant $V_{ds} = -40.0 \text{ V}$. The saturation mobility μ_{sat} (b), the average threshold voltage V_{th} and I_{on}/I_{off} ratio (c) were shown as a function of the speed. The red-dashed lines in (b) and (c) are for eye-guide.

To further investigate the effect of the patterned OSCs in the channel area of the OFET, we performed zone-casting deposition of TIPS-pentacene on a bare SiO₂ surface only, where the OSC completely covered the surface. The deposition parameters were chosen from the type I morphology (**Figure 4.3**), using a casting speed of 0.1 mm s⁻¹ and a concentration of 1.0 mg ml⁻¹. I refer to this wafer as ‘non-isolated’, and the one fabricated on the patterned substrate as ‘patterned’. A third case, where the surrounding OSCs of the OFET channel of a ‘non-isolated’ wafer is removed by a hand-held toothpick, is called ‘isolated’. The sketch of these three wafers is shown in **Figure 4.5a**, where the green color refers to TIPS-pentacene and the gray color to the SiO₂. The comparison between the ‘patterned’ and ‘non-isolated’ cases is shown in **Figure 4.5**, where the transfer curve of I_{ds} and $I_{ds}^{1/2}$ with respect to the V_g sweep is shown in **Figure 4.5b** and also I_{ds} and I_{gs} with respect to the V_g sweep is shown in **Figure 4.5c**. Both cases obtained a similar highest I_{ds} of 8×10^{-5} A shown in **Figure 4.5b**. The gate leakage I_{gs} between the ‘patterned’ and the ‘non-isolated’ case indicates a three orders of magnitude difference in which the ‘patterned’ case shows $\sim 10^{-10}$ A whereas the ‘non-isolated’ transistor exhibits $\sim 1.4 \times 10^{-7}$ A at $V_{ds} = 40.0$ V. Considering 20 OFETs in one wafer expanding on an area of 15 mm \times 20 mm, the crosstalk between the neighboring devices for the ‘non-isolated’ wafer leads to a higher leakage current from the source to the gate electrode. The patterning strategy reduces the crosstalk and the leakage current by up to three orders of magnitude as an outcome of the latter comparison. As a further check on this claim, we compared the same OFET while it was measured as ‘non-isolated’, which was later measured again as ‘isolated’ after the removal of surrounding OSC around the OFET channel. The relative comparison shown in **Figure 4.5d** and **4.5e** confirms the claim from the previous comparison in **Figure 4.5c**, the leakage current I_{gs} shown in **Figure 4.5e** also reduces three orders of magnitude from $\sim 2.0 \times 10^{-7}$ A to $\sim 10^{-10}$ A

for the same device upon removing the surrounding OSC around the OFET channel. The impact of such reduced I_{gs} is slightly visible in **Figure 4.5d** on switch-on I_{ds} . At $V_g = 5.0$ V, the ‘non-isolated’ OFET in the forward sweep exhibits an off-current value of 1.2×10^{-9} A and the ‘isolated’ OFET showing a value of 8.4×10^{-10} A.

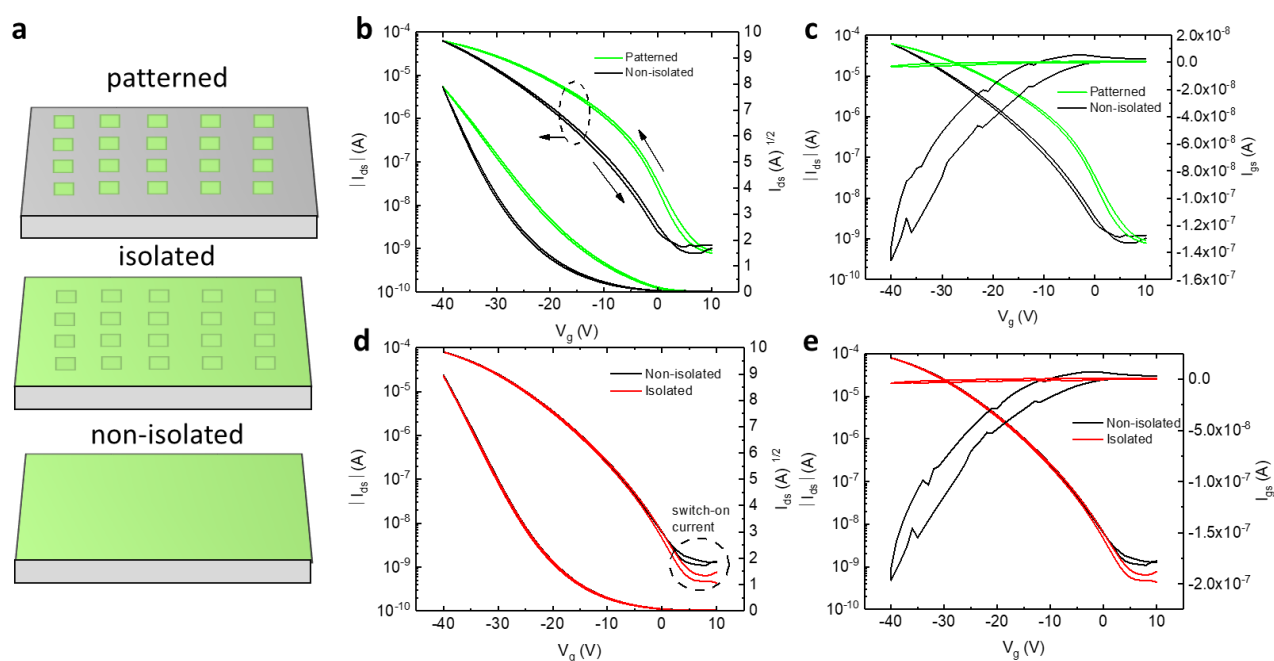


Figure 4.5 Patterned, isolated and non – isolated TIPS – pentacene films are shown in (a). The patterned film is deposited using MWGC method. The non – isolated film is deposited by MGC on bare SiO_2 . Lastly, the isolation film is achieved by manually removing the OSC around the OFET channel with the help of a wood stick. (b, c) Comparison of transfer characteristics between patterned and non – isolated film and (d, e) between isolated and non – isolated film. (b, d) displays I_{ds} and $I_{ds}^{1/2}$ as a function of V_g and (c, e) displays I_{ds} and I_{gs} as a function of V_g .

The difference in I_{ds} could be attributed to the drain leakage in the off-state of the OFET when a ‘non-isolated’ device is present, leading to crosstalk with the neighbor devices.

Although the values are very small, the electrostatic interaction between the source and the drain electrodes of the operating device and the electrodes of the neighboring devices via OSC is likely to increase the gate leakage I_{ds} and the drain leakage I_{ds} in the off-state.

As a result, the patterning strategy using MGC reduces crosstalk, where its effect was demonstrated in terms of reduced gate leakage and drain leakage based on a single OFET analysis.

4.3 Conclusion

In conclusion, zone-cast TIPS-pentacene on a patterned surface with a strategy based on wettability control revealed four distinguished morphologies for the variation of concentration and casting speed: I) ‘unidirectional bands’, II) a ‘directional branched’, III) spherulite and IV) ‘interrupted unidirectional bands’. The type I among those exhibited the best and best reproducible charge transport behavior in OFETs. Furthermore, multiple comparisons to understand the benefit of OSC patterning have shown that gate leakage and drain leakage currents can be reduced by disrupting the crosstalk between the neighbor devices. Finally, the findings in the study can be potentially used for upscaling MGC and integrated circuits applications.

References

1. Sirringhaus, H., *25th anniversary article: Organic field-effect transistors: The path beyond amorphous silicon*. *Advanced Materials*, 2014. **26**(9): p. 1319-1335.
2. Bronstein, H., et al., *The role of chemical design in the performance of organic semiconductors*. *Nature Reviews Chemistry*, 2020.
3. Facchetti, A., *Semiconductors for organic transistors*. *Materials Today*, 2007. **10**(3): p. 28-37.
4. Liu, K., et al., *Advances in flexible organic field-effect transistors and their applications for flexible electronics*. *npj Flexible Electronics*, 2022. **6**(1).
5. Chen, X., et al., *Balancing the film strain of organic semiconductors for ultrastable organic transistors with a five-year lifetime*. *Nature Communications*, 2022. **13**(1): p. 1480.
6. Park, S., et al., *Recent Advances in the Bias Stress Stability of Organic Transistors*. *Advanced Functional Materials*, 2019. **30**(20).
7. Kumagai, S., et al., *Scalable Fabrication of Organic Single-Crystalline Wafers for Reproducible TFT Arrays*. *Scientific Reports*, 2019. **9**(1): p. 15897.
8. Zhao, X., et al., *Organic Semiconductor Single Crystal Arrays: Preparation and Applications*. *Advanced Science*, 2023. **10**(15): p. e2300483.
9. Rifhan Amira Mohd Razif, S.M.M.M., Azri Husni Hasani and Zuhanis Mansor, *Mitigation techniques for crosstalk in ICs*. *The Electronic Packaging Interconnect Technology Symposium 2019*, 2019. **701**.
10. Zhang, X., et al., *Alignment and Patterning of Ordered Small-Molecule Organic Semiconductor Micro-/Nanocrystals for Device Applications*. *Advanced Materials*, 2016. **28**(13): p. 2475-503.
11. Zhang, X., et al., *Precise Patterning of Organic Semiconductor Crystals for Integrated Device Applications*. *Small*, 2019. **15**(27): p. e1900332.
12. Klauk, H., et al., *Ultralow-power organic complementary circuits*. *Nature*, 2007. **445**(7129): p. 745-8.
13. Cavallini, M., et al., *Ambipolar multi-stripe organic field-effect transistors*. *Advanced Materials*, 2011. **23**(43): p. 5091-7.
14. Minari, T., et al., *Controlled self-assembly of organic semiconductors for solution-based fabrication of organic field-effect transistors*. *Advanced Materials*, 2012. **24**(2): p. 299-306.

15. Li, Y., et al., *Large plate-like organic crystals from direct spin-coating for solution-processed field-effect transistor arrays with high uniformity*. *Organic Electronics*, 2012. **13**(2): p. 264-272.
16. Kim, Y.H., et al., *Controlled deposition of a high-performance small-molecule organic single-crystal transistor array by direct ink-jet printing*. *Advanced Materials*, 2012. **24**(4): p. 497-502.
17. Deng, W., et al., *Channel-restricted meniscus self-assembly for uniformly aligned growth of single-crystal arrays of organic semiconductors*. *Materials Today*, 2019. **24**: p. 17-25.
18. Giri, G., E. Miller, and Z. Bao, *Selective solution shearing deposition of high performance TIPS-pentacene polymorphs through chemical patterning*. *Journal of Materials Research*, 2014. **29**(22): p. 2615-2624.
19. Yildiz, O., et al., *Role of Meniscus Shape on Crystallization of Molecular Semiconductors and Fluid Dynamics During Meniscus-Guided Coating*. *Advanced Functional Materials*, 2024.
20. Yildiz, O., et al., *Optimized Charge Transport in Molecular Semiconductors by Control of Fluid Dynamics and Crystallization in Meniscus-Guided Coating*. *Advanced Functional Materials*, 2021. **32**(2).
21. Lee, J.C., et al., *Numerical Simulations and In Situ Optical Microscopy Connecting Flow Pattern, Crystallization, and Thin-Film Properties for Organic Transistors with Superior Device-to-Device Uniformity*. *Advanced Materials*, 2020. **32**(48): p. e2004864.
22. Damien Baigl, Y.C., etc., *From Convective Assembly to Landau-Levich Deposition of Multilayered Phospholipid Films of Controlled Thickness*. *Langmuir*, 2008.

Chapter 5 Conclusions

In this thesis, control of the crystallization behavior of OSCs has been studied by MGC deposition. Several significant points were understood and described, which were missing in the literature.

In chapter 2, an optimal processing window in terms of casting speed and concentration were defined for zone-cast C8-BTBT and the numerical simulations of coating bead and crystallization explained the morphological transitions of OSC. The concentration does not change the morphology but shifts the transition speed between morphologies. A narrow window in the evaporation regime provides the most efficient charge transport that enables an advanced OFET performance. Moreover, the transitions between morphologies were highly impacted by the concentration gradient next to the contact line. The concentration gradient was found to be rising with increasing the casting speed by the numerical simulation in the coating bead and leading to higher density of nucleation sites.

In chapter 3, the role of meniscus shape during MGC was studied. An ideal coating height (gap distance) during MGC was not defined before for the low-weight molecular semiconductors. The investigation showed that the thin films deposited at low gap distance (zone-cast TIPS-pentacene at $d < 0.25$ mm) improves the meniscus stability by reducing the thermal Marangoni effect. However, a thin film deposited at a high gap distance ($d > 0.25$ mm) exhibited periodic ridges formed perpendicular to the casting direction. The numerical simulation in the coating bead explained the temperature distribution at the front meniscus interface highly dependent on the meniscus shape (gap distance). The difference in the temperature distribution at the front meniscus increases with increasing the gap distance that results in stronger thermal Marangoni flow. Therefore, the inhomogeneous periodic ridges in the thin films deposited at high gap distance originate from the hydrodynamic instability caused by strong Marangoni flow.

In chapter 4, precise allocation of OSCs during MGC was succeeded by controlling the wettability of substrates via SAM modification. The morphology mapping of zone-cast TIPS-pentacene based on patterned substrates showed that a high concentration leads to crystallization beyond the intended hydrophilic area. The advantage of patterning OSCs on the active channel of OFETs was demonstrated by reducing the leakage current by three orders of magnitude. This was achieved by eliminating the crosstalk between the neighboring devices.

In conclusion, the optimization of MGC parameters and their coupling has been investigated and understood, which will be helpful for the future implementation of solution processing in OFET fabrication. The insights gained from these studies have the potential to drive the upscaling of MGC techniques, playing a vital role in understanding the crystallization behavior of OSCs

Chapter 6 Experimental appendix

Electrical parameter evaluation of OFETs

Threshold voltage

Threshold voltage is found from $I_{ds}^{1/2}$ - V_g relation. The linear slope for mobility estimation intercepts with x -plane when $I_{ds}^{1/2} = 0$, this intercept point in V_g is the threshold voltage. When sweeping V_g reaches threshold voltage V_{th} , the first time a conduction channel is provided between the source and the drain at V_{th} . [1]

Subthreshold swing

Subthreshold swing, SS , is another important parameter showing how fast I_{ds} increases one-order of magnitude in respect to applied V_g in the subthreshold region. It can be calculated using eqn. below. [2]

$$SS = \frac{dV_g}{d \log I_{ds}}$$

Switch on voltage

The switch-on voltage refers to the required bias voltage to establish a conduction channel between the source and the drain. The switch-on voltage is the intercept point of x -plane with the subthreshold linear fit. If an Ohmic contact is formed at the electrode / OSC interface, a linear $I_{ds}^{1/2}$ - V_g curve should give a value of switch on voltage that is equal to V_{th} .

Switch on / off ratio

The switch on / off ratio is found by dividing the I_{ds} value at the point the transistor is turned-on and by the point the transistor is turned-off.[3]

Materials and substrate preparation

Highly doped silicon substrates with a 300 nm thick SiO₂ layer were cleaned in an ultrasonic bath by using acetone, hexane, toluene, and isopropyl alcohol. After exposure to oxygen plasma for 10 min, the surface was treated with trichloro(phenethyl)silane (PETS) in a vacuum oven heated at 140 °C and vacuumed to 10 mbar for 3 h. All solvents, C8-BTBT, TIPS-pentacene and PETS were purchased from Sigma-Aldrich and used as received.

Zone-casting

Zone-casting was performed in a specially designed setup. The solution and the substrate were heated at 45 °C. The substrate speed was controlled in the range from 40 μm s⁻¹ to 5000 μm s⁻¹.

Morphological and structural characterization

Film thickness measurements were done by a KLA Tencor Profilometer. Optical Microscopy Images were obtained by a Leica Light Microscope in reflected light. AFM studies were done using Park System NX-20 in tapping mode. Grazing incidence wide-angle X-ray

scattering (GIWAXS) measurements were performed at the Dortmund Electron Accelerator (DELTA) Synchrotron Facility (Dortmund, Germany), beamline BL09. The photon energy was set to 10 keV ($\lambda = 1.24 \text{ \AA}$). The sample chamber was vacuumed to $\sim 1 \text{ m bar}$ during the measurement. The incident angle (α_i) of the X-ray beam was adjusted individually for each sample in the range of 0.08° - 0.12° . The scattered intensity was recorded by a 2D image plate (MAR345, marXperts GmbH, Norderstedt, Germany). The exposure time was 180 s. The q -range ($q = 4 \times \pi \times \sin\theta \times \lambda^{-1}$) was calibrated using silver behenate standart. The data was processed and analyzed using Datasqueeze (University of Pennsylvania, Philadelphia, PA, USA) and OriginPro (OriginLab Corporation, Northampton, MA, USA).

Transistor fabrication and characterization

Chapter 2

BG / TC device configuration was used for the OFETs. C8-BTBT was dissolved in THF with the concentration of 1 mg ml^{-1} . After zone-casting the active layer, 10 nm thick MoO_3 was thermally evaporated on the top of the film through a shadow mask with the evaporation rate of 0.2 \AA s^{-1} followed by 50 nm thick Ag deposited at the evaporation rate of 1 \AA s^{-1} . The channel length of the electrode geometry was ranging from 30 to 80 μm , and the width of the electrodes was 1000 μm . Afterwards, the devices were annealed at $60 \text{ }^\circ\text{C}$ for 12 h in a N_2 -filled glove box. Electrical characterizations were done using Keithley 4200-SCS in a N_2 -filled glove box. Field-effect mobilities were calculated in the saturation regime using conventional transconductance analysis given by $\mu_{sat} = (2L/W)(1/C_i)(\partial\sqrt{I_D}/\partial V_g)^2$. Measurements were done for V_g sweeping from 10 to -40 V at a constant $V_{ds} = -40 \text{ V}$.

Chapters 3 and 4

BG / TC device configuration was used for OFETs. TIPS-pentacene was dissolved in THF at a concentration of 1 mg ml⁻¹. After the zone-casting of the active layer, a 50 nm thick Au layer was deposited at an evaporation rate of 1 Å s⁻¹.

References

1. Horowitz, G., et al., *The Concept of “Threshold Voltage” in Organic Field-Effect Transistors*. *Advanced Materials*, 1998. **10**(12): p. 923-927.
2. Kalb, W.L. and B. Batlogg, *Calculating the trap density of states in organic field-effect transistors from experiment: A comparison of different methods*. *Physical Review B*, 2010. **81**(3).
3. Katsouras, I., et al., *Controlling the on/off current ratio of ferroelectric field-effect transistors*. *Sci Rep*, 2015. **5**: p. 12094.

Acknowledgement

I would like to thank my parents, Songul and Kazim, for their eternal support and efforts in my education, career and life. I would also like to thank my elder sister and brother, Nadiye and Ozkan, for always keeping an eye on me. I would especially like to thank my wife Derya, who has been the greatest support during my Ph.D. studies.

Furthermore, I have had the chance to work with the great scientists and talents, so I would like to acknowledge them. Firstly, I would like to thank my bachelor thesis supervisor Prof. Saziye Ugur, who tragically passed away at an early age in 2020. She introduced the polymer / nanotube blends to me, and we published my first experimental results in a book chapter, which was also my first publication. Secondly, I would like to thank my master thesis supervisors, Dr. Marta Mas Torrent and Dr. Raphael Pfattner, who introduced bar-assisted meniscus shearing to me and organic FETs and assisted completing my master thesis at Autonomous University of Barcelona. Subsequently, I continued working on the same topic with Dr. Tomasz Marszalek as a part of this Ph.D. thesis. I would especially like to thank Dr. Marszalek for accepting me to this position and for all the fruitful discussions we had during my Ph.D. Thirdly, I would like to thank Prof. Wojciech Pisula, Dr. Jasper Michels and our director Prof. Paul Blom for all the meetings and discussions during my time at MPI-P. For the 2D-simulations of meniscus, I would like to acknowledge and thank Dr. Zuyuan Wang. Finally, I am aware that this list could go on for several pages, but in short, I would like to thank all my fellow group members, group leaders and the technical support of MPI-P family.

Lastly, I would like to acknowledge my company, United Monolithic Semiconductors GmbH, where I continue to work on the development of gallium nitride based high electron mobility transistors. I would like to thank Dr. Jan Grünenputt, Dr. Hermann Stieglauer, Dr.

Hervé Blanck and Dr. Daniel Sommer for their support and understanding throughout my Ph.D. process.

List of publications

- 1) H. Fan, H. Yang, Y. Wu, **O. Yildiz**, X. Zhu, T. Marszalek, P. W. M. Blom, C. Cui, Y. Li, Anthracene-Assisted Morphology Optimization in Photoactive Layer for High-Efficiency Polymer Solar Cells. *Adv. Funct. Mater.* 2021, 31, 2103944. <https://doi.org/10.1002/adfm.202103944>
- 2) **O. Yildiz**, Z. Wang, M. Borkowski, G. Fytas, P. W. M. Blom, J. J. Michels, W. Pisula, T. Marszalek, Optimized Charge Transport in Molecular Semiconductors by Control of Fluid Dynamics and Crystallization in Meniscus-Guided Coating. *Adv. Funct. Mater.* 2022, 32, 2107976. <https://doi.org/10.1002/adfm.202107976>
- 3) S. Wang, S. Frisch, H. Zhang, **O. Yildiz**, M. Mandal, N. Ugur, B. Jeong, C. Ramanan, D. Andrienko, H. I. Wang et al: Grain engineering for improved charge carrier transport in two-dimensional lead-free perovskite field-effect transistors. *Materials Horizons* 10 (9), pp. 2633 - 2643 (2022). <https://doi.org/10.1039/D2MH00632D>
- 4) E. del Pino Rosendo, **O. Yildiz**, W. Pisula, T. Marszalek, P. W. M. Blom and C. Ramanan, *Phys. Chem. Chem. Phys.*, 2023, **25**, 6847 <https://doi.org/10.1039/D2CP05240G>
- 5) S. Wang, K. Bidinakis, C. Haese, F. H. Hasenburger, **O. Yildiz**, Z. Ling, S. Frisch, M. Kivala, R. Graf, P. W. M. Blom, S. A. L. Weber, W. Pisula, T. Marszalek, Modification of Two-Dimensional Tin-Based Perovskites by Pentanoic Acid for Improved Performance of Field-Effect Transistors. *Small* 2023, 19, 2207426. <https://doi.org/10.1002/sml.202207426>
- 6) **O. Yildiz**, Z. Wang, M. Brzezinski, S. Wang, Z. Li, J. J. Michels, P. W. M. Blom, W. Pisula, T. Marszalek, Role of Meniscus Shape on Crystallization of Molecular Semiconductors and Fluid Dynamics During Meniscus-Guided Coating. *Adv. Funct. Mater.* 2024, 2314131. <https://doi.org/10.1002/adfm.202314131>

Curriculum vitae

Okan Yildiz

Contact details

Email: yildizokann@gmail.com

yildizo@mpip-mainz.mpg.de

Linkedin: <https://www.linkedin.com/in/yildizok/>



Experiences



Development Engineer - United Monolithic Semiconductors GmbH, Ulm /Germany

March 2023 - present

- Technology development of RF-MMIC devices based on GaN HEMT, which are used in the field of defence & space, telecommunications, automotive radar and industrial sensors
- Module development, technology qualification, electrical tests of GaN HEMT
- Physical analysis on the failure mechanism of semiconductor devices
- Lifetime test analysis in terms of humidity, temperature, mechanical & electrical stress



Research Assistant, Ph.D. - Max Planck Institute for Polymer Research, Mainz / Germany

October 2018 - June 2022

- Design, development and implementation of organic field-effect transistors based on small molecule and polymer semiconductors
- Optimizing electrical behavior of semiconductor films by control of morphology and molecular packing order
- Solid film characterization by microscopy, spectroscopy and x-ray techniques
- Fabrication of electrodes, insulators and organic semiconductors using PVD, spin-coating and MGC techniques



Master Thesis Research Project - Materials Science Institute of Barcelona, Barcelona / Spain

January 2018 - July 2018

- Improving device stability and performance of OFETs
- Controlling morphology of semiconductor / polymer blends by bar-assisted meniscus shearing



Laboratory Assistant - Istanbul Technical University, Istanbul / Turkey

January 2016 - January 2017

- Investigation of conductivity network depending on multi-walled carbon nanotubes (MWCNT) content in polystyrene latex (PS)
- UV-light spectroscopy and conductivity measurements of PS / MWCNT thin films

Education

- **Ph.D. in Physics**
Johannes Gutenberg University, Mainz / Germany
July 2019 - present
- **Master's Degree in Advanced Nanoscience and Nanotechnology**
Autonomous University of Barcelona, Barcelona / Spain
September 2017 - July 2018
- **Bachelor's Degree in Physics Engineering**
Istanbul Technical University, Istanbul / Turkey
January 2012 - January 2017